UNIVERSITÀ
DEGLI STUDI
FIRENZE

DOTTORATO DI RICERCA IN
International Doctorate in Atomic and Molecular Photonics

CICLO *XXXI*

COORDINATORE Prof. Cataliotti Francesco Saverio

The dynamics of melting and crystallization of ices by pump-probe experiments based on ultrafast T-Jump

Settore Scientifico Disciplinare CHIM/02

Dottorando
Dott. *Falsini Naomi*
Naomi Falsini

Tutore
Prof. *Bini Roberto*

Coordinatore
Prof. *Cataliotti Francesco Saverio*

Anni 2015/2018

Abstract

The melting mechanisms on a sub-microscopic scale have been addressed by many experimental and theoretical works covering a sub-nanosecond time window. On the other hand, macroscopic observations of phase transitions, such as the freezing process, take place in a millisecond time window, limited in time by thermal exchange with the environment. The access to the intermediate time interval is difficult to realize both through experimental and theoretical techniques, and it is still completely unexplored. The coverage of this gap is the purpose of this study.

In this thesis the characterization of the melting and crystallization dynamics of water ices (ice I_h and VI) and water-based crystalline structures, such as clathrate hydrates of methane and argon, is reported. The melting dynamics of pure water ices I_h and VI have been experimentally investigated within the entire mesoscopic regime from the first nanoseconds after the melting onset to the complete recrystallization of the sample, by combining the Thermal Jump (T-Jump) technique and the time-resolved Mie scattering spectroscopy. The experiment exploits a pump-probe technique realized by combining the T-Jump source (pump), responsible for the increase of the sample temperature and thus the melting, and a continuous-wave laser used as probe. The crystal sample, kept at static temperature and pressure conditions, is homogeneously and instantaneously heated by an energetic picosecond infrared pulse resonant with a vibrational combination band of water (T-Jump). By monitoring the scattering at the melt-ice interfaces inside the ice sample, the dimensional evolution of the molten domains created by the IR pulse in the crystal lattice has been followed. The experiment gives an unexpected result, revealing a bulk melting of the sample which is not instantaneous (up to the microseconds time scale), characterized by a regime of molten domains dimensions ranging from tens of nanometers up to around 1.5 microns.

In order to proceed in the dynamics investigation of water-based crystalline structures, such as clathrate hydrates which have more complex structures than pure water, an homogeneous initial sample is a fundamental requirement to investigate their melting dynamics. The development of a synthesis technique for hydrates and a loading procedure in the diamond or sapphire anvil cell has been thus necessary. A working procedure to synthesize clathrate hydrates in a high-pressure apparatus, especially designed for this purpose, has been developed. The characterization by FTIR and Raman spectroscopy of melting and recrystallization

of these clathrate hydrates has also been performed in order to investigate the possibility of studying the dynamics of these phase transitions with pump and probe techniques.

In order to access the first nanosecond after the pump pulse, the T-Jump technique has been coupled to the transient infrared (TRIR) absorption spectroscopy to monitor the ice (and potentially clathrate) destruction and formation in time with the necessary time resolution by probing the combination band of water related to bending and libration modes. This experiment allows to access the investigation of melting dynamics from 100 ps after the pump pulse, thus filling the gap with the experiment based on the Mie scattering technique. The melted sample portion as a function of time has been directly quantified, revealing the maximum fraction of the probed ice volume that can be melted: it is about 33%, and is reached in $\sim$ 3 ns. The TRIR experiment, together with the previous method based on Mie scattering, allows to follow the melting dynamics from 100 ps after the pump excitation (T-Jump) to tens of milliseconds, allowing to monitor the entire dynamics from the beginning of melting to recrystallization in bulk water samples, and allowing the experimental characterization of the growth process of the nucleated liquid up to the recrystallization at the thermodynamic conditions of melting.

Contents

Introduction

The study at microscopic level of the dynamics of phase transformations is the focus of this thesis work. The knowledge of the dynamics of a phase transition implies the characterization of the mechanisms employed by the system for changing its aggregation geometry and the kinetics of the process. The transition does not take place in the whole system at the same time, it is not an instantaneous process, in fact it is a dynamic phenomenon typical of each substance and of its aggregation state. A still open discussion concerns the microscopic mechanisms responsible for melting and crystallization phenomena and the amount of time required for passing from one phase to another when the thermodynamic parameters of the system are changed.

Our interest is directed to molecular systems whose rearrangement mechanisms and their characteristic time scales are still not well elucidated also for many of the most common phase transitions, such as melting, despite investigations of phase transitions dynamics having been addressed by several theoretical and experimental works. As the state of the art of the experimental characterizations is concerned, observations of phase transitions have been obtained by imaging and photographic techniques with millisecond or longer time resolution, allowing for long time scales investigations in the macroscopic regime [1, 2]. Such observations account for processes occurring at surfaces and limited in time by thermal exchange with the environment, such as the freezing process. On the other hand, investigations on short time scales (sub-nanosecond time window) allow to monitor structural changes on short length scales, for example of few nanometers, allowing for the explanation of the fundamental mechanisms of the transition onset [3–5]. However, the experiments performed so far are unable to unveil the entire system dynamics.

From the theoretical point of view, computational studies, performed through numerical and molecular dynamics calculations, are unable to handle at the same time large sample volumes and large time scales, allowing for an access, with a noteworthy reliability, limited to the firsts moments of the phenomenon. For example, simulations have determined, in systems such as copper or aluminum, the minimum number of atoms/molecules needed to form a critical nucleus for the transition, the solid/melt interfacial energy, and the transient local structures, revealing a possible nucleation mechanism [6, 7].

One of the main issue encountered in tackling the transition dynamics from an experimental point of view concerns the possibility to control the temperature (T) and pressure (P) conditions during the process. Temperature has a fundamental role in inducing a phase change, but temperature variations at atmospheric pressure allow the access only to a restricted number of transformations for a given system. In addition to temperature, pressure is a powerful tool to rule the behavior of molecular systems. In fact, the extraordinary efficiency of pressure in modifying intermolecular interactions permits a considerable tunability of the local and the long-range structure. Therefore, the application of pressure can lead to the formation of new phases. It is relevant to note that these modifications are not merely laboratory artifices because the pressure varies in nature up to 60 orders of magnitude approximately from 10^{-30} to 10^{+30} atm. This significant pressure range allows to modify, only by the pressure effect, not only the aggregation state and the chemical-physical properties of the materials, but also their chemical structure [8]. High pressure experiments are commonly performed by using the *anvil cell*, allowing for static or dynamic compression measurements. Among this type of cells the Diamond Anvil Cell (DAC) is the most used, but also other materials, such as sapphire (SAC), can be chosen for anvils.

In a static compression measurement the T,P conditions of the sample contained within the anvil cell (static pressure cell) can be finely and independently controlled. Dynamic compression, instead, employs two different approaches: the dynamic anvil cell and the shock-driven experiments. The dynamic anvil cell (generally d-DAC) is a device which induces system modifications through ramps of variable pressure. In fact, it repetitively applies a time-dependent pressure profile to the sample, allowing for the study of the dynamic-pressure properties of materials [9]. Dynamic changes can be induced on long time scales by using the dynamic anvil cell where the dynamics of transformation is regulated by the continuous variation of pressure. By using this device the growth of ice VI and VII has been observed [10, 11]. The rate and topology of hydrates formation have also been obtained under dynamic compression in d-DAC [12]. In shock experiments the compression is generated by the use of *shock waves* induced by gas guns, explosive, or lasers. Thanks to shock compressions, phase transition boundaries up to extreme pressures and temperatures can be accessed [13–18]. Differently to static high pressure experiments, shock waves compression subjects materials to extreme conditions (very large compressions up to hundreds GPa, high temperatures, and large deformations) on very short time scales (picoseconds to microseconds), resulting in a rich array of physical and chemical changes. Structural transformations (including melting and freezing) in shocked materials and chemical reactions and decompositions in shocked energetic materials are just some of the scientific challenges in the field of dynamic compression. Due to the possibility to achieve in the laboratory the pressure and temperature ranges existing in the Earth's and other planets' interior, dynamic compression experiments take a special place in the study of planetary processes. Moreover, ultrafast measurements allow to investigate the material behavior and transformations under extreme conditions in real time, ranging from picoseconds to microseconds. For example, ultrafast x-ray diffraction at x-ray free-electron lasers has been lately used to investigate structural transformations during the solid-liquid phase transition under shock compression in systems like scandium, copper and fused silica [16–18]. Laser-driven shock compression experiments recently performed on water ice VII provides experimental evidence for superionic conduction in water ice at planetary interior conditions [19]. The possibility of providing great amount of energy on atoms or molecules on very short time scales allows to reach very high T,P conditions. Nevertheless, due to the shock, the pressure and temperature variation is significant and the transformation proceeds without the possibility to control P and T conditions independently. Differently to static high pressure techniques, during the shock a trend of defined T,P conditions (the Hugoniot curve) is followed by the system. In addition, a shock compression experiment is temporally dependent on the duration of the shock wave, that is the perturbation phenomenon. It is not possible to characterize the kinetics of phenomena faster than the perturbation itself. In fact, a fundamental requirement for studying a phase transition dynamics is the perturbation duration: the perturbation has to be faster than the dynamics under investigation.

Uncontrolled T,P conditions and perturbation duration are strong limitations in the investigations of phase transition dynamics. By changing the pressure, the static pressure anvil cell allows to set many different initial conditions (different starting crystal phases of the same molecule) and the problem is to change the temperature very rapidly (ps time scales) to induce the phase transition. For example, a fast perturbation (faster than the dynamics under investigation) can be obtained through a short duration laser pulse of suitable power matching an allowed transition thus providing the energy to heat the sample (*Thermal Jump technique – T-Jump*) [20, 21]. In this way the sample is heated from within, and nuclei of the higher-temperature phase can be homogeneously formed in the bulk, overcoming the dominance of heterogeneous nucleation induced by pre-existing defects or surface effects [22].

We have chosen to investigate the melting dynamics in water and water-based crystal structures, as water is a good model system, relatively simple and extensively investigated. Water, in fact, is the fundamental substance for the regulation of a wide range of biological, environmental, physical and chemical processes and is widespread all over our planet in several forms, from the well known gas and liquid states of matter to the solid one, which shows a remarkably high number of crystalline phases. Nevertheless, its dynamical, chemical and physical properties are not yet fully understood. The presence of strong hydrogen bonds [23] characterizes water and gives rise to peculiar structures in all the condensed phases. In fact, in addition to the well known hexagonal ice (ice I_h) which is generated by cooling liquid water at room pressure, water forms eighteen distinct crystal structures dependently on the environmental (T,P) conditions. The ice phases, which are particularly sensitive and modifiable by effect of high pressure, are reported in the phase diagram shown in figure I.1. The different ices are thermodynamic stable phases where water molecules are bonded to other four molecules through hydrogen bonds, but these tetrahedral structures can be distorted or regular giving rise to several three-dimensional networks depending on the protons disorder's degree [24]. Molecular arrangements lead to properties, such as density or heat capacity, that can be clearly distinguished.

Clathrate hydrates are another interesting class of water-based compounds generated only by pressure. They are complex crystal structures where water forms three-dimensional networks of different shapes and sizes stabilized by the repulsive interactions among the molecules contained inside the water cages. The guest species can be noble gases or small molecules, such as H_2, N_2, CO, CO_2 and hydrocarbons (CH_4, C_2H_6 etc). Among them, the most widespread clathrates, also

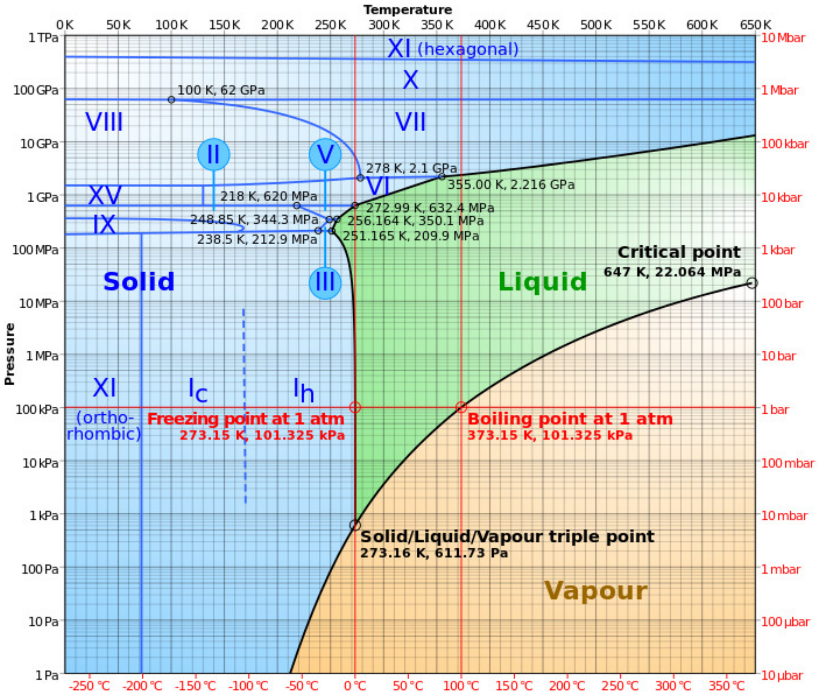

Figure I.1: Water phase diagram. The different solid phases of ice are shown. They differ in the arrangement of the water molecules.

important from applicative points of view, are the methane hydrates, originating at around 0°C and 0.1 GPa. They have a central role in the *carbon cycle* because of the great amount of carbon that can be stored inside them. For this reason they are a relevant fossil fuel source. The comprehension of the mechanisms regulating the formation and the decomposition of such systems is extremely relevant from an environmental point of view because methane hydrates are related to climate changes (*greenhouse effect*) due to the release of methane in the atmosphere. Moreover the comprehension of such mechanisms is fundamental for the exploitation of the carbon stored in these structures (energetic aspects), and also from a technological point of view because of their unwanted formation inside methane pipelines.

From these considerations derives that the knowledge of the phase transition dynamics of such systems (water and hydrates) is relevant both from a fundamental and an applicative point of view. Investigations which take into account the kinetics and the mechanism of the transformations in bulk systems at the same time are difficult to perform experimentally, and almost impossible for computational studies. Experimental studies are, in fact, strictly dependent on the sample features (volume, interfaces) and are often far from the thermodynamic conditions typical of the transition under investigation. For these reasons computational and experimental results often differ importantly and a rationalization of these differences is currently a fundamental issue in the study of phase transition processes. Among the experimental techniques, the time resolved pump and probe spectroscopy is employed to access the mechanisms of a system and the relative kinetics. The technique is able to provide information of the system even at molecular level, for example by following the evolution over the time of a vibrational band typical of the system. The technique employs two short laser pulses; one, the *pump* pulse, is used to induce the system excitation and generate a non-equilibrium state, and the other, the *probe* pulse, is used to monitor the pump-induced changes in the sample, allowing to obtain the system evolution over time.

In this thesis work a new strategy for the investigation of the dynamics of phase transitions in water-based crystal structures has been developed. The phase transition, and specifically melting, is induced by an energetic laser pulse having a duration of about 15 ps, which is absorbed by the sample (T-Jump technique). The crystal sample, which is kept in a cryostat at static T,P conditions, is homogeneously heated in a picoseconds time scale which is comparable to the intrinsic thermalization dynamics of water ice [5]. Within the pulse duration (15 ps), and the T-Jump itself, all the irradiated sample is (super-)heated. In this way, the perturbation is faster than the phase transition dynamics under investigation (the melting process). In order to monitor the dynamics of the transformation induced by the excitation event, two complementary probe techniques have been developed: the *Mie scattering* spectroscopy, which allows to follow the dimensional evolution of the molten domains generated in the superheated crystal lattice after the T-Jump, and the *transient infrared (TRIR) absorption* spectroscopy, which allows to appreciate the changes of a characteristic vibrational band of water (ices or hydrates). The Mie scattering technique has been used to monitor the system with a nanosecond resolution (due to the used photodiode) from the first nanoseconds after the T-Jump to tens of milliseconds. The TRIR spectroscopy, instead, having a temporal resolution of 100 ps, allows for the investigation of the system at shorter time scales. Together, these techniques are able to provide at the same time high temporal resolution in the firsts moments after the excitation and a wide time window of investigation. In this way, investigations of dynamics at short and long time scales can be performed, allowing for the monitoring both of the fast (melting) and the slow (refreezing) processes. In fact, the techniques allow to follow the system evolution, with the time resolution required for the dynamical processes under investigation. This is the first investigation of the dynamics of melting performed in the range 100 ps – 100 ms under controlled T,P conditions at the thermodynamic equilibrium of the system. Besides pure water (ice I_h and VI), we have tried to investigate also clathrate hydrates of methane and argon. The employed setups have been expressly designed to fit the requirements for sample compressed in a static pressure anvil cell, allowing for dynamics investigations of compressed samples, such as the several higher pressure crystalline phases of water and clathrate hydrates.

In Chapter 1 the experimental setups and techniques that have been developed and used in this work are reported and described. The first part focuses on the description of the Thermal Jump technique. In the second one the experimental setups used for all the measurements described in this thesis are reported. The last part is dedicated to the high-pressure devices.

In Chapter 2 a dynamics study on pure water ices in the mesoscopic regime is reported. Melting dynamics in ice I_h and VI from the first nanoseconds after the melting onset up to its completion (recrystallization) is explored by combining the T-Jump and the *Mie scattering* techniques. By monitoring the transmission variations of a continuous wave laser probe due to the scattering at the melt/ice interfaces inside the sample, the dimensional evolution of molten domains in the superheated crystal lattice can be followed.

Chapter 3 concerns the development of a synthesis technique for hydrates and a loading procedure in the anvil cell. A working procedure to synthesize clathrate hydrates of methane and argon in a high pressure apparatus, expressly designed for this purpose, has been developed. An homogeneous initial hydrate sample is a fundamental requirement for the dynamics investigations of melting and refreezing. The characterization by IR and Raman spectroscopy of clathrates and their phase transitions is also reported.

In Chapter 4 the results of TRIR absorption spectroscopy experiment on ice I_h relative to the first nanosecond after the T-Jump are reported. The source for the T-Jump is electronically synchronized with a femtosecond laser used as probe, allowing for the investigation of melting dynamics from 100 ps after the T-Jump. By monitoring the variations in time in the IR spectrum of a characteristic vibrational band of ices, the kinetics of the melting process and the direct quantification of the melted portion as a function of time can be obtained. These results paves the way to the investigation of the melting dynamics in clathrate hydrates.

The conclusion Chapter summarizes and closes this work.

CHAPTER 1

Experimental techniques & instrumentation

1.1 Thermal Jump technique

The *Thermal* or *Temperature Jump technique* (T-Jump) has been often used in dynamics investigations when a fast direct heating of the system is required. A fast perturbation of the system can be obtained through a laser pulse which is absorbed by the sample thus providing heat to the sample, increasing its temperature (T). The laser pulse energy has to be taken into account in order to induce the transition. In this way the sample can be heated from within, allowing to avoid an external absorber. The use of the external absorber does not allow to preserve the purity of the sample and to homogeneously heat the sample. These are fundamental requirements for our purpose and are assured by using a laser pulse. The duration of the perturbation is a fundamental requirement for studying the dynamics of a phase transition. The perturbation has to be faster than the dynamics under investigation, otherwise the measured dynamics would be strictly dependent on the heat transfer rate of the system, as in the case of external absorbers. This technique has been predominantly employed in the study of the dynamics of denaturation and successive reformation of protein structures in biological systems [25–27]. Also for dynamics investigations of condensate phase systems [28] and liquid water [21] the T-Jump has been successfully used. For water-based systems, both in pure water and in H_2O/D_2O mixtures, the laser pulse can induce vibrational excitations determining changes in the H-bonds network. The disruption and reformation dynamics of the H-bonds occurs in fs-ps time scales [29], and allows the thermal energy redistribution (*thermalization*). In this experiment the dynamics of the solid-liquid phase transition (melting) of water-based crystalline structures, such as water phases and clathrate hydrates of methane, has been studied by means of the T-Jump technique. Also the dynamics of other systems, such as benzene and ethylenediamine, has been taken into account.

1.1.1 Liquid water vibrational absorption spectrum

Liquid water is characterized by three internal vibrational modes (symmetric stretching ν_1, bending ν_2, and asymmetric stretching ν_3) and three external librations. In fact also in the vibrational spectrum of liquid water it is possible to observe bands corresponding to librations, which are typical of water ice structures. This is due to the molecules organization through H bonds making up a pseudo-lattice (pseudo-librations).

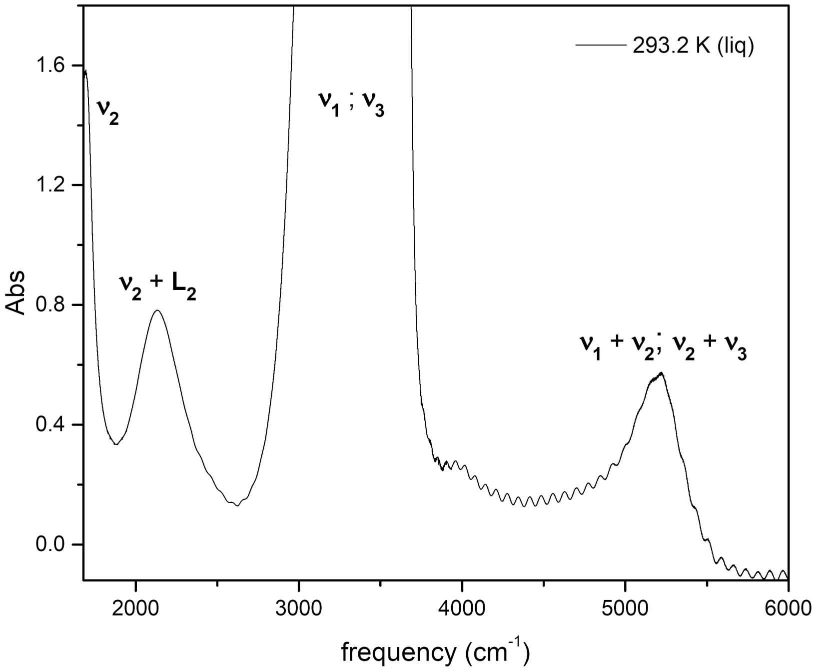

Figure 1.1: Liquid water vibrational absorption spectrum at ambient temperature and pressure. Sapphire windows (empty cell) are used as reference. The band at frequency lower than 2000 cm^{-1} is the water bending mode ν_2.

The vibrational spectrum region we are interested in is confined in the range 1600-6000 cm^{-1}, as shown in figure 1.1. At frequency lower than 1600 cm^{-1} the sapphire of sample cell windows absorbs the light, and diamond absorbs the wavelength of the T-Jump pulse, thus diamond windows cannot be used for our experiment. Within this range we can observe bands attributed to stretching ν_1 and ν_3, to the bending mode ν_2 and to several combination modes (see figure 1.1):

- The band centered at around **2200 cm^{-1}** is due to the combination mode of bending (ν_2) and libration (L_2). This band is dependent on the H-bond and therefore is sensitive to changes within the liquid structure [30].
- The intense band at **3400 cm^{-1}** is due to stretching (ν_1, ν_3). The ν_2 overtone band is in the same spectral range.
- The band at **5200 cm^{-1}** is due to combination modes of symmetric or asymmetric stretching.

1.1.2 T-Jump in ice

The laser pulse is sent to the crystal sample with the appropriate spectral features in order to be absorbed by water molecules. This involves the excitation of the molecular vibrational modes which occurs in fs time scales. The temperature of the system increases through the redistribution of the absorbed thermal energy (heat) via the vibrational relaxation over the lattice modes, allowing for the sample heating. Both the vibrational relaxation and the heat transfer contribute to the Thermal Jump lasting about 5 ps in liquid water [27] and 10-15 ps in ice [5]. However, the duration corresponds to the slower process between the pulse duration and the sample thermalization. This thermalization process is slower than the vibrational excitation because of the slow heat distribution among H bonds, and it can be slower in non-H bonded molecular crystals.

In this study the sample is heated in a ps time scale, contrary to previous works on biological systems which show longer (ns) time scales. In fact, the laser pulse duration ($\sim$15 ps) is comparable to the ice thermalization dynamics. This allows for dynamics investigations also of processes occurring in time scales comparable to the perturbation dynamics, for example the firsts moments of the phase transition as the melting, which is the process we are interested to study. In order to efficiently excite vibrations and heat the sample, the wavelength of the incident laser has been chosen to coincide with a relative maximum of a band of the water absorption spectrum (see figure 1.1). In particular, the excitation involves the region of combination modes $\nu_1 + \nu_2$ and $\nu_3 + \nu_2$, which corresponds to a broad band centered at around 5200 cm^{-1} (1930 nm). The width of such combination band is 525 cm^{-1} ($\sim$ 200 nm) obtained by fitting it with the Gaussian function. The simultaneous excitation of bending and stretching modes is realized by a single pulse, allowing for the efficacious transfer of the heat to the water molecules. The key point of the method is that the pulse, whose wavelength is resonant with a vibrational transition, allows the heat transfer from the pulse to the sample through intermolecular interactions. After the excitation of the water molecules the relaxation via external modes takes place increasing the vibrational amplitude of molecules with consequent temperature increase. If the laser pulse is highly energetic, it can be able to supply to the system the needed heat to induce the sample melting, that is the breakdown of the crystalline phase structure: the pulse supplies the energy for temperature increase and to overcome the latent heat of melting. It has been reported that the temperature can reach 330 ± 10 K [31] before the disruption of ice crystal lattice and the super-heated state generated in this way endures up to around 1 ns [32–34].

The pulse energy needed to increase the sample temperature of 1 K (E_{1K}) is given by the equation [35]

$$E_{1K} = c_p \rho \frac{V}{\alpha} \tag{1.1}$$

where c_p is the specific heat, ρ is the density, V is the irradiated sample volume, and α is the fraction of absorbed light.

In order to calculate the energy required to induce the melting of the irradiated volume of the sample, the melting latent heat of water (ΔH_{fus}) has to be taken into account in the equation. The values of specific heat, density, and molar latent heat of fusion of ice I_h and ice VI, used to calculate the amount of energy needed to heat by 1 K or to completely melt the irradiated part of the sample (the irradiated volume is $6.28 \cdot 10^{-6}$ cm^3 for both the ice samples) are listed in table 1.1.

	ice I_h	ice VI
ρ (gcm^{-3})	0.918	1.31
c_p ($Jg^{-1} \cdot K^{-1}$)	2.00	2.75
ΔH_{fus} ($kJ \cdot mol^{-1}$)	6.007	6.354

Table 1.1: Values used to calculate the amount of energy needed to heat by 1 K or to completely melt the irradiated volume (V) of sample for ice I_h and ice VI.

From these values, the energy needed to raise the temperature of the irradiated volume by 1 K is 11.5 μJ for ice I_h and 22.6 μJ for ice VI [36, 37]. The minimum energy needed for the complete melting of the irradiated volume at the melting point (i.e., the latent heat of fusion) is 1.92 mJ for ice I_h and 2.90 mJ for ice VI [38]. Thus, at the starting temperature conditions of the present experiment, the energy absorbed by ice (up to 4.7 mJ/pulse) in a single pulse is in principle sufficient to completely melt the irradiated volume and increase its temperature of some tens of kelvins.

Calculation of the saturation threshold for absorption

According to the T-Jump pulse duration (∼15 ps), a reasonable estimation is that no more than 50% of the total number of molecules (of the irradiated volume) can be found in the excited state. The threshold energy of absorption saturation (E) of a system can be calculated by the following equation

$$E = N_{molecules} \cdot E_{photon} \tag{1.2}$$

where $E_{photon} = h\nu$, is the photon energy at the typical absorption wavelength of the system (in the present experiment, for ice I_h is 1930 nm and for ice VI is 1960 nm), and $N_{molecules}$ is the number of excited molecules in the irradiated volume.

$$N_{molecules} = N_{moles} \cdot \frac{N_A}{2} \tag{1.3}$$

where N_A is the Avogadro constant and N_{moles} is the number of moles in the irradiated volume

$$N_{moles} = \frac{V \cdot \rho}{M_{mol}} \tag{1.4}$$

with the irradiated volume V, the sample density ρ, and the molar mass of the molecule M_{mol}.

For ice I_h, when the absorption wavelength is 1930 nm, the equation 1.2 provides a value of 9.9 mJ. For ice VI such value is 14.37 mJ.

1.2 Experimental setups

1.2.1 FT-IR

A Bruker IFS-120 HR spectrometer, specifically modified for high pressure experiments [39], has been used to perform infrared measurements. The spectrometer has been employed to characterize the samples, such as the different phases of ices and of clathrates, especially in the regions of the spectrum at around 2200 cm^{-1} and 5200 cm^{-1}. The samples under investigation have also been characterized through infrared measurements before and after the T-Jump experiment or other transformations in order to check the induced modifications.

The FT-IR apparatus, reported in figure 1.2, is equipped with source lamps for different spectral regions from about 5 up to 25000 cm^{-1}: a tungsten lamp for the visible/near infrared, a Globar for the MID-infrared range and a mercury lamp in the far infrared. It is also equipped with interchangeable beam splitters made of Mylar, KBr and CaF_2 and with four detectors: a bolometer (10-600 cm^{-1}), a mercury-cadmium-tellurium semiconductor (MCT, 500-6000 cm^{-1}), an indium antimonide semiconductor (InSb, 1850-9000 cm^{-1}) and a silicon diode (9000-32000 cm^{-1}).

Samples confined in an anvil cell can be accessed by spectroscopic techniques thanks to the transparency of the anvils. Nevertheless to avoid technical limitations due to the very small dimensions of the sample chamber, which is the gasket hole typically ranging in the hundreds μm, modifications of the original apparatus were necessary. In commercial instruments without an appropriate condensing system several reasons, like millimeter-sized infrared beams, the low brilliance of the medium infrared thermal source and low sensitivity detectors, make impossible performing measurements on such a small samples like those contained in an anvil cell. For this purpose the instrument employed in the experiments has been modified with a *beam condenser optical bench* equipped with ellipsoidal mirrors for focusing the IR spot on the anvil cell. The ellipsoidal mirrors allow a demagnification ratio of about a factor of 4 resulting in a waist on the focus slightly wider than the dimensions of the sample. This determines an effective enhancement of the transmission through the anvil cell of over than an order of magnitude. To remove the strong absorption due to atmospheric CO_2 and moisture, the spectrometer operates under vacuum or in an inert N_2 atmosphere. The Bruker IFS-120 HR spectrometer has a moving mirror with an arm of 3.0 m giving a

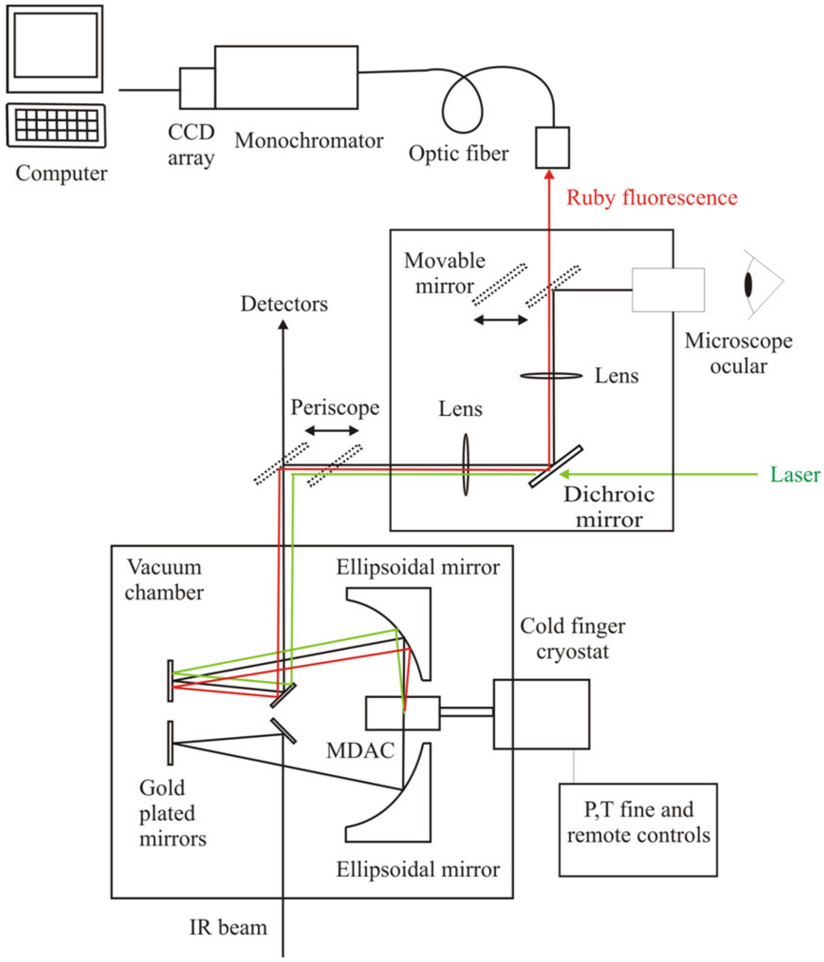

Figure 1.2: Scheme of the IR Setup used for infrared measurements and samples characterizations. It is specifically modified for high pressure experiments.

higher resolution than needed for high pressure measurements, where 1 cm^{-1} is the used spectral resolution. Moreover the instrumentation can be equipped for low and high temperature measurements. The low temperatures can be achieved by using a closed cycle double step helium compression cryostat, DE204SL by APD Cryogenics, coupled with the spectrometer. The high temperatures can be achieved by means of a resistive heater (600-700 K) that envelops the anvil cell. The pressure control can be remotely performed through a capillary which connects the pressure regulator outside the instrument to the membrane of the membrane-anvil cell inside the sample chamber. The pressure is in situ measured by the *ruby fluorescence method*, using a microscope that focuses few mW of the second harmonic of a continuous wave Nd:YAG laser on the ruby chip and collects, in a back scattering geometry, the fluorescence.

1.2.2 Micro-Raman setup

Raman measurements on this thesis have been performed using a custom setup especially designed to have a high spatial resolution.

The exciting source is a 641.7 nm emission line from a continuous wave Kr^{+} laser (Innova 300 by Coherent). A telescope is used to magnify the beam which is sent to a 50/50 beam splitter: the reflected part, focused by a 20X microscope objective, is sent to the sample contained in the membrane-anvil cell. The signal is sent back through the beam splitter and is collected in a back-scattering geometry by the same microscope objective. The scheme of the Raman setup is reported in figure 1.3. The combination of the magnified beam and the short focal length of the microscope objective ensure a beam waist in the focal plane of less than 3 μm and a depth of focus (Rayleigh range) in the order of few tens of μm. To further reduce the effective depth of field and the active diameter of the collecting system, a spatial filter, constituted by two confocal convex lenses of the same focal length and a 25 μm pinhole in their focus point, is placed before the detection. This allows to achieve a spatial resolution of 1 μm on the focal plane with a depth of field lower than 20 μm. This is fundamental for gaining the spatial resolution and thus avoiding the strong Raman diamond signal from the windows. The collected radiation is then filtered by two different notch filters to avoid excitation wavelength residues. The notch filter has a large rejection band that covers Raman shifts up to 200 cm^{-1}. The transmitted radiation is then focused onto the slit of the last stage of a triple stage monochromator equipped by a set of three gratings (300,

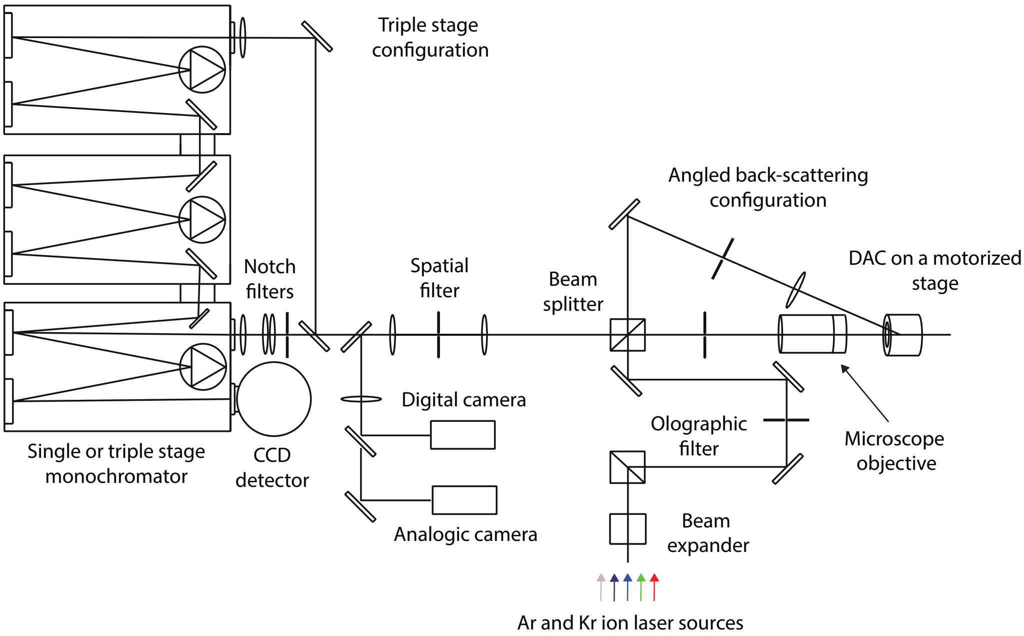

Figure 1.3: Scheme of the used Micro-Raman Setup.

900 and 1800 grooves/mm) giving a maximum spectral resolution of 0.7 cm^{-1}. The signal is detected by a 1024×1024 pixels liquid nitrogen cooled CCD placed on the exit of the third monochromator stage. The sample holder is provided with motorized micrometric movements which are software controlled, allowing automatic measurements and spatial sampling. This allows for fine translations on the focal plane of the sample with a precision of 1 μm.

1.2.3 T-Jump generation

The source described in this section is an optical parametric generator and amplifier (OPA) specifically built to obtain a ps Thermal Jump in water-based crystal samples [20].

The OPA provides for a pump pulse having the spectral and energetic characteristics required to excite the sample: the pulse can reach energies up to 15 mJ/pulse and its wavelength, around 1930 nm, is resonant with a vibrational combination band of water ($\nu_1 + \nu_2$; $\nu_3 + \nu_2$). A schematic view of the T-Jump setup, which is pumped by a Nd:YAG laser, is shown in figure 1.4. The pump beam for the OPA is the fundamental (1064 nm) of a 20 ps mode-locked Nd:YAG laser (Ekspla PL2143A) with maximum repetition rate of 10 Hz and energy up to 55 mJ/pulse. The beam is vertically polarized and has a collimated diameter of 8 mm. A 20/80 beamsplitter divides the pump beam, coming from the laser,

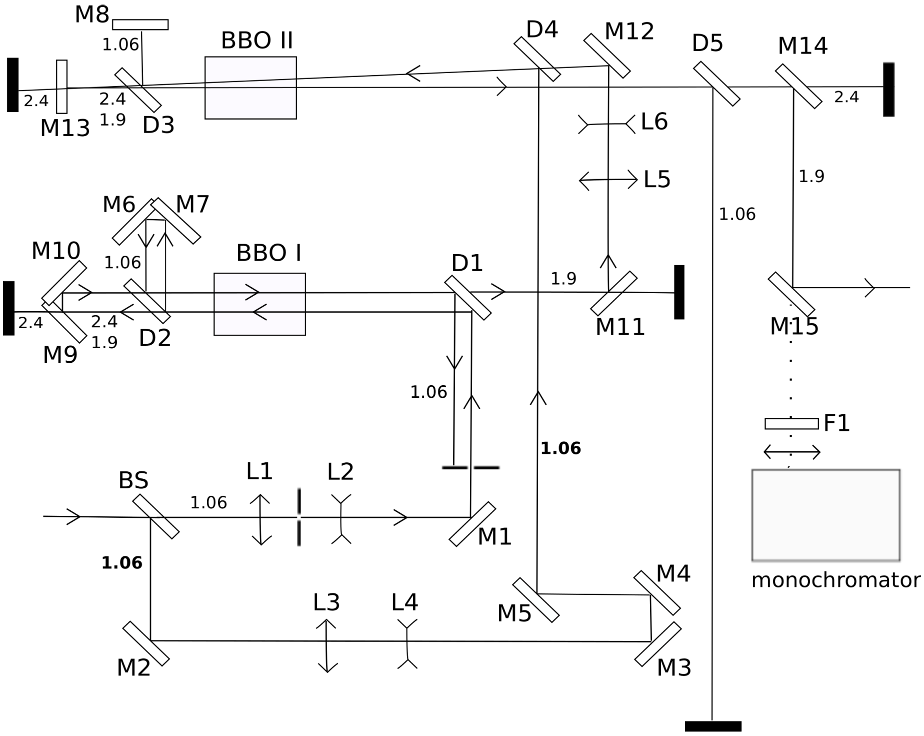

Figure 1.4: Scheme of the T-Jump Setup. Wavelengths present in the path are indicated in μm.

in two parts, which are respectively sent to the generation and the amplification path. The 20% of the beam transmitted by the beamsplitter is demagnified by a factor 0.25 on the beam diameter by a telescope (L1, f=100 mm, and L2, f=-25 mm). Two identical non linear crystals (BBO I and BBO II in Fig.1.4) for Type I generation allow for the light conversion 1064.0 nm (e) = 2371.3 nm (o) + 1930.0 nm (o), where 2371.3 nm and 1930.0 nm are the *idler* and the *signal* wavelengths, respectively. In order to excite a large population of the water sample, the generation parameters (angles, coating) have been chosen to generate a larger frequency bandwidth and a shorter pulse with respect to the pump pulse. BBO I is used for the 1930 nm generation and preamplification. The elements from M1 to M8 are highly-reflective mirrors at 1064 nm, and from M9 to M15 are highly reflective at 1900 nm. Dichroic mirrors D1 to D5 are highly reflective at 1064 nm on UVFS substrate, with anti-reflex coating at 1900 nm on both sides. After the first pass through BBO I, the pump is reflected by D2 whereas the signal and idler are transmitted. The idler is also transmitted by M9 to avoid its amplification in the second pass. Both the pump and the signal are reflected back by roof reflectors (one is mounted on a linear stage) into BBO I for the second pass. The roof reflectors also avoid any reflections back into the Nd:YAG laser. After magnification by a factor 2 (L5, f=-50 mm, and L6, f=100 mm), the preamplified 1930 nm beam is sent to BBO II spatially and temporally coincident with the 80% part of the pump beam reflected by the beamsplitter BS, and demagnified by a factor 0.6 (L3, f=250 mm, and L4, f=-150 mm) for a double amplification pass. The residual pump and idler beams are separated from the signal by reflection on D5 and transmission through M14, respectively.

The unamplified and amplified pulses can be independently sent to a 1/8 m monochromator (Spectral Products CM110) coupled to a large area MCT photoconducting detector (VIGO System) to characterize the spectral distribution of the output signal (Fig.1.5a). The source produces pulses tunable in the range 1700-2300 nm (FWHM = 100 nm), but the maximum conversion efficiency is found for phase matching at 1930 nm. The energy is measured with a pyroelectric detector (Gentec-Eo). The energy (mJ) at 1930 nm is reported in Fig.1.5b as a function of the pump energy. Maximum output energy is ∼ 25% of the pump energy. The autocorrelation profile (Fig.1.5c) has been measured by second

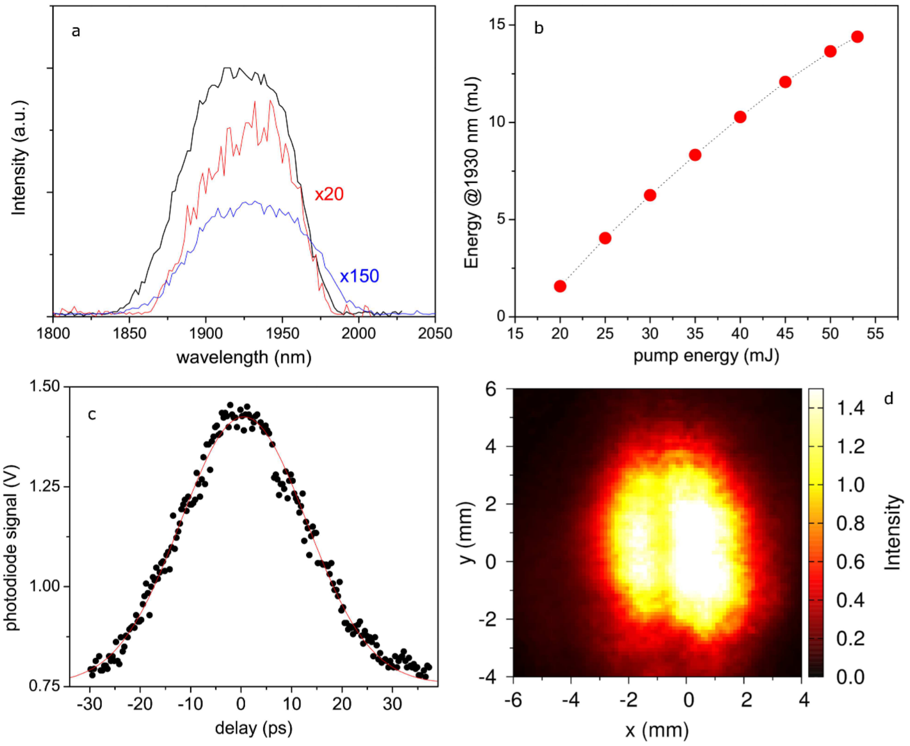

Figure 1.5: Characterization of the T-Jump beam. a. Spectrum of the output beam (in black), of the preamplified beam after the second pass in BBO I (in blue), of the beam after the second pass in BBO II in the absence of seed beam (in red). b. Energy/pulse at 1930 nm as a function of the energy/pulse of the pump at 1064 nm. c. Autocorrelation profile (see text). d. Spatial profile.

order autocorrelation, exploiting the two-photon absorption at 1930 nm on a Si photodiode (Hamamatsu S1722-02). The FWHM of the autocorrelation curve (fitted as a Gaussian profile) is 20.6 ps, corresponding to a pulse duration of ~ 15 ps. The spatial profile of the output beam, sampled by the MCT photo-conducting detector mounted on a motorized xy translation stage, is shown in Fig.1.5d.

1.2.4 Mie scattering experiment

The pump and probe experiment is the key experiment of this thesis for the study of phase transition dynamics (melting and refreezing) on water ices I_h and VI [40].

The pump pulse is an infrared radiation (1930 nm) responsible for the thermal jump (T-Jump pulse) of a 50-μm-thick ice sample. It is generated by an optical parametric generator and amplifier (T-Jump source) pumped by a mode-locked Nd:YAG laser.

The sample is probed by a monochromatic continuous wave laser beam. Different sources, ranging from UV to NIR, have been alternatively used for the probe beam. The scheme of the experimental setup is shown in figure 1.6.

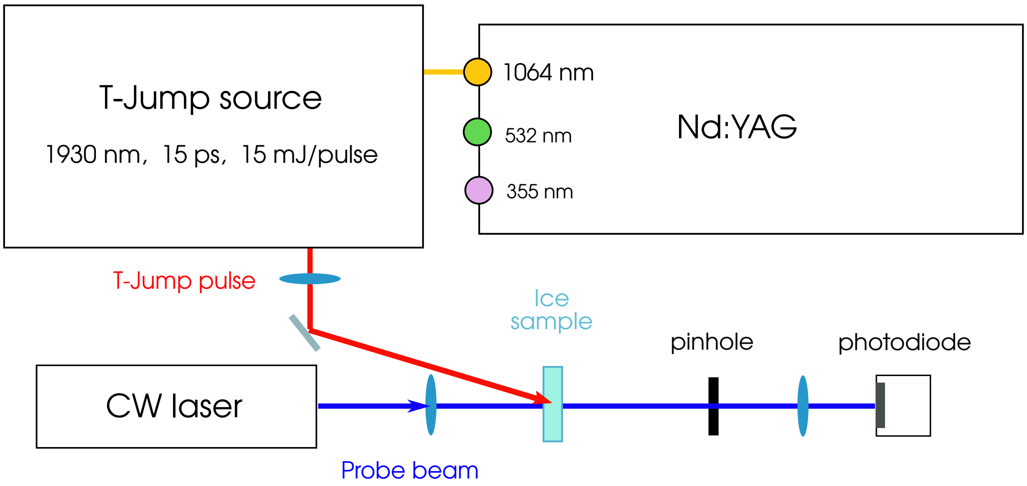

Figure 1.6: Scheme of the Mie scattering experiment. The T-Jump source, pumped by a mode-locked Nd:YAG laser, provides for the pump pulse (T-Jump pulse) that is sent to the sample. The sample is probed by a monochromatic continuous wave laser beam which is detected by a photodiode.

The pump and probe beams are sent to the sample with an angle of about 15°. This angle has been chosen to minimize the detection by the photodiode of any residual of the Nd:YAG laser radiation (1064 nm) in the T-Jump pulse, and also to preserve the overlap of the two beams in the anvil cell. At angle values larger than

15° the overlap is not guaranteed because of the anvil cell geometry determining the accessible angle.

The pulse at 1930 nm is focused (f = 500 mm) 50 mm far from the sample in order to have an irradiated diameter of $\sim$ 400 μm on the sample. The irradiated diameter is smaller compared to the entire sample diameter both for ice I_h and ice VI measurements. In the latter case the gasket hole of the anvil cell is responsible for the diameter of the entire sample (see paragraph 1.3.1). It is around 500 μm for all the dynamics measurements of this thesis. In the ice VI measurements, the (IR) T-Jump pulse is sent to the sample avoiding the irradiation of the metallic gasket (see 1.3.1 for Sapphire Anvil Cell).

The sample volume irradiated by the T-Jump pulse is due to the sample thickness (50 μm) and to the T-Jump pulse diameter which crosses the sample itself ($\sim$ 400 μm). In order to probe a portion of sample entirely irradiated by the T-Jump pulse, the probe beam is focused on the sample (f = 50 mm) to a focus diameter of $\sim$ 150 μm (the beam waist is calculated as a function of the probe laser wavelength). After the sample, the probe beam is detected by the photodiode (the 90% of its sensitive area is illuminated).

The absorbance of the ice sample under irradiation with the T-Jump source has been determined by measuring the transmission with a pyroelectric energy meter (Gentec-Eo), using as reference the empty cell. The absorbance is 0.55±0.30 for both types of ice (in agreement with the IR absorption spectra) and is constant for all the T-Jump energy range used, indicating that saturation of absorption is not reached even at the highest T-Jump energy.

Different continuous wave laser sources, ranging from UV to NIR, have been used to probe the sample, which does not absorb at any of these wavelengths. During the measurement, the laser power on the sample has been $\sim$ 5–10 mW. The employed sources with the relative wavelengths are reported in table 1.2.

CW lasers	λ (nm)
Ar+ (Coherent Sabre Innova 90)	457.9
Diode (Thorlabs CPS 405)	405.0
He-Ne (Melles Griot 25-LHR-691)	632.8
Nd:YAG (Lightwave 126)	1064.0

Table 1.2: The CW laser sources employed for measurements with the relative wavelengths.

Detection

The probe beam is detected by an UV-enhanced Si photodiode with cutoff frequency f_c = 60 MHz (Hamamatsu S1722-02). The UV-enhanced Si photodiode has an active area diameter of 4 mm. The spectral response of the photodiode is shown in figure 1.7. Among the used laser sources, the maximum photosensitivity is observed for the He-Ne laser (632.8 nm). According to its cutoff frequency, the photodiode has a rise time (10 to 90%) of about 1.3 ns and a discharge time of 3.2 ns. The FWHM of its instrument response function is around 5 ns. A filter at 1900 nm has been placed before the detector. The photodiode signal is monitored and recorded on a RohdeSchwarz 2-GHz oscilloscope (RS RT1024).

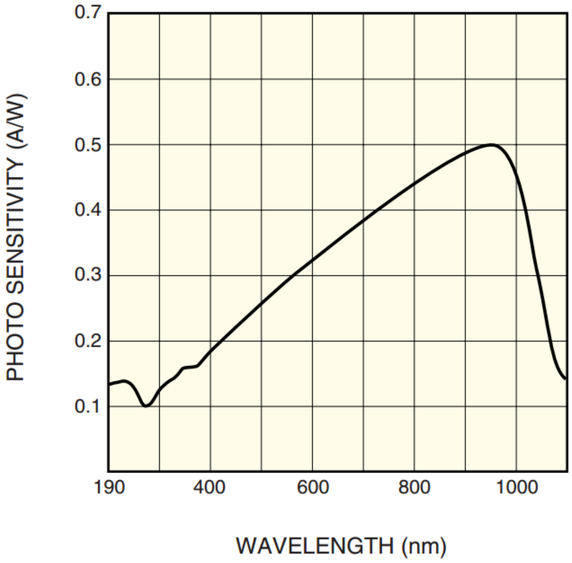

Figure 1.7: The spectral response for the UV-enhanced Si photodiode is shown. It covers a wavelength range from 190 to 1100 nm, with a maximum at 960 nm.

Different configurations of the probe detection

Different configurations of the probe detection allow for transmission or scattering measurements. The transmission or scattering is collected and focused on the photodiode, as in figure 1.8a or b, respectively.

For transmission, the transmitted light is the attenuation of the incident beam due to the scattering, a diaphragm (pinhole) with aperture $2 < \phi < 8$ mm (depending on the spatial shape and divergence of the probe beam) is placed close to the lens to collect light at a small angle with respect to the incident beam ($0 < \theta < 1.5°$).

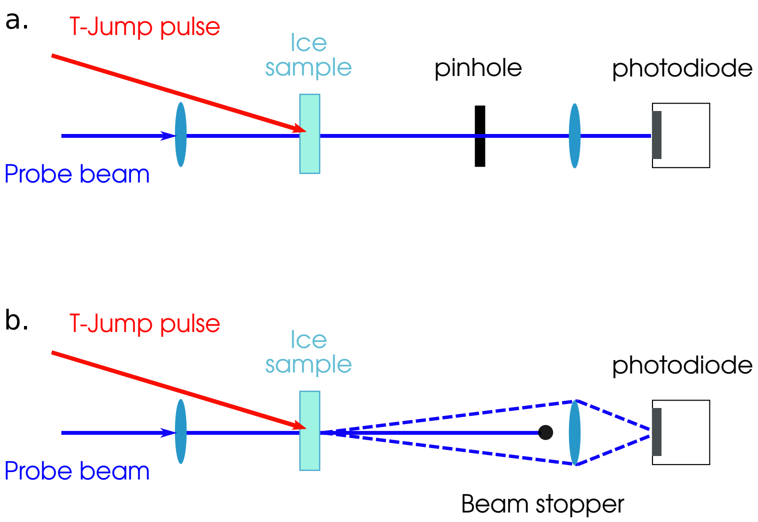

Figure 1.8: During the experiment the probe beam is collected in two possible configurations to detect the transmitted beam (a) or the scattering at $2^\circ < \theta < 7^\circ$ (b).

For scattering, the diaphragm is removed and a beam stopper is placed to stop the transmitted beam. The scattered light is collected in the entire angle ($2 < \theta < 7^\circ$), permitted by the collecting lens which has a diameter of 25.4 mm.

Sample chamber

Sample preparation Ice I_h and ice VI are prepared using water from Aldrich, HPLC grade, filtered with MillexVV Durapore PVDF syringe filters (pore size 0.1 μm). For ice I_h, the water is loaded in a room-pressure cell with fluorite windows and a polytetrafluoroethylene (Teflon) spacer. The spacer has a thickness of 50 μm and a diameter of 25.4 mm. The room-pressure cell is inserted in a Peltier cryostat and cooled to 250 K. The temperature is then increased to the desired T_0 value in the range 254.2–272.6 K. In fact, water is a metastable substance which requires to be supercooled at ambient pressure (or supercompressed at ambient temperature) to crystallize.

For ice VI, liquid water is loaded in a membrane Sapphire Anvil Cell (SAC - see 1.3.1) equipped with z-cut, low fluorescence sapphire anvils (Almax Easylab) and a copper-beryllium gasket. The sample is 50-μm-thick and 500 μm in diameter. The sample is (super-)compressed to 2 GPa at room temperature, and then the pressure is lowered to the desired P_0 value (1.2 GPa or 1.4 GPa). The fluorescence of a ruby chip with a diameter of 5 μm is used as a pressure gauge [41]. The purity of the so generated samples (ice I_h between fluorite windows and ice VI in the SAC) have been characterized by acquiring the FTIR spectra with the Bruker spectrometer described in paragraph 1.2.1.

Windows material Window materials with different thermal conductivity (sapphire and fluorite) have been used on ice I_h to check whether thermal diffusion through their surface could be the rate-limiting process. The measurement could provide different results in case of distinct window behavior regarding heat transfer and surface effect. The material in contact with the sample (window surface) can influence the dynamics under investigation, in particular the nucleation process. The surface effect, in fact, is responsible for heterogeneous nucleation.

The results shown in this work are independent of the windows material, consistent with thermal diffusion in ice/water (thermal conductivity: k $\sim$ 0.6 WK^{-1}·m^{-1} for water, k $\sim$ 2.2 WK^{-1}·m^{-1} for ice) being slower than through the windows (k $\sim$ 9 WK^{-1}·m^{-1} for fluorite (CaF_2), k $\sim$ 25 WK^{-1}·m^{-1} for sapphire) or at the window/sample interfaces (values for interfacial thermal resistance are not available).

In figures 1.9 and 1.10 the IR spectra performed on sapphire and fluorite, respectively, are shown. The empty cells have been used as reference for the measurements. Since fluorite and sapphire are not fluorescent and are transparent in the spectral region of our interest (2000-6000 cm^{-1}), they are valid materials for our measurements.

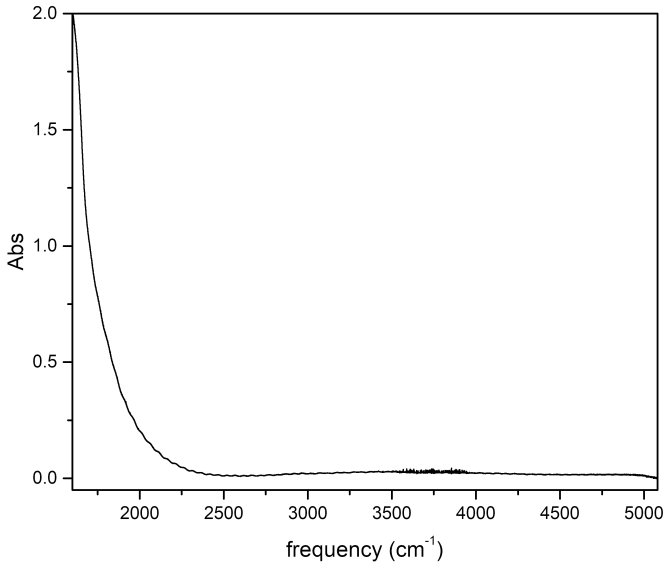

Figure 1.9: Infrared absorption spectrum of two sapphire anvils contained in the SAC. The thickness of one anvil is around 2.5 mm (thickness of empty cell is 5 mm). At frequency higher than 2000 cm^{-1} the sapphire doesn't absorb.

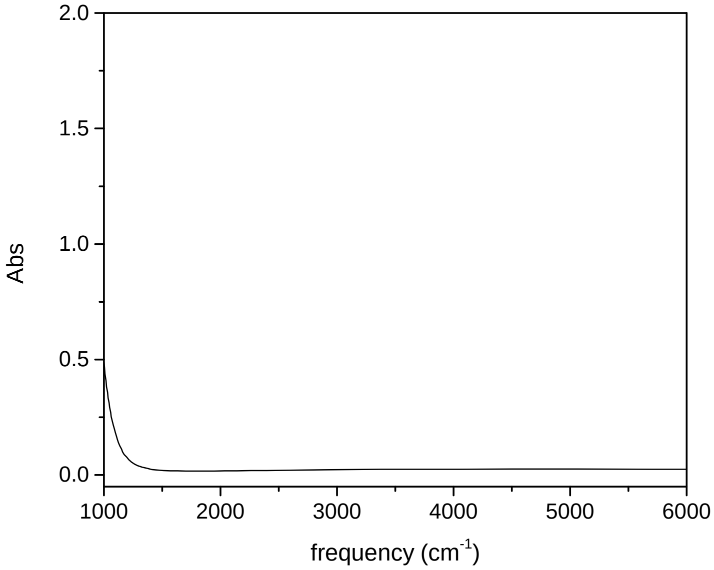

Figure 1.10: Infrared absorption spectrum of the two fluorite windows constituting the cell. The thickness of one window is around 2 mm (thickness of empty cell is 4 mm). At frequency higher than 1300 cm^{-1} the fluorite doesn't absorb.

1.2.5 Transient infrared absorption experiment

Transient infrared (TRIR) absorption has also been used to probe the sample after the Thermal Jump. This is a non classical pump and probe experiment and since the pump and the probe beams come from different sources they must be electronically synchronized.

The pump is a picosecond pulse and the probe is a femtosecond one. The pump pulse is the same infrared radiation (1930 nm) used in the experimental setup described in paragraph 1.2.4, which is responsible for the T-Jump of the sample. The pump pulse is focused on the sample in order to have an irradiated diameter of $\sim 400\ \mu$m on the sample. The same considerations (irradiated volume, angle between pump and probe, etc) reported in paragraph 1.2.4 can be done for the pump pulse employed for transient absorption measurements.

The sample is probed by an infrared femtosecond laser, allowing for the transient IR absorption spectroscopy. The scheme of the experimental setup showing the two sources is reported in figure 1.11. This kind of setup has been especially designed also to fit the requirements for sample compressed in a (sapphire) anvil cell. The IR pulse is generated by an *optical parametric amplifier* (OPA) pumped by a femtosecond Ti:sapphire laser. The pulse from the OPA source is filtered by an IR long pass filter (3.6 μm) to eliminate the residual signal

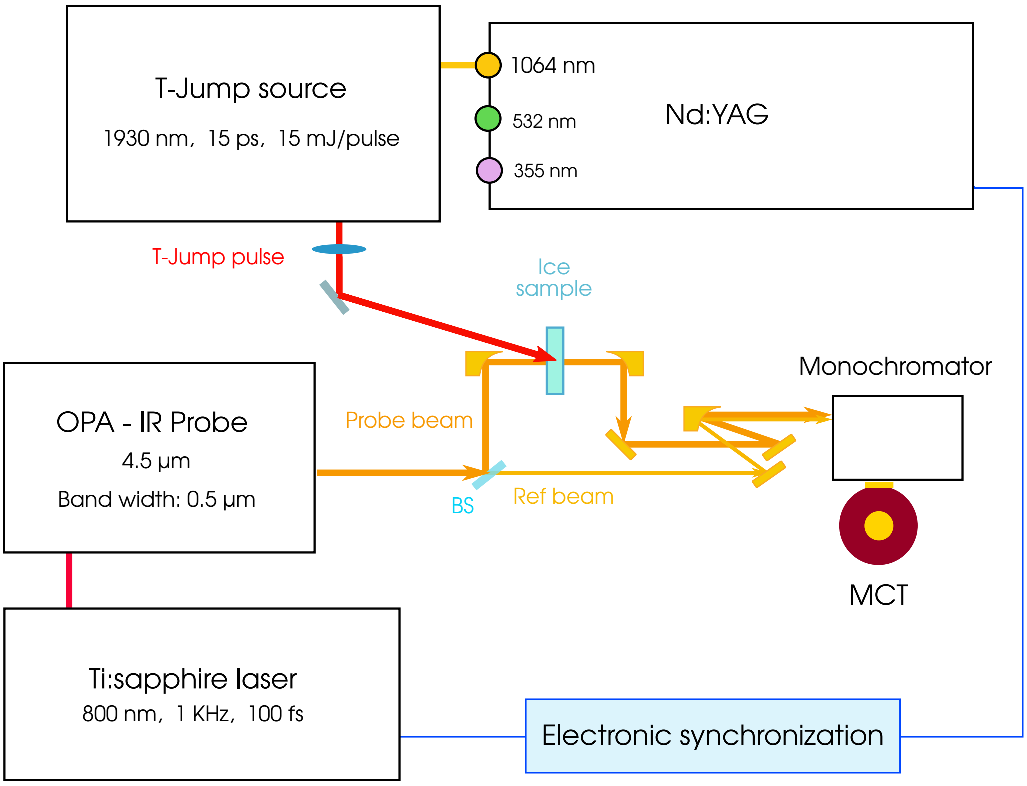

Figure 1.11: Scheme of the TRIR experiment. The T-Jump source, pumped by a mode-locked Nd:YAG laser, provides the pump pulse (T-Jump pulse) that is sent to the sample. The sample is probed by the TRIR absorption spectroscopy. The two femtosecond IR laser beams (probe and ref) are detected by a MCT detector.

and idler from the IR beam. Then it is divided in two arms with a 95/5 beam splitter (BS): the *probe* beam, which passes through the sample, and the *reference* beam, directly sent to the detector. The probe beam is focused on the sample by a 90° off-axis parabolic gold mirror with focal length of 50.8 mm in order to have a diameter of about 150 μm on the focal plane. The sample is kept at static temperature and pressure conditions between two fluorite windows in the cryostat for low temperature measurements. The probe and the reference beams are then focused on the monochromator with a 30° off-axis parabolic gold mirror with focal length of 108.9 mm. The MCT detector is a double 32 elements array (one for the probe beam and one for the reference). The ratio between the probe and the reference intensity (I_{probe} and $I_{reference}$ for each of the 32 elements of the MCT) allows to obtain the IR absorption spectrum of the sample, through the absorbance (A) equation

$$A = -\log \frac{I_{probe}}{I_{reference}} \tag{1.5}$$

The IR beam has a band width of about 0.5 μm centered at around 4.55 μm (2200 cm^{-1}). The IR band at 4.55 μm is the combination of bending and libration modes of water. The absorption band which is probed by the IR beam is shown in figure 1.12 for ice I$_h$ and liquid water.

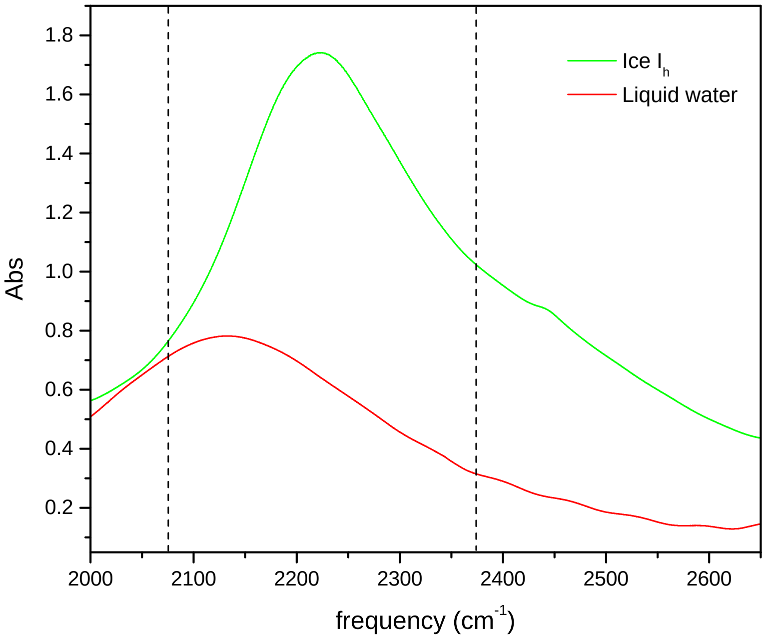

Figure 1.12: FT-IR absorption band of ice I$_h$ at 268.1 K in green and liquid water at 293.2 K in red. The probed region is delimited by black dashed lines. The spectra have been acquired with the Bruker spectrometer described in 1.2.1.

IR beam source

The IR beam source generating the probe and the reference beams is an optical parametric amplifier (OPA) which is pumped by a femtosecond Ti:sapphire laser.

The femtosecond laser system is constituted by an oscillator, whose pulses are amplified by a regenerative amplifier pumped by a Nd:YLF laser. The oscillator is a home made femtosecond mode-locked Ti:sapphire laser pumped by a 532 nm diode (OPUS). The Nd:YLF Q-Switched laser (YLF 621 D, BMI) is the pump laser for the amplification of the pulse coming from the oscillator. The output pulse features for the oscillator and Nd:YLF laser are reported in table 1.3.

	Oscillator	Nd:YLF
Pulse duration	100 fs	120 ns
Repetition rate	83 MHz	1 kHz
Emission wavelength	800 nm	523 nm
Power	350 mW	10 W

Table 1.3: Output features of the used oscillator and Nd:YLF laser.

The regenerative amplifier (Pulsar, Amplitude technologies) is a Ti:sapphire laser based on the chirped pulse amplification of the ultra short pulse coming from the oscillator. The output features of the beam are reported in table 1.4.

	Regenerative amplifier
Pulse duration	100 fs
Repetition rate	1 kHz
Emission wavelength	800 nm
Power	550 mW

Table 1.4: Regenerative amplifier output features.

The OPA is a home made setup needed to convert the 800 nm radiation to the MIR region. In fact this setup is able to generate, due to non linear phenomena, a MIR radiation from 3 to 10 μm [42]. The OPA source is constituted by three different arms which can be seen in the picture of figure 1.13: the *Seed* line (in green), *Pre-amp* (in yellow) and *Amp* (in orange) arms.

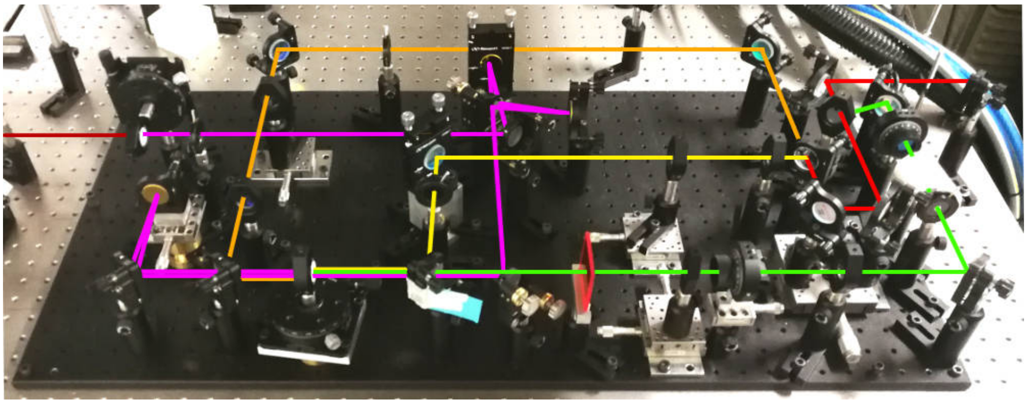

Figure 1.13: Picture of the *Optical Parametric Amplifier* setup (OPA) generating the IR beam. In red is reported the 800 nm radiation. The *Seed* line is reported in green, the *Pre-amp* arm in yellow and the *Amp* arm is in orange. Magenta and brown indicate, respectively, the signal and idler pathways and the MIR radiation.

In the Seed line the 4% of the 800 nm radiation is sent to a λ/2 plate and to a plate polarizer at Brewster angle in order to rotate the polarization of 90°. The radiation is then focused on a 1-mm sapphire window in order to obtain a single-filament white-light continuum, which is the seed for the pre-amplification stage in a type II β-barium borate non-linear crystal (BBO) together with the Pre-amp beam. A 90/10 BS divided the 96% of the 800 nm radiation in the amp and the pre-amp arms, respectively. The Pre-amp beam is focused on the BBO crystal and, together with the white-light continuum, is responsible for the generation and pre-amplification of the signal and the idler frequencies (magenta line). The *phase matching* condition is realized by the delay stage in the pre-amp path and to the BBO crystal orientation. The Amp arm is responsible for the signal and idler amplification with a second pass in the BBO. Due to a spherical gold mirror, the second pass is lower in height in the BBO crystal. The spherical gold mirror is mounted on a delay stage allowing for the temporal superimposition of the two beams in the BBO. The two amplified signal and idler (NIR) frequencies are then sent, temporally and spatially recombined thanks to a third delay line, to a 1.5-mm-thick type I $AgGaS_2$ non-linear crystal. The MIR radiation (in brown) is obtained in the crystal by the *Difference Frequency Generation* (DFG) of the signal and the idler frequencies. A radiation conversion in the range 3 to 10 μm is allowed by the orientation of the type II BBO and the type I $AgGaS_2$ crystals.

Detection

The probe and the reference beams are focused on the slit of a monochromator (TRIAX 180, Horiba) equipped with a plane mechanically ruled grating (100 gr/mm, 6 μm blaze wavelength), allowing for a free spectral range of 180 cm^{-1}. They are then detected by a liquid nitrogen cooled HgCdTe (MCT) detector (InfraRed Associates, Inc.) equipped with 64 elements. It is a double array of 32 pixels with element size of 0.2 mm$\times$0.5 mm. The MCT array has a wavelength response in the range 2-10 μm. The higher element sensitivity is around 8 μm. The entire detection system (monochromator and MCT) allows a spectral resolution per pixel of around 5.8 cm^{-1}. The MCT electronics has been designed and built in our laboratories in order to couple the detector to the 1 kHz source (Nd:YLF laser repetition rate).

Sources synchronization

The ps T-Jump source (pump) and the fs IR source (probe) are electronically synchronized: the 1-kHz laser (Nd:YLF) is the *master clock* for the laser sources synchronization. A *delayed frequency divider* (DFD), triggered by the 1-kHz laser, generates a delayed TTL with duration of about 100 μs, as reported in the synchronization scheme of figure 1.14. The DFD allows to choose the delay in the range 100 to 999 μs with microsecond resolution. The DFD is designed to generate the delayed TTL and wait for 99 pulses of the master clock laser before repeating the cycle, resulting in a 10 Hz TTL. In this way the sources synchronization over the time is ensured. The so generated delayed TTL is the external trigger for the ps Nd:YAG laser pulse which pumps the T-Jump source. Due to the lamps discharge, the Nd:YAG laser has an intrinsic delay: it shoots the ps pulse with a fixed delay of $\sim$1.39 ms. Moreover, the delayed ps shot is a stochastic event which happens with a characterized Gaussian distribution function having a 6σ band width (99.74% calculated over 1000 pulses) of 2.7 μs, as shown in the third line of figure 1.14. By regulating the delay of the TTL on the DFD, the shot from the Nd:YAG laser, which is responsible for the pump pulse, can be finely delayed with respect to the clock pulse. In this way the pump pulse (the Gaussian distribution function center) is temporarily coincident with the third pulse of the 1 kHz laser, responsible for the probe pulse, allowing for pump and probe time superposition.

In order to perform the pump and probe measurement at a certain delay

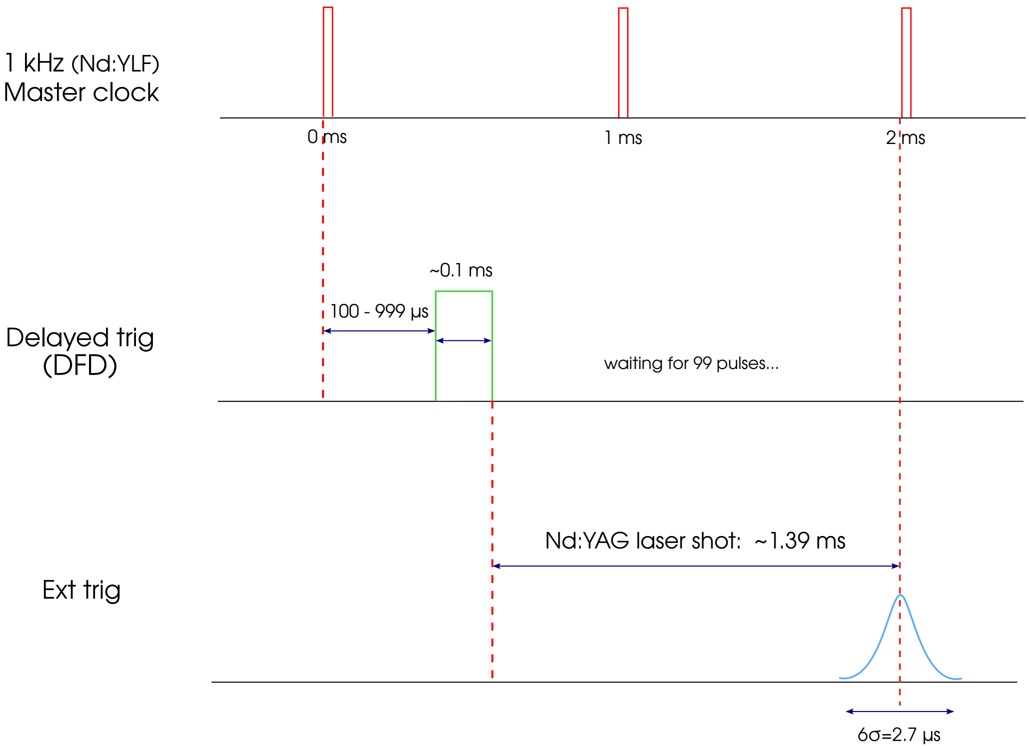

Figure 1.14: Scheme of the electronic synchronization between the two laser sources. The master clock is the 1-kHz laser (Nd:YLF).

time Δt between the pump and the probe pulses (with $\Delta t = t_{probe} - t_{pump}$), both the Gaussian distribution function and the TTL delay must be employed. The Gaussian distribution function has a width which covers a time window of 2.7 μs. In addition, the TTL delay can be regulated on the DFD in order to control the Δt, allowing for pump and probe measurements at short or long time scales respect to the pump pulse. The delay time Δt (see figure 1.15) is optically detected and measured by the oscilloscope. The ps T-Jump pulse (pump) and the fs Ti:sapphire laser pulse (probe) are detected by two identical UV-enhanced fast Si photodiodes, and the delay between the pulses is precisely measured by the oscilloscope (with an estimated error of $\sim$100 ps). The pump pulse is used as trigger for the measurement of the delay. It is also used as external trigger for the acquisition of the probe and the reference spectra detected by the MCT detector. In particular, the ADC is armed by the pump pulse to acquire the probe and the reference pulses detected by the 32×2 elements of the MCT. A software program has been written in order to couple the acquired probe and reference spectra to the corresponding measured delay time Δt.

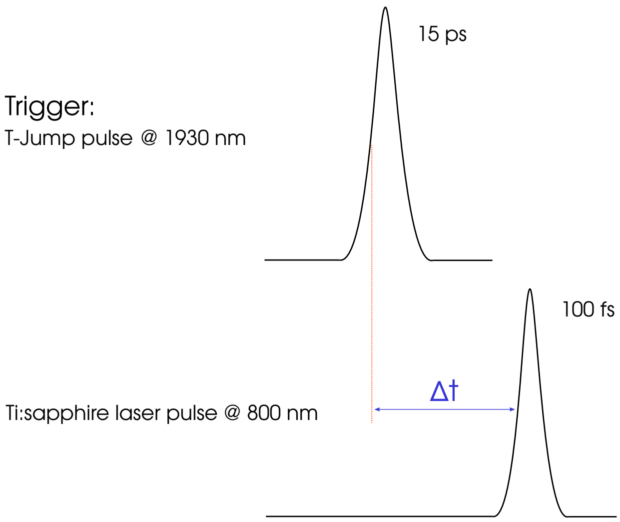

Figure 1.15: Delay time Δt between the T-Jump pulse (pump) and the Ti:sapphire laser pulse (probe). The delay is measured by the oscilloscope. Due to the photodiode response function, the FWHM of the two peaks is enlarged. The pump pulse is used as trigger for the measurement of the delay.

The experiment consists in *single shot* measurements performed with a repetition rate of 1 Hz. In each measurement a single pump pulse is shot and a couple of probe and reference pulses are acquired. The absorbance of the sample is calculated (equation 1.5) in order to obtain the IR absorption spectrum for each measured Δt. The entire dynamics of the investigated process, which is stochastically sampled, can be reconstructed by multiple series of single shot measurements. The method is able to provide for high time resolution ($\sim$100 ps) and a wide time window (in the range 100 ps potentially up to infinity) of investigation at the same time. The time resolution has been obtained by detecting the pulse at 800 nm with two identical photodiodes. The distribution of the delay time between the same pulse detected by different photodiodes over 1000 pulses has a width of about 100 ps.

1.3 High-pressure devices

1.3.1 The Anvil Cell

The *anvil cell* is commonly used in the study of systems at high pressure. This device is able to generate static pressure on small volume samples. Dependently on the geometry of the cell and on the anvil material a very wide range of pressure can be reached up to hundreds of GPa [43]. By resistive heating, it also allows to work in the temperature range from 10 to 1300 K.

The sample chamber is limited laterally by a metallic gasket, preindented and drilled by spark erosion, placed between the anvils to confine and hold the sample. Sample sizes typically range from 100 to 400 μm of diameter and around 50 μm of thickness. The most used anvil cell is the Diamond anvil cell (DAC), but several materials are suitable to be used as anvils, such as sapphire, tungsten carbide, synthetic diamonds etc.

In all the measurements of this thesis a particular kind of anvil cell is used to generate high static pressure: the membrane anvil cell, where the pressure is applied on the anvils by the dilatation of a metallic membrane which is inflated by an inert gas at low pressure, such as Helium (figure 1.16). Solid and liquid samples can be directly loaded between the anvils, inside the gasket sample chamber. Then the cell is closed and pressure is externally applied by the *Pressure Driving System*.

The pressure experienced by the sample inside the cell can be monitored by the Ruby fluorescence method [41, 44, 45], adding a small ruby chip as a sensor together with the sample. Alternatively, in the DAC, the pressure shift of the D band of diamond in the Raman spectrum can also be used.

The anvil material must be transparent to the radiation sent to the sample and must present the needed hardness to reach high pressure without fractures. In an anvil cell the anvils are the transparent sides of the sample cell and guarantee the optical access through the sample allowing for spectroscopic measurements.

In our dynamics investigations, the sapphire has been used for anvils. This is due to the very high energy of infrared pulsed light required during measurements which is absorbed by the diamond leading to severe damage of the anvil.

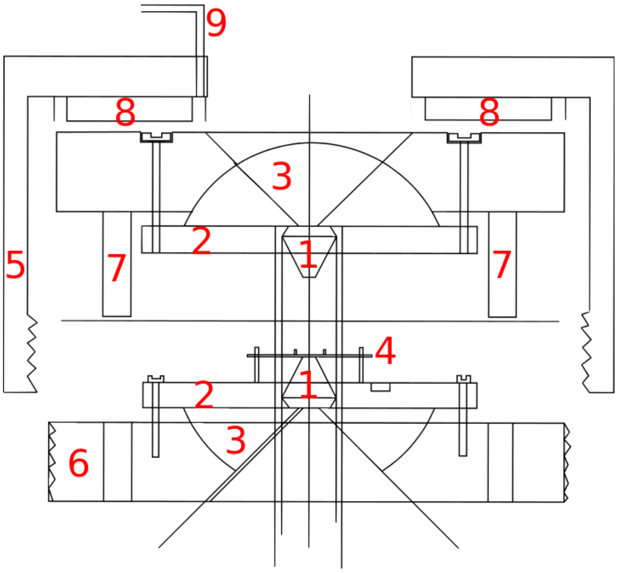

Figure 1.16: Schematization of a membrane Diamond Anvil Cell (mDAC).

1 - Diamond	2 - stainless steel platform
3 - tungsten carbide hemisphere	4 - gasket
5 - upper semi-cell	6 - bottom semi-cell
7 - stainless steel rectified spines	8 - stainless steel membrane
9 - stainless steel capillary	

Sapphire Anvil Cell

The sapphire has a high optical transparency in a wide spectral region: sapphires are transparent from the near IR to the UV, and they strongly absorb at energy lower than 2000 cm^{-1}. In the spectral region of our interest (see figure 1.9), that is between 2200 and 5200 cm^{-1}, sapphire has a negligible absorption. This material is not fluorescent.

The material constituting the anvils of a cell used for high pressure experiments must possess mechanical properties (mechanical strength and hardness) necessary to endure high pressures. The anvils geometry determines the maximum pressure that can be reached in the cell. Sapphires with truncated-conical geometry have been used for our experiments. The used sapphires have thickness of 2.5 mm, base diameter (big surface) of 4 mm and culet diameter of 950 μm.

Sapphire is second in hardness compared to diamond, and, with our geometry, is able to endure pressure up to 5 GPa. The used anvils come from a single crystal of sapphire which is free from structural defects, which could compromise its mechanical strength, and free from chemical impurities, which could introduce spectral interferences with the sample and with an eventual source in spectroscopic investigations. The sapphire employed for our high-pressure measurements is an optical-axis-oriented monocrystal. It has no birefringence along that axis. The sapphires we used had a well polished surface. Moreover, they have been selected to meet the requirements for our experiment. From the point of view of optical properties, sapphires have been selected for working in the medium infrared: low absorbance in that spectral region, as previously shown in figure 1.9. From a mechanical point of view, we tested sapphires with different geometries selecting the truncated cone one. Their resistance under irradiation with the high energy T-Jump pulses has been tested, being a required measurement condition.

1.3.2 High pressure reactor

A working procedure to synthesize clathrate hydrates has been developed. The synthesis is performed in a high pressure apparatus especially designed for this purpose.

The autoclave, which is shown in figure 1.17, has been realized by the mechanical workshop at LENS. It is made of steel and has a cylindrical sample chamber of about 25 cm^3 (diameter of 25 mm and height of 50 mm). The cylindrical chamber is closed on both sides by screwed flanges. The sealing is guaranteed by

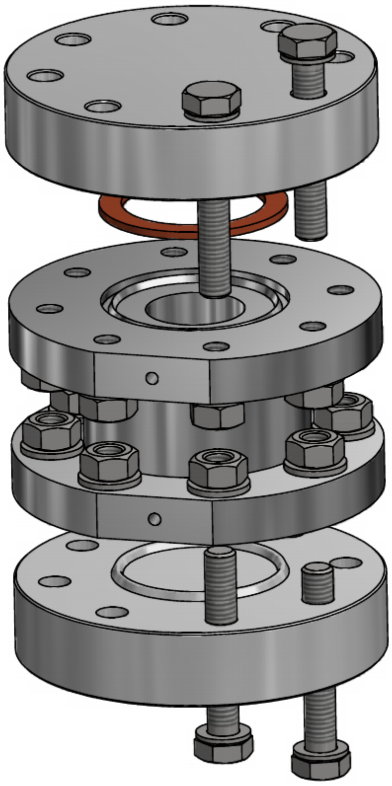

Figure 1.17: High pressure autoclave especially realized and used for the synthesis of clathrate hydrates.

two copper o-rings covered with silver. The chamber is connected to a vacuum pump and to a gas tank to load pressurized gas directly inside the vessel. In order to monitor the pressure during the process, a pressure gauge is also attached.

Synthesis procedure

In order to synthesize clathrate hydrates, the procedure proposed by Stern et al. (see Chapter 25 of the book *Natural Gas Hydrate* [46]) has been followed as a guideline.

The synthesis of clathrate hydrate has been performed in the high pressure (400 bar of gas) reactor, starting from finely ground ice and gas (methane or argon). Ice, obtained from distilled water, has been crushed and ground by hand in a mortar cooled at the liquid nitrogen temperature. About 10 g of such ice have been loaded in the already cold reactor refrigerated with a mixture of solid/liquid ethanol at 160 K. A porous filter paper disk has been put to prevent the formation of ice along the connections to the gas tank or the vacuum pump, and the reactor has been sealed. The cold reactor has been pumped for a couple of hours, then the (methane or argon) gas has been loaded inside the reactor kept at 160 K in the ethanol bath. The gas pressure has been raised up to 200-220 bar at this temperature. Screws need to be tightened at low temperature for a correct sealing. After about 30 minutes, the reactor has been transferred into the chiller at -33°C. The temperature program, which are reported in table 1.5 for clathrate hydrates of methane and in table 1.6 for clathrate of argon, has been started.

from	to	time
-33°C	-29°C	30 min
-29°C	-2°C	1 h
-2°C	+7°C	2 h
+7°C	+17°C	2 h
+17°C	+17°C	36 h

Table 1.5: Temperature program for the synthesis of clathrate hydrates of methane.

When the temperature approaches the melting temperature, if the pressure inside the autoclave is greater or equal to 300 bar, the clathrate formation takes place. After the heating to -2°C, pressure raised up to about 400 bar for the case of methane, and an argon pressure of $\sim$350 bar has been found after the heating

from	to	time
-33°C	-4°C	3 h
-4°C	+2°C	12 h
+2°C	+2°C	6 h

Table 1.6: Temperature program for the synthesis of clathrate hydrates of argon.

to -4°C. After the temperature cycle, the pressure decreased to ~370 bar for methane clathrate and to ~200 bar for argon clathrate. The temperature has been lowered to -33°C in the chiller, then the sample has been quenched in liquid nitrogen. The reactor has been unsealed in liquid nitrogen and nitrogen atmosphere. The product, which is very highly unstable at ambient temperature, appears as fine white flakes. The generated clathrate has then been stored at -80°C in a freezer.

Loading procedure

Methane clathrate hydrates (loading in DAC) A diamond anvil cell (400 μm culet diamonds, inconel gasket drilled at 150 μm diameter, and 70 μm of thickness) with a ruby chip has been cooled down in liquid nitrogen and dry atmosphere, then an amount of sample has been rapidly pulled out and put over the gasket. The cell has been rapidly closed and pressurized with 20 bar in membrane.

Pressure after the loading was 5.30 GPa at room temperature. The P,T conditions are in the stability range of the MH-III (filled ice) phase of methane clathrate hydrates [12].

Argon clathrate hydrates (loading in SAC) A sapphire anvil cell (950 μm culet sapphires, Cu-Be gasket drilled at 450 μm diameter, and $\sim$ 60 μm of thickness) with some ruby chips has been cooled down in liquid nitrogen and dry atmosphere, then an amount of sample has been rapidly pulled out and put over the gasket. The cell has been closed and pressurized with 13 bar in membrane.

Pressure after the loading was 2 GPa. Membrane pressure has been released to 0 bar and raised to 2.9 bar: the pressure inside the sample was 0.64 GPa at room temperature. The P,T conditions are in the stability range of the h_1 phase of the argon clathrate hydrates [47].

CHAPTER 2

Phase transition dynamics by Mie scattering

2.1 Introduction

A phase transition is characterized by the change of the chemical potential (μ) of the substance, which is a measure of the potential that a substance has for undergoing physical change in a system [48]. For a one-component system it corresponds to the molar Gibbs energy (G_m) of the substance. From its behavior, according to the Ehrenfest classification, it is possible to classify phase transitions into different types. The transitions have implications for the slopes of the phases' chemical potentials on both sides of the phase transition. In particular, the classification is based on the lowest order of derivative of the chemical potential with respect to temperature which presents a discontinuity: that order is the order of the phase transition. Many familiar phase transitions are *first-order* transitions, such as crystallization and melting. They are accompanied by changes of enthalpy and volume. All these transitions need to overcome a free-energy barrier, corresponding to the work for the formation of a nucleus of the new phase. *Nucleation* is the starting mechanism and involves the formation of stable (micro- or smaller) structures which are the "germs" or "nuclei" of the new phase that appears within the pre-existent phase [49]. The initial step of the phase transition determines the final structure of the emerging new phase. This phenomenon is possible if the atoms or molecules constituting the material can diffuse through the material itself to aggregate and thus form the nuclei of the new phase. In the case of crystallization, according to the classical nucleation theory, the process is regulated by the competition between the energy gain due to the liquid-solid transformation and the loss associated with the formation of the liquid-crystal interface. This explains why certain materials in the liquid phase pass to a state of metastable equilibrium (*supercooling*) [50–53]. This process can be observed also in pure liquid water which can be cooled at room pressure down to its melting temperature until about -42°C without observing solidification [54]. At this border ("stability limit" for supercooled water [55]) the liquid phase is not kinetically stable anymore and water crystallizes in the thermodynamic stable form through homogeneous nucleation. For the same principle, liquid water can be compressed up to about 1.4 GPa at room temperature, while at 1 GPa it should crystallize as it can be seen from the water phase diagram of figure 2.1 [56]. The observation of homogeneous or heterogeneous nucleation strictly depends on the kind of system, the supercooling degree, the purity and the state of stillness of the investigated system [57]. After the nucleation process, the growth of the so-formed stable nuclei into macroscopic domains occurs.

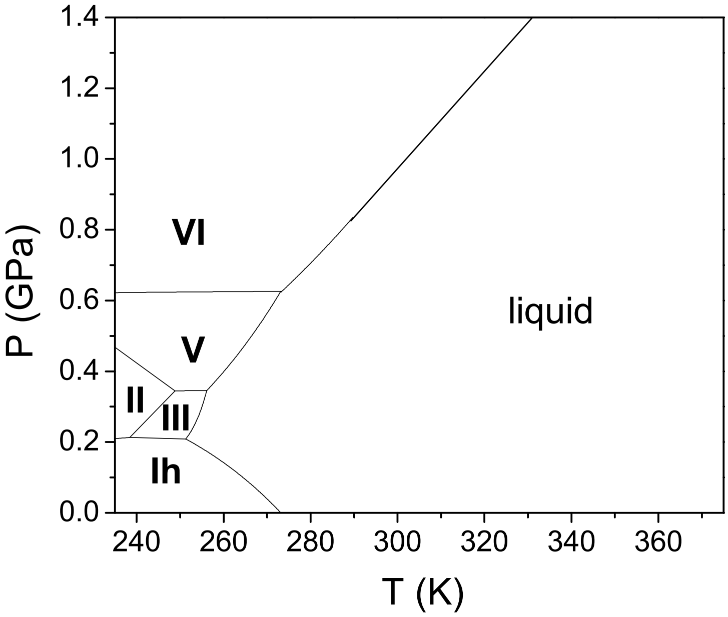

Figure 2.1: Water phase diagram [56]. The figure shows some phases including ice I_h and VI.

In this chapter a method to investigate phase transitions dynamics in water ices is described. In the following, two among the most common first-order phase transitions, such as melting and crystallization, will be taken into account in the attempt to go deeper into the comprehension of their dynamics.

The melting process is characterized by the disruption of the crystalline order and the achievement of the local structure of the (disordered) liquid phase, but its mechanisms at molecular level and the relative characteristic time scales are not well elucidated, as for any other phase transition. The melting mechanisms have been addressed by several theoretical and experimental works which cover a sub-nanoseconds time window with typical sample sizes of tens of nanometers. In fact in the attempt to explain the fundamental mechanisms of the transition onset, the dynamics of melting have been studied up to the present in the picoseconds time scale, allowing for the observation of structural changes on a length scale of few nanometers. In order to access these very short time scales, both in simulations and experiments, micro- or submicro-sized crystals are rapidly heated above the melting temperature (T_m) into a *super-heated* state, where the melting occurs [5–7, 31, 58]. Metals and water ices have been employed as test systems for melting investigations. Experimentally, the system can be rapidly heated by a pulse of infrared light at a wavelength that the sample can absorb (T-Jump technique). In this way, the sample is heated from within, and transition nuclei can be formed in the bulk, overcoming the dominance of heterogeneous nucleation, induced by surfaces effects or pre-existing defects [22]. At temperatures approaching super-heating, in fact, it has been discovered that melting becomes a single barrier-crossing process, revealing the importance of non-local behavior [7]. The sample temperature increases through the redistribution of the absorbed energy via the vibrational relaxation over the lattice modes. This thermalization process takes $\sim$15 ps in water ice [5] and can be slower in non-H bonded molecular crystals. The structural changes following the heating pulse have been monitored in 20-nm-thick aluminum [3] and gold [4] samples by electron diffraction, where the main signal of melting completes in a few picoseconds. The melting dynamics in 1.6-μm-thick ice I_h (the room pressure and low temperature water phase) after an ultrafast T-Jump has been studied over a time window of 250 ps by time-resolved infrared absorption spectroscopy [5, 31, 32, 34]. The spectral changes attributed to melting occur in the first 150 ps after the pulse (time constant $\tau = 37$ps). An incomplete melting is still observed within that time window (250 ps), consistent with the amount of energy delivered by the pulse which is not sufficient to fully melt the sample. All these experiments are thus suitable to determine and investigate the onset of the process, but they are unable to unveil the successive dynamics.

The knowledge at the picoseconds-nanometer scale barely connects to the experiences in the macroscopic world. The growth of the crystalline domains (crystallization), on the other hand, has been monitored by slower techniques, such as photographic investigations and visible or infrared imaging techniques. Photographic investigations have been performed with millisecond resolution to investigate ice nucleation events upon cooling [2] or the rate and topology of ices and hydrates formation under dynamic compression [10, 12]. Macroscopic observations of phase transitions, such as the growth of the stable nuclei into crystalline domains, require milliseconds or longer time resolution, since account for processes occurring at surfaces and limited in time by thermal contact with the environment. For example, an experimental evidence is reported for acoustically levitated water droplets [1], where the crystallization takes around 34 ms at -24°C. Moreover, aggregates of thousands of molecules are required in order to make the system crystallize at macroscopic level at high supercooling degrees [59].

In this thesis, the dynamics of pure water ice samples (I_h and VI) have been investigated by combining the Temperature Jump technique, where an energetic infrared pump pulse homogeneously heats ice on a picoseconds time scale, and the time-resolved Mie scattering spectroscopy, where a continuous-wave laser probe is used for monitoring over the time the scattering variations given by the melting and the successive recrystallization [40]. Water ices dynamics is investigated from the first nanoseconds ($\sim$ 3 ns) after the melting onset up to its completion in previously unexplored time and dimensional domains, thus covering the gap between the already known sub-nanosecond time window, typical of nano-sized samples, and the millisecond one, which is the typical range of macroscopic observations of phase transitions.

2.2 Experimental method

Ice I_h and ice VI samples, kept in a thermal bath at fixed temperature (T_0) and pressure (P_0), are “instantaneously” heated by a 15 ps pulse of light at 1930 nm.

The experimental setup used for the measurement and details on sample chamber are described in paragraph 1.2.4 of chapter 1. Ice I_h at ambient pressure is held between fluorite windows in a cryostat at a static temperature T_0 ranging between 254.2 K and 272.6 K. Ice VI is in a sapphire anvil cell (see paragraph 1.3.1 in chapter 1), between sapphire anvils, at room temperature and P_0 = 1.2 GPa or 1.4 GPa. The light is absorbed by ice through excitation of a vibrational combination band of water ($\nu_1 + \nu_2$, $\nu_3 + \nu_2$), as shown in Fig.2.2.

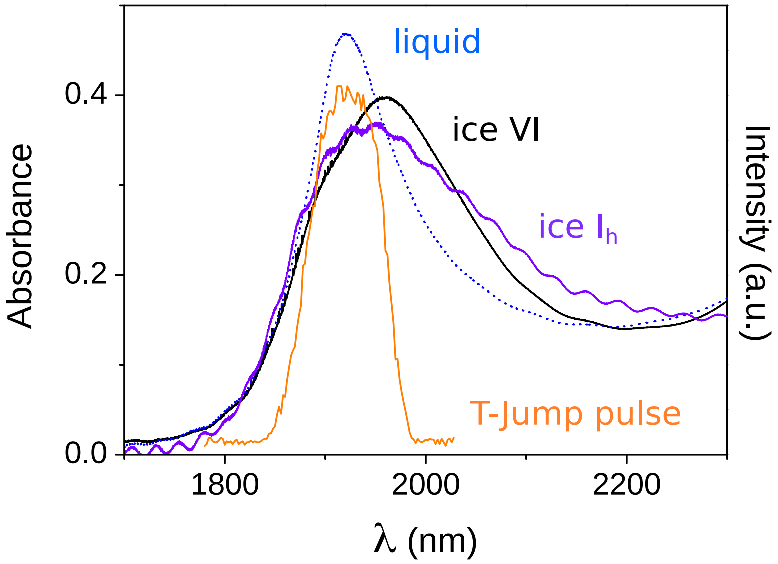

Figure 2.2: The spectra of liquid water (at room conditions), ice I_h (at 263 K), and ice VI (at 1.2 GPa) superimposed to the emission spectrum of the pump. The modulation in the ice I_h spectrum is due to interference fringes given by reflections between the anvil cell's surfaces (culet).

The employed incident energy (3-9 mJ/pulse) is well below the estimated ionization limit [58] and below the threshold of absorption saturation (see paragraph *Calculation of the saturation threshold for absorption* in chapter 1). In fact, the measured absorbance of the sample under T-Jump pulse irradiation is ~ 0.55 at all the energies used. This low absorbance value guarantees the uniformity of sample irradiation along the beam axis, and thus the sample can be uniformly heated across its length. The pump provides for a quasi-instantaneous T-Jump inside the sample up to a temperature T_1 which is dependent on the amount of delivered energy, as can be seen in Fig.2.3. This means that just after the pulse, the formation of a super-heated crystal lattice at T_1 is obtained [34]. The T-Jump is achieved through redistribution of the vibrational energy via the lattice modes (thermalization process), completed in $\sim$15 ps, while melting already starts [5, 31]. The estimated pressure change ($1.3\ \mathrm{MPa{\cdot}K^{-1}}$) [5], due to the ps T-Jump pulse, is 50 MPa during the pulse (it is about 5% of the initial pressure), and it rapidly decreases due to the melting itself in ice I_h [58].

The energy absorbed in a single pulse is $E > 2$ mJ for ice I_h and $E > 3$ mJ for ice VI, exceeding that needed to heat the sample to T_m and to obtain its complete melting (see paragraph 1.1.2 of chapter 1 for the physical values used for calculations).

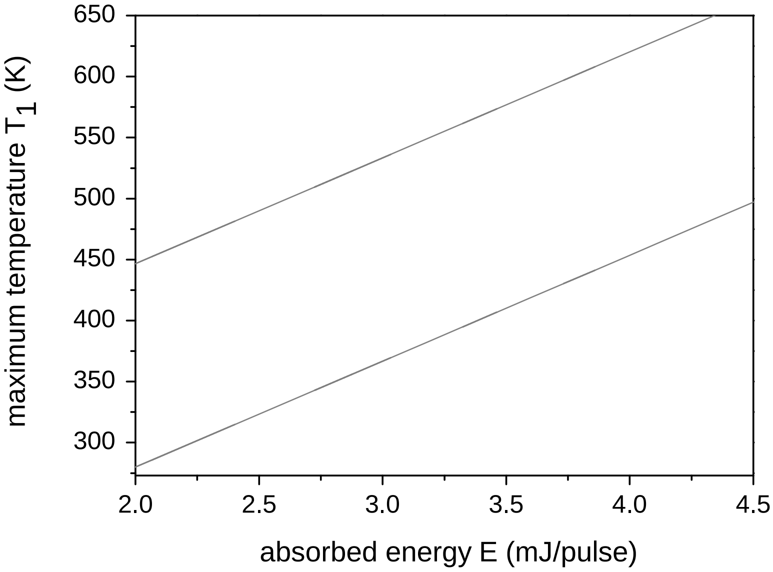

Figure 2.3: Estimate of the initial temperature T_1 just after the pulse, for an ice I_h sample at initial temperature T_0 = 263 K. T_1 values are reported as a function of the absorbed energy E. The upper and lower limits are ideal cases of no melting and complete melting, respectively, during the pulse duration.

A monochromatic continuous-wave laser beam has been used as probe in order to monitor what occurs inside the sample after the excitation. We used several probe wavelengths (λ_{probe}), as described in section 1.2.4 of chapter 1. The transmission of the probe laser through the sample has been measured with a fast Si photodiode by using the experimental setup of Fig.1.6 and the detection configuration of Fig.1.8a. The acquired transmission curve describes the time evolution of the signal (figure 2.4). In general, when a pump pulse is shot, the probe transmission drops to a minimum in tens of nanoseconds (depending on the amount of deposited energy) and then returns to a static value in a time (from micro- to milliseconds) strongly dependent on T_0. That static value is the same observed for the (polycrystalline) sample before the excitation, meaning that a polycrystalline sample of the same optical properties is reformed.

The transmission of the probe through liquid samples does not change after the T-Jump pulse, even though liquid water absorbs the pump beam to the same extent as ice (Fig.2.2), except at the highest E values ($E \geq 4.5$ mJ), where a strong oscillation of the transmission is observed, likely due to the formation of vapor bubbles. The transmission of the liquid remains $\sim$ 5–10% higher than the static ice transmission, explainable in terms of optical quality, being the ice sample polycrystalline and not a single crystal. Only a weak transmission decrease is observed, likely due to thermal lensing effect, as can be seen in Fig.2.5,

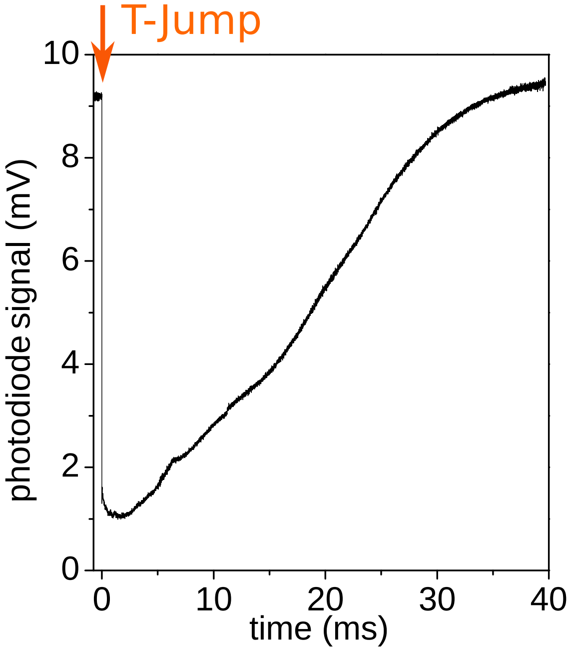

Figure 2.4: Kinetic trace detected by the photodiode and recorded by the oscilloscope. The photodiode signal is acquired with E = 3.5 mJ at T_0 = 269 K and λ_{probe} = 632.8 nm. Before the T-Jump pulse, the static transmission typical of the unperturbed polycrystalline ice I_h sample can be observed. After the pulse a fast loss of transmission is observed followed by a slow recovery of the initial transmission value.

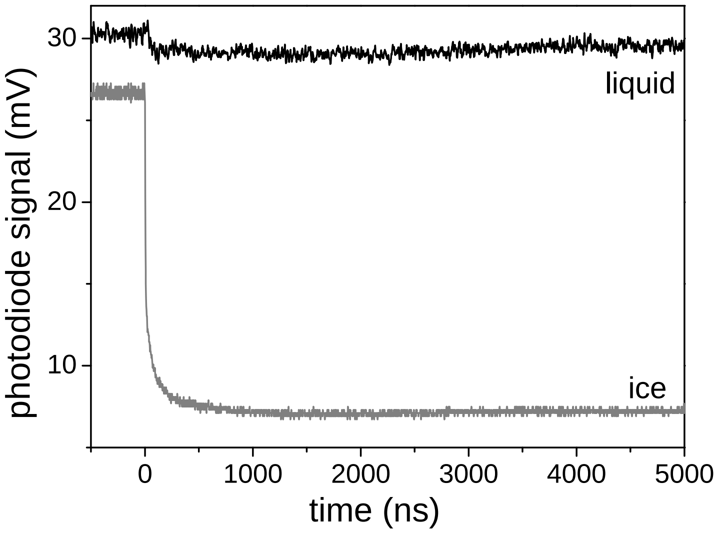

Figure 2.5: Comparison between the transmission curves for a liquid water sample and an ice sample. Both samples have been irradiated with E = 3.5 mJ and probed with the same λ_{probe} = 457.9 nm. In ice at T_0 = 263 K, the T-Jump causes a drop in transmission. In liquid water at T_0 = 278 K only a weak transmission decrease, ascribed to thermal lensing, is observed.

where the comparison between the transmission curves in a liquid water sample and in an ice sample after the T-Jump with the same absorbed energy (E = 3.5 mJ) and probed with the same λ_{probe} is shown. The negligible transmission decrease in the liquid confirms that the signal observed in ice is not affected by unwanted contributions, such as interferences between pump and probe light on the photodiode. Thermoreflectance [60, 61] has also been considered to potentially contribute to our signal, but the absence of highly reflecting interfaces suggest to rule out this contribution.

2.2.1 Interpretation of the signal

The transmission change in the kinetic trace is due to the scattering at interfaces between (super-heated) ice and molten ice domains, generated by the T-Jump and evolving in time. This has been confirmed by changing the detection configuration: when the transmitted beam is blocked (Fig.1.8b) a positive signal due to off-axis scattered light is consistently observed, with a time dependence similar to the transmission change (see trace of Fig.2.6).

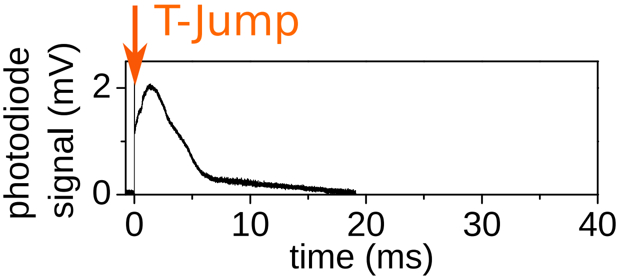

Figure 2.6: The transmission curve has been acquired with blocked probe beam as in the configuration of figure 1.8b. The time-dependent signal has been measured in ice I_h at T_0 = 269 K with energy absorbed by the sample E = 3.5 mJ, and λ_{probe} = 632.8 nm. The positive signal is due to the off-axis scattered light.

As expected for scattering, the signal amplitude increases as λ_{probe} decreases in both configurations. The independence of the transmittance on the probe power has been always verified. After each pump pulse, it is possible to observe by eye a different speckle produced by the static scattering of the probe beam by the sample, consistent with a melting and refreezing event.

To summarize, the absorption of the T-Jump pulse induces a fast super-heating of the ice sample which evolves in the melting of part of the sample followed by the sample refreezing caused by the temperature decrease from T to T_0, due to the thermal contact with the environment.

The estimation of the size of the molten domains evolving after the pulse and determining the light scattering is the goal of this approach. Several fresh samples have been studied in order to check the reproducibility of the measurement. Each sample has been used for many shots, and each shot probes a single melting/crystallization event in a polycrystalline sample with slightly different optical quality. The evolution has been monitored until the complete recovery of the sample's initial conditions (hundreds of milliseconds depending on T_0), and the measurements have been repeated at temporal intervals larger than 2 seconds, allowing for the complete sample recrystallization. The complete melting, indicated by a transmission increase to the liquid transmission value, has been rarely observed despite the excess of energy delivered to achieve the process. The liquid transmission value, in fact, has been observed only by using the maximum energy value and T_0 very close to T_m in the range 270–273 K (or piling up T-Jump pulses with a 1- to 5-Hz rate).

2.3 Analysis of the transmission curve

2.3.1 Considerations on thermal conduction and melting rate

Due to the T-Jump, the sample temperature increases to T_1, which depends on the amount of absorbed energy E (as can be seen in Fig.2.3), leading to a super-heated state. Due to the incessant thermal contact with the external environment, the temperature T(t) decreases after the pulse, until it reaches the initial value T_0. The melting process occurs at quasi-constant temperature T_1, while the thermal conduction through the sample's walls and the sample itself occurs in a longer time scale. The magnitude of these two time scales respectively depends on the amount of absorbed energy E, which determines T_1, and on the external temperature T_0. In particular, T_1 affects both the rate of thermal diffusion ($\propto T(t) - T_0$) and the rate of melting, which is expected to be kinetically driven by the super-heating, having a rate $\propto e^{T(t)-T_m}$.

2.3.2 Results

The acquired transmission curves have been transformed into absorbance A(t) (Fig.2.7) by using the following equation

$$A(t) = -\log \frac{I(t)}{I_s} \tag{2.1}$$

where I(t) is the transmission curve (photodiode signal intensity evolving in time) and I_s, which is used as reference, is the initial, static transmission of the polycrystalline sample before the pump pulse.

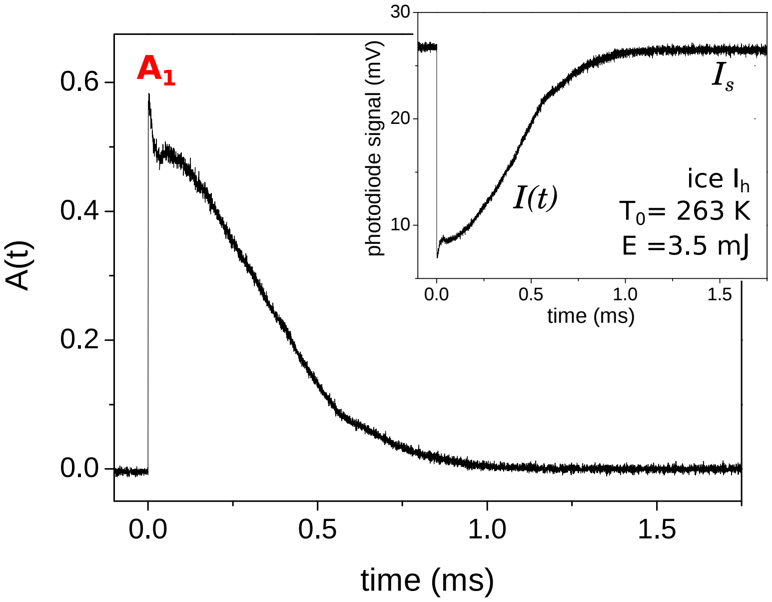

Figure 2.7: The transmission curve $I(t)$ is transformed into an absorbance curve using the initial static transmission I_s as reference.

The absorbance curves have been accurately fitted by the following monoexponential growth function

$$A(t) = A_1(1 - e^{-\frac{t}{\tau_1}}) \tag{2.2}$$

in the region up to 1000 ns (Fig.2.8). The time constant τ_1 and absorbance A_1 values, resulting from the analysis of the acquired experimental curves, are reported in Fig. 2.9 as a function of the used absorbed energy E. The rate constant τ_1 is the characteristic time of the monoexponential growth which is able to fit the absorbance curve in the first region after the T-Jump pulse up to 1000 ns. The τ_1 values are the same for ice I_h and ice VI within the error. As can be seen in the figure, the monoexponential time constant τ_1 spans five orders of magnitude from 15000 to 5 ns, decreasing exponentially with E, as expected since it represents the

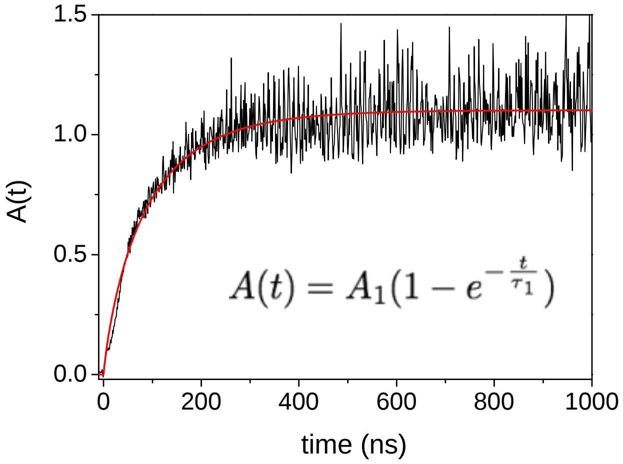

Figure 2.8: An example of the monoexponential fit up to the first maximum A_1 is shown for ice I_h at T_0 = 269 K with E = 4.9 mJ/pulse and λ_{probe} = 632.8 nm.

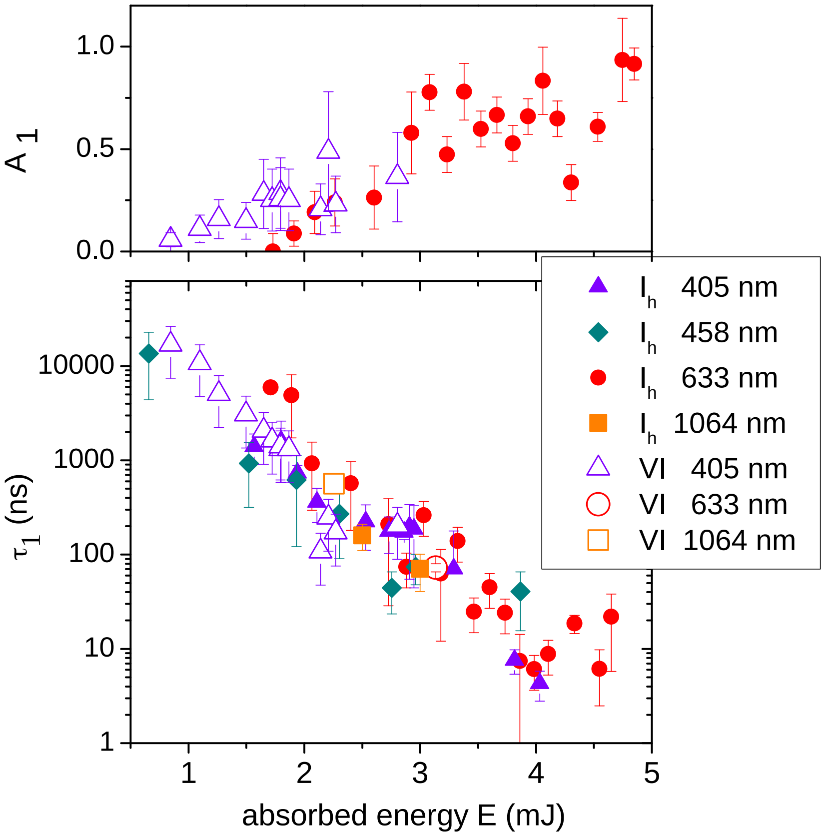

Figure 2.9: Time constant τ_1 and absorbance A_1 average values resulting from the fit both for ice I_h and ice VI. The error bars represent the standard deviations. The values are averaged over a number of pulses ≥ 10, and for ice I_h different T_0 conditions (within the range 254.2–272.6 K) have been considered for the fitting. Results for different λ_{probe} are reported.

characteristic time of melting growth, driven by the super-heating of the crystal. In fact, by changing the used E, different curves can be observed (Fig. 2.10): The first maximum in the A(t) curve appears for $E \geq 2.5$ mJ as a sharp peak followed by a fast decrease. For $E \geq 3.5$ mJ, instead, a second maximum at longer time scales can be observed.

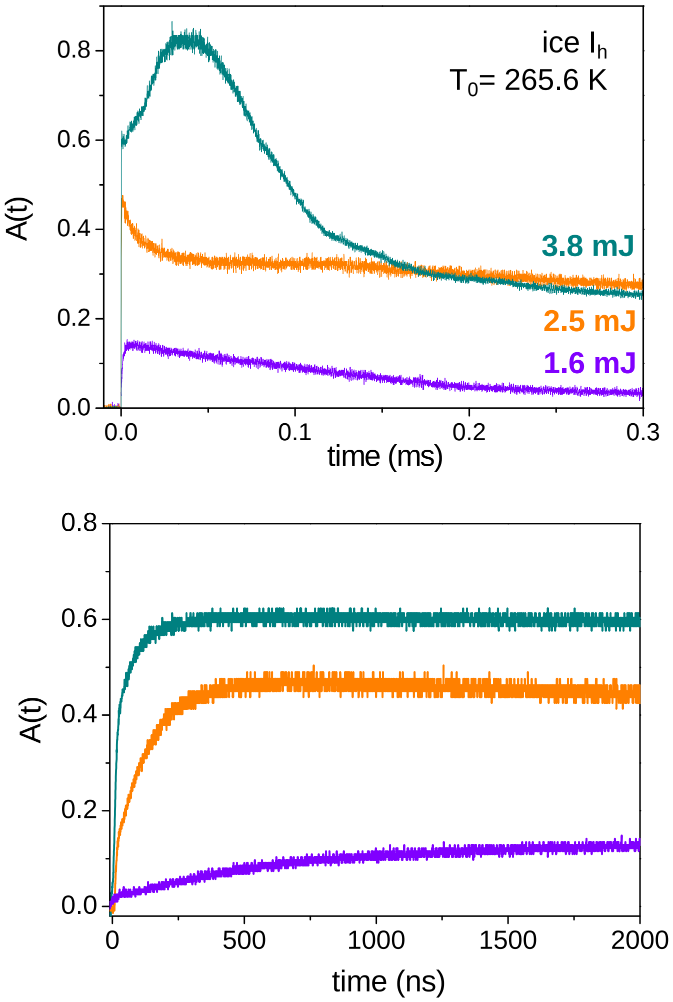

Figure 2.10: Absorbance curves obtained using different pump energies. (Lower) Zoom-in of the same curves in the range 0-2 μs.

The temporal range where the used exponential function well reproduces the curve depends on both E and T_0, being the result of two competitive phenomena, the melting at $T \sim T_1$ and the thermal conduction, which reduces the super-heating and, thus, the melting rate. We have also verified if there is a dependence of τ_1 and A_1 on T_0 i.e. if the initial temperature affects the fast melting dynamics. Many measurements have been performed as a function of T_0 (in the range 254.2-272.6 K) for ice I_h, revealing that τ_1 and A_1 are independent of T_0 if the pump pulse energy values are greater than 2.5 mJ (E $\geq$ 2.5 mJ/pulse), and confirming that the thermal conduction is not relevant in the firsts 600 ns within the probed T_0 range. For energy E $\geq$ 2.5 mJ, where $\tau_1 \leq$ 600 ns (Fig.2.9), we experimentally find for ice I_h that τ_1 is independent of T_0, for fixed energy values. This finding is shown in Fig.2.11 (lower).

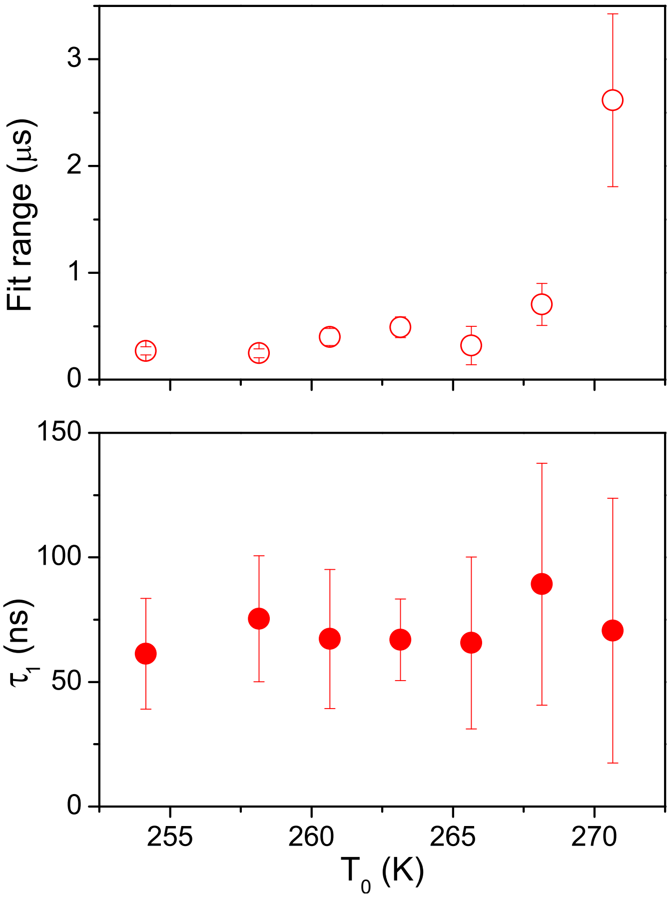

Figure 2.11: Dependence of τ_1 on T_0. The rate constant τ_1 values obtained from the monoexponential fit (Lower), in the time range specified (Upper), of absorbance curves acquired on ice I_h for the specific case E = 3 mJ and λ_{probe} = 632.8 nm as a function of the external temperature T_0. The values are averaged over several pulses in the same T_0, and λ_{probe} conditions. The error bars represent the resulting standard deviations ($\pm\sigma$).

The time range where the monoexponential fit is able to reproduce the curve depends inversely on $T - T_0$, as can be deduced by the Fig.2.11 (upper), and can be seen as a time range where the thermal conduction is not yet effective as the behavior can be described by a single exponential phenomenon. This result means that the thermal conduction occurs on longer timescales and does not affect the melting dynamics in the first hundreds of nanoseconds.

2.4 Size evolution of molten domains

2.4.1 Mie scattering theory

The scattering of light can be thought as the change of the direction of light taking place when an incident light beam encounters an obstacle, that is the scattering particle.

Light scattering theory can be categorized in terms of two theoretical frameworks. One is the *Rayleigh* scattering theory which is applicable to small, non-absorbing, spherical particles. Rayleigh scattering describes the elastic scattering of light by spheres that are much smaller than the wavelength of light, and its model breaks down when the particle size becomes larger than around 10% of the wavelength of the incident radiation. The second is the theory of *Mie* scattering which includes the general spherical scattering solution (absorbing or non-absorbing) without a particular extent on particle size. Mie scattering theory has no size limitations, but suggests situations where the size of the scattering particles is comparable to the wavelength of the light, rather than much smaller or much larger. Mie theory, therefore, can be considered as a general theory used to describe most spherical particle scattering systems, including Rayleigh scattering. For the special case of spherical particles, Mie theory is the basic theoretical tool. In fact, it provides for the solution for the electromagnetic scattering by a sphere of radius R in a homogeneous and isotropic medium illuminated by a plane wave. One can distinguish two main approaches to this problem: One adapts the properties of the object in order to obtain scattered radiation with the desired properties, the other one studies the characteristics of the scattered radiation to deduce properties of the object which is illuminated. This approach is known as *The Inverse Problem* (and it has been applied in this work in order to obtain the size of the scatterers of our system).

Suppose that one or more particles are placed in a beam of electromagnetic radiation. The rate at which the electromagnetic energy is received by a detector placed downstream from the particles is denoted by U. If the particles are removed, the power received by the detector is U_0, where $\mathrm{U}_0 > \mathrm{U}$. The presence of the particles has resulted in *extinction* of the incident beam. If the medium where the particles are embedded is non-absorbing, the difference $U_0 - U$ is due to *absorption* in the particles and/or *scattering* by the particles. This extinction depends on the chemical composition of the particles, their size, shape, orientation, the surrounding medium, the number of particles, and the polarization state and frequency of the incident beam. Let us now consider extinction by a single particle embedded in a non-absorbing medium and illuminated by a plane wave. We construct an imaginary sphere of radius r around the particle (of radius R). One of the most important physical quantities involved in the extinction phenomenon is the *cross section*, defined as the net rate at which electromagnetic energy (W) crosses the surface of an imaginary sphere of radius r $\geq$ R centered on the particle divided by the incident irradiance (I_i) [62]. To quantify the rate of the electromagnetic energy that is absorbed (W_{abs}) or scattered (W_{sca}) by the diffuser, the absorption (C_{abs}) or scattering cross sections (C_{sca}) can be defined:

$$C_{abs} = \frac{W_{abs}}{I_i}; \quad C_{sca} = \frac{W_{sca}}{I_i} \tag{2.3}$$

The sum of these is the extinction cross section $C_{ext} = C_{sca} + C_{abs}$, which gives an idea of the amount of energy removed from the incident field (beam) due to scattering and/or absorption generated by the particle.

Let us consider a collection of spherical particles homogeneous in sizes D and refractive index n. All the information about scattering by any particle or a collection of particles is contained in all the elements of the 4×4 scattering matrix. Each of its 16 elements is an angle-dependent function of wavelength, particle size, shape, and composition. The *differential scattering cross-section* is defined as the energy scattered per unit time into a unit solid angle about a direction Ω, specified by two angles, the scattering and the azimuthal angles, for unit incident irradiance. Despite scattering being a mechanism for polarizing light, unpolarized light has been taken for our calculations, and for unpolarized incident light, the equation for the differential scattering cross-section is

$$\frac{dC_{sca}}{d\Omega} = \frac{S_{11}}{k^2} \tag{2.4}$$

with

$$k = \omega\sqrt{\varepsilon\mu} \tag{2.5}$$

where ω is the frequency of the radiation, ε is the permittivity, μ is the magnetic permeability of the medium, and, given unpolarized incident light, S_{11} is the element of the scattering matrix which is the dimensionless scattered irradiance, and specifies the angular distribution of the scattered light. The angular distribution of the scattered light is a property of the single particle and does not depend on the concentration of the suspension where the particles are embedded. In fact, it strongly depends on the size of the particles diameter D, as is reported in Fig.2.12 showing the scattering cross-section as a function of azimuthal angle (θ).

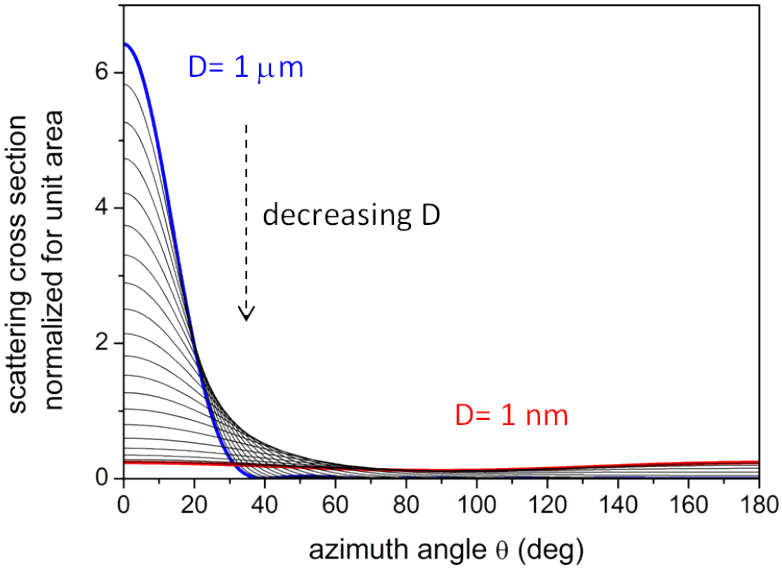

Figure 2.12: The scattering cross-section as a function of azimuthal angle (θ) is shown. For a given wavelength it decreases as the diameter (D) of the scatterer decreases, as can be seen in the two extreme cases of D = 1 μm (blue line) and D = 1 nm (red line).

The scattering by a single particle is independent of the concentration of the particles in the suspension. For a given homogeneous (with the same size D of particles) monodisperse suspension, the ratio of the scattering measured at two different angles is independent of the concentration. In this way, it is possible to obtain a value for D independently of the concentration.

In the following, the expected absorbance (A) of each suspension has been calculated as

$$A = C_{sca} \times C \times h \tag{2.6}$$

where C is the particle's concentration, h is the sample thickness, and C_{sca} is the Mie scattering cross-section. The scattering cross-section, according to the Mie theory, is computed by using a FORTRAN source code, which is reported by Bohren and Huffman for a spherical scatterer [62]. The absorbance A in our case is only due to the scattering by the particles as the absorption is zero for a non-absorbing suspension. In the assumption of homogeneous suspension of same-diameter D spherical particles transparent to the probe wavelength, the code input for the calculation of the C_{sca} contains the wavelength of the probe light (λ_{probe}), the refractive indexes of the particles and surrounding medium, the diameter (D) of the particles, and the range of azimuthal angles (θ) with respect to the forward direction at which the light is collected (Fig.1.8 a and b). The output contains the matrix elements of the scattering cross-section for the single particles, from which the angular distribution of scattered light for unpolarized light can be calculated.

The values of the refractive indexes used in the calculations of liquid water (scattering particles) and of ice I_h (surrounding medium) are n_{ice} = 1.308 (ice lattice) and n_{liq} = 1.332 (liquid water spheres). For the calibration, the refractive index for SiO_2 nanoparticles (scattering particles) is n = 1.430.

2.4.2 Characterization of the setup sensitivity

In order to assess the sensitivity of the used experimental setup to the method based on Mie scattering, the transmission through monodisperse suspensions of SiO_2 nanoparticles in water has been measured with the configuration of Fig. 1.8a and the T-Jump off.

Several diameters (D = 20, 80, 200, and 400 nm) of SiO_2 nanoparticles and different particles concentrations (C) have been used for the measurement. Moreover, quartz cuvettes with optical path of 0.1 or 10 mm have been employed. The transmission loss due to scattering (reported as absorbance) measured for suspensions of particles characterized by different diameters D and concentrations C is reported in Fig.2.13 (the used thickness is 10 mm). The absorbance has been calculated by using as reference the cuvette containing pure water. The lines represent the values calculated according to the Mie-scattering theory. As can be seen in Fig.2.13, the absorbance values measured with the calibration suspensions are in excellent agreement with the calculated by the Mie-scattering theory. In Fig.2.14 the absorbance values measured as a function of different λ_{probe} on suspensions of particles having D = 200 nm (C = 1.1 μm^{-3}) and D = 400 nm (C = 0.14 μm^{-3}) are reported for an optical path of 0.1 mm (which is double our samples). As can be seen, if $C \geq 1\ \mu m^{-3}$ and $\lambda_{probe} \leq 632.8$ nm, our setup, and thus the used probe method, is sensitive to particles sizes down to 200 nm.

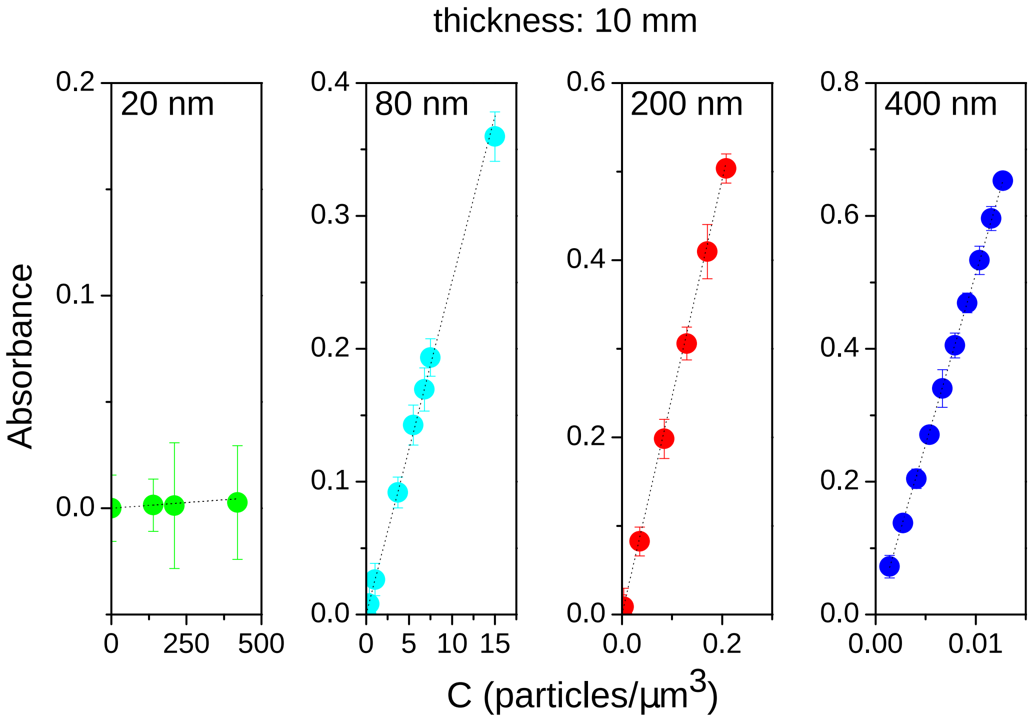

Figure 2.13: Result of the calibration of our setup to the method based on Mie scattering, obtained by using monodisperse suspensions of silica nanoparticles in water. The calibration on an optical path of 10 mm as a function of concentration for different particle diameters (20, 80, 200, and 400 nm), and λ_{probe} = 632.8 nm, is reported. The lines are the calculated values.

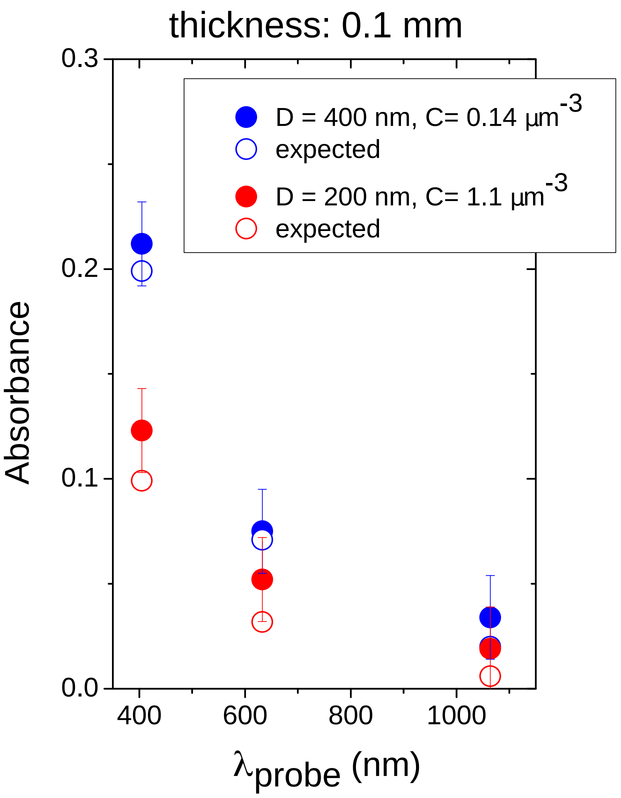

Figure 2.14: Result of the calibration of our setup to the method based on Mie scattering, obtained by using monodisperse suspensions of silica nanoparticles in water. The calibration on an optical path of 0.1 mm as a function of the λ_{probe} used is reported for different particle diameters (200 and 400 nm). The calculated (expected) values are reported in the figure as open circles.

2.4.3 Determination of the molten domains size

The angular distribution of the scattered light is a property of the single particle. It does not depend on the concentration, and it strongly depends on the dimension of the scatterer, as is reported in Fig.2.12. For this reason it can be used to estimate the diameter D for a homogeneous monodisperse suspension of spherical particles.

Due to the limitation of our experimental setup, it is not possible to characterize the entire scattering efficiencies as a function of θ. To give an estimation of the scatterer's dimension, the ratio between the scattering intensities integrated between different angles have been measured. The two configurations of Fig.1.8 have been used to detect the attenuation of the transmitted beam, that is a measure of the total scattering ($Total\ Sca$, between 0 and 180°), with the configuration (a), and the scattering intensity at $2^\circ < \theta < 7^\circ$ ($2-7^\circ\ Sca$), with the configuration (b).

The signal in both configurations of Fig.1.8 with the pump off has been acquired for a suspension of silica nanoparticles having diameter D = 400 nm, concentration C = 0.01273 μm^{-3}, with λ_{probe} = 632.8 nm and a sample thickness h = 10 mm. As explained above, the ratio of the two acquired signals $\left(\frac{2-7^\circ\ Sca}{Total\ Sca}\right)$ is due to the angular distribution of the scattered light, and yields an estimate of the scatterer's diameter, which is D = 409 nm in our case. This result indicates that we are able to correctly estimate D for a monodisperse suspension by using the ratio of the signals obtained by the two configurations.

In order to determine the size of the scatterers in our sample after the excitation, the method described above has been used for ice I$_h$. The transmission curves as a function of time for ice I$_h$ at T_0 = 269 K have been acquired after the T-Jump pulse (E = 3.5 mJ) by using the two configurations of Fig.1.8 with λ_{probe} = 632.8 nm. Their ratio $\left(\frac{2-7^\circ\ Sca}{Total\ Sca}\right)$ as a function of time can be seen in Fig.2.15A. In the approximation where all of the scattering domains are spheres with the same diameter D, by comparing the curves of Figs.2.15 A and B, respectively showing the ratio of the experimental signals $\left(\frac{2-7^\circ\ Sca}{Total\ Sca}\right.$, that is $\left.\frac{b}{a}\right)$) and the ratio of the signals calculated as a function of D for the same azimuthal angles as in the experimental configurations (according to the angular distribution of the scattered light), an estimate of D is obtained as a function of time. This diameter monotonically increases up to $\sim$ 1.5 μm in 2.3 ms and then decreases for longer delays (Fig. 2.15 C).

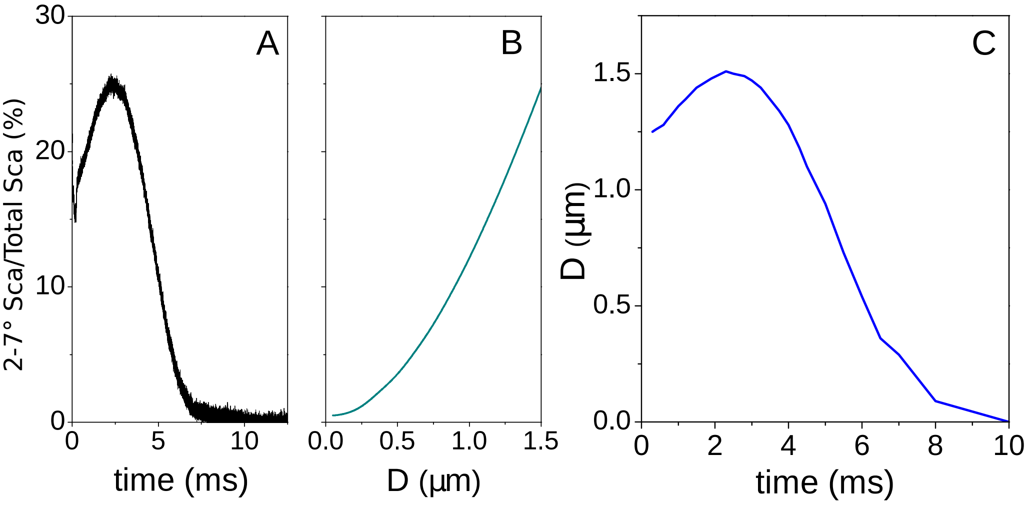

Figure 2.15: Determination of the scatterer's diameter D(t) in our samples by the angular distribution of scattering, in the approximation of a monodisperse suspension of spherical particles. (A) The ratio of the signals measured as a function of time in the two configurations of Fig.1.8(b/a), 2-7°Sca/Total Sca. (B) The ratio of the signals calculated as a function of D for the same azimuthal angles as in the experimental configurations. (C) D(t) in our samples obtained by discretely sampling and comparing the curves in A and B.

The spherical scatterers in the sample can be thus identified as molten domains growing and evolving so long as the temperature is higher than the melting temperature ($T > T_m$), and decreasing in size during refreezing, i.e. when $T = T_m$. The configuration of Fig.1.8b is affected by a strong reflection of the pump beam, allowing for the estimate of the dimensions only for $t \geq 0.3$ ms. In addition, the method makes use of data from two different pulses, meaning two different ice samples, and of a weak off-axis scattering signal.

2.4.4 Model of the melting and refreezing sample

The simplest model to describe our sample and its evolution after excitation assumes as starting point the sample at $\sim$ 3 ns after the T-Jump, which is the minimum delay experimentally accessed by the detector. At $\sim$ 3 ns nucleated monodisperse suspension of water spheres randomly positioned in an ice matrix at homogenous temperature T_1, with initial diameter D_1 and concentration C_1 are already present. As estimated in previous works and calculated according to Fig.2.3, T_1 can be set to 360 K, and D_1 = 25 nm [5, 31]. C_1 is set to a different value for each simulation, ranging between 0.1 and 5 μm^{-3}. In the simulation (see paragraph *Simulation details*) the temperature at the sample's wall T has been imposed to decrease in time with an exponential law to the final value T_0. The water spheres are set to grow, at each time step, by the same amount, depending on $T - T_m$, and coalesce when they touch each other. When $T < T_m$, the water spheres decrease instead of growing. At all time steps, the absorbance is calculated on a monodisperse suspension where all of the spheres have the same average diameter. The rate constants for the temperature decrease, spheres growth, and spheres decrease have been chosen to reproduce the shape of the curve obtained experimentally. The simulation does not provide any indication on the actual time scales of the processes, which are derived only by the experiment, but it is essential to validate the approximations made. In fact, despite the model simplicity and the quite small dimensions of the used simulation box ($10\times10\times10$ μm^3), the simulation is able to reproduce with great detail the features of the data, as can be seen by comparing figures 2.10 and 2.16.

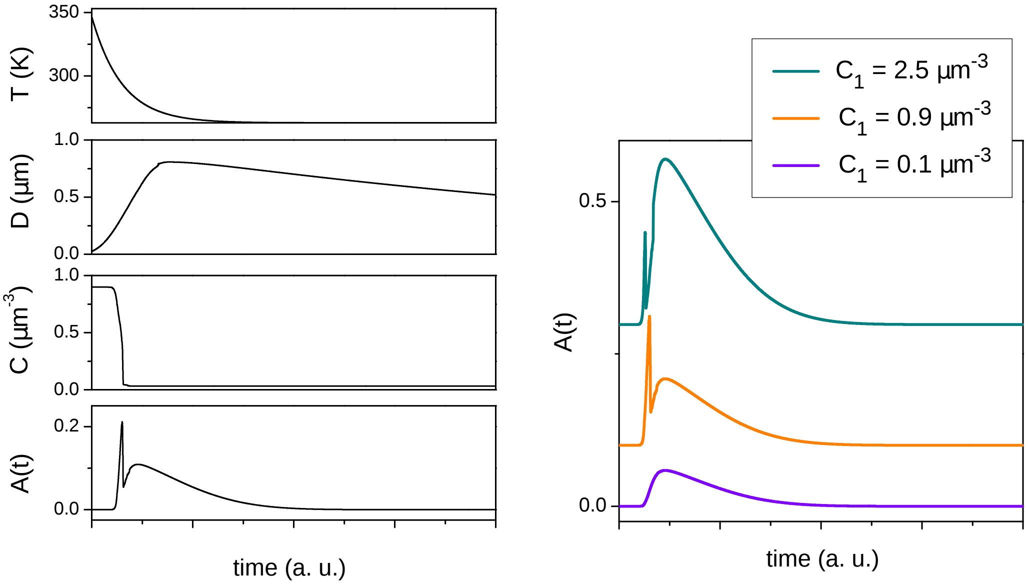

Figure 2.16: Results of the simulation. (Left) Time evolution, for an initial concentration $C_1 = 0.9\ \mu m^{-3}$, of the temperature T(t), the average diameter D(t), and the concentration C(t) of the droplets and of the resulting absorbance A(t). In the A(t) curve obtained by the simulation, the first sharp maximum (A_1) and the following decrease are due to coalescence, and the second maximum is due to the formation of larger domains. (Right) A(t) curves simulated with different C_1 values. Increasing C_1, the simulation reproduces the effect experimentally observed by increasing the energy E (Fig.2.10), suggesting that E determines the initial concentration of melting nuclei.

In particular, the changes in the A(t) curves simulated with increasing C_1 perfectly reproduces what is experimentally observed by increasing the absorbed energy E (Figs.2.10 and 2.16 on the right). The absorbance curve A(t) in the figures has a sharp maximum (A_1) resulting from the coalescence, where a critical diameter is reached and the water spheres merge into each other. By further increasing of C_1 (see Figs.2.10 and 2.16 on the right) a second maximum due to large spheres formation appears. As expected, this behavior confirms that E, by determining the number of excited molecules, is responsible for the concentration of the melting nuclei at $\sim$ 3 ns. The saturation of A_1 with the energy E (Fig.2.9) likely indicates a limit temperature of super-heating, previously estimated as $\sim$ 360 K, above which the number of melting nuclei becomes independent of the temperature T of the sample.

The model allows us to constrain the scatterers' concentration C and obtain an estimate for their diameter D, in the approximation of the sample as a monodisperse suspension of water spheres in ice (Fig.2.17).

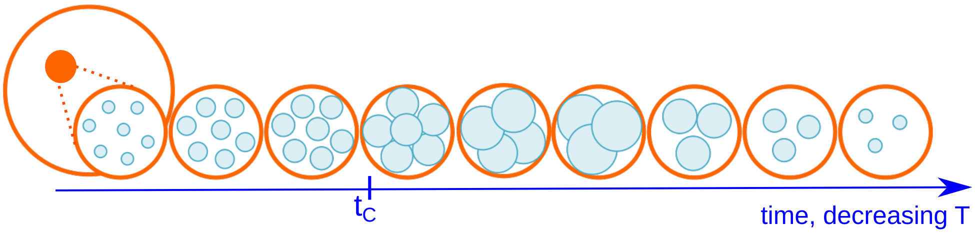

Figure 2.17: A cartoon of the proposed model for the evolution of the super-heated ice/water system during melting and refreezing is reported. Liquid domains, approximated as spheres, grow at constant concentration C_1 (the initial number of spheres) until coalescence occurs (at t_C). After the coalescence period (where C and D are bound by a packing constraint), when T = 273 K, the domains start decreasing in volume at fixed concentration C_2.

In fact, the simulation assumes C is approximately constant before the coalescence, occurring at a time t_C where the sharp maximum is observed. A certain value of absorbance for the suspension can be given by infinite couples of C and D values, but many of those have no physical meaning. For this reason geometrical constraints have to be applied to our system during coalescence (for $t \geq t_C$). For example, C and D can be linked by the simple cubic packing constraint (or other packings), whose equation is reported below.

$$C = \frac{1}{D^3} \tag{2.7}$$

As the A(t) curves measured with E = 3.5 mJ are concerned, the values of diameter and concentration (D = 430 ± 15 nm and C = 13 μm^{-3}) at $t_C \sim 200$ ns have been obtained with very good agreement with the different λ_{probe} used. Moreover, by imposing a constant concentration at $C(t) = C(t_C)$ for $0 < t < t_C$, D(t) can be deduced at t < 200 ns, as explained in the following. The τ_1 and A_1 values resulting from the exponential fit (Fig. 2.9) of the curves measured at E = 3.5 mJ (at every T_0) have been averaged and used to build the exponential growth shown in panel A of Fig. 2.18. For each λ_{probe}, C has been determined by using simple cubic packing at t_C = 200 ns, where the absorbance is A_1. This C value has been used to calculate the absorbance expected in the detection configuration of Fig.1.8a (transmitted beam), as a function of drops diameter, A(D). The reverse D(A) function has been fitted to a stretched exponential (panel B of Fig. 2.18). The absorbance variable in the stretched exponential function has been substituted with the exponential growth of A to obtain the D(t) curve (Fig. 2.18 C), for different λ_{probe}.

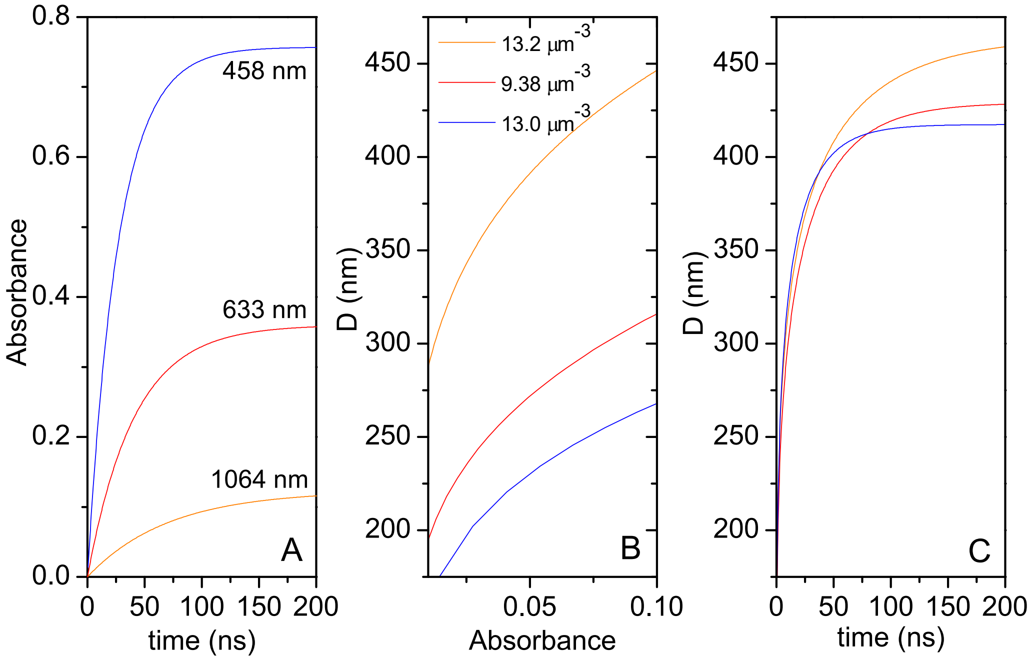

Figure 2.18: Characterization of the sample's evolution at t < 200 ns after the T-Jump. (A) Absorbance curves as a function of time built using τ_1 and A_1 values resulting from the exponential fit (Fig.2.9). (B) D(A) curves, for each λ_{probe}. D(A) curve is the reverse function of the expected absorbance as a function of the diameter. (C) The resulting D(t) curve, for different λ_{probe}.

As shown in the inset of Fig. 2.19, the melt domains grow slowly in time, from ∼ 200 nm to ∼ 400 nm in ∼ 200 ns. In the graphs of figure 2.19, the system's evolution is reconstructed from 3 ns after T-Jump until the recrystallization. The refreezing starts when the temperature of the sample's wall, in contact with the environment, reaches T_m = 273 K. During freezing, the heat is constantly removed by the thermal bath, whereas the sample remains at T_m. Thus, the freezing rate should be dependent on the rate of heat diffusion through the ice/water system

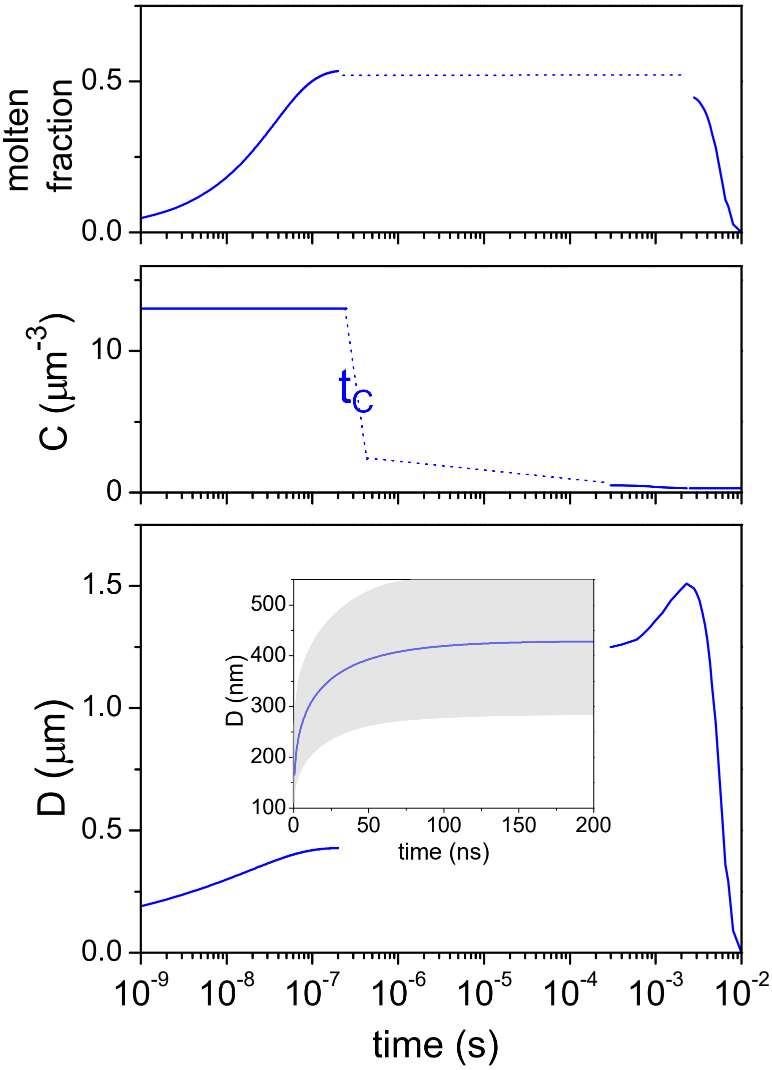

Figure 2.19: System's evolution (molten fraction, C and D as a function of time) from 3 ns after T-Jump until the recrystallization, obtained for E = 3.5 mJ, T_0 = 269 K, and in the approximation of simple cubic packing during coalescence. (Inset) Diameter of the scattering domains for t < 200 ns at the same E and T_0 conditions. Blue line for simple cubic packing; the shaded area contains values obtained by different packing hypothesis.

to the cell walls, proportional to T_m - T_0. In order to investigate the refreezing rate, A(t) curves obtained for ice I_h with E = 2.5 mJ and λ_{probe} = 632.8 nm, in a series of measurements at different T_0 conditions, have been analyzed. The decreasing part of the A(t) curves has been fitted by an exponential decay. To relate this decay to the sample's state, an averaged diameter D(t) of the molten domains, decreasing with time, has been estimated by assuming C constant, in this temporal range, at a value C_2. This value is obtained by imposing the packing constraint

$$C_2 = \frac{1}{{D_2}^3} \tag{2.8}$$

where D_2 is the maximum diameter of the water spheres (1500 nm) obtained by the analysis of the angular distribution (Fig.2.15). The resulting V(t) curves are well fitted by an exponential decay, where

$$V(t) = \frac{\pi \cdot D(t)^3}{6} \tag{2.9}$$

As expected, the rate constant $\frac{1}{\tau}$ increases linearly with ΔT = T_0 - T_m (Fig.2.20).

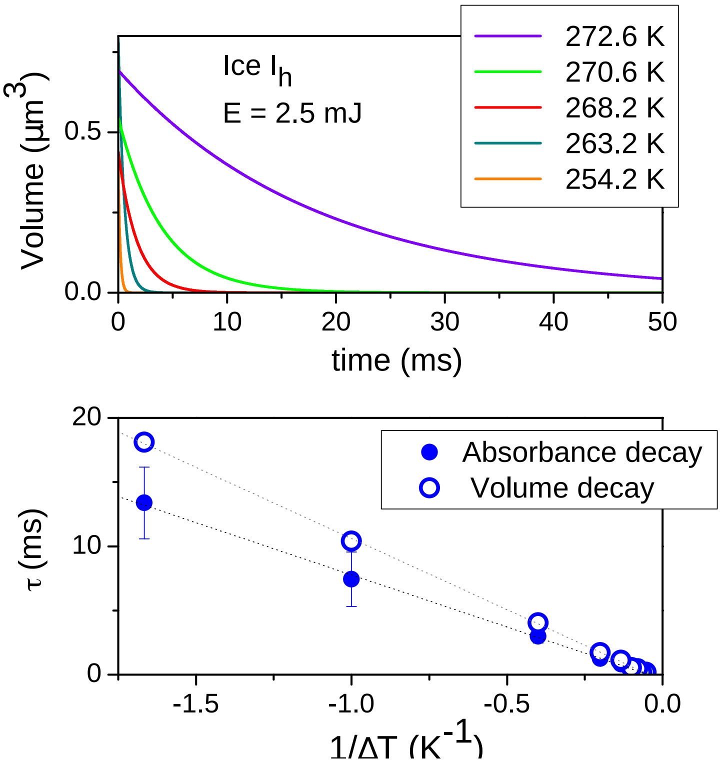

Figure 2.20: (Upper) The volume of the scattering domains as a function of time during refreezing, for ice I_h at different T_0 temperatures of the thermal bath, obtained as described in the text and reproduced as exponential decays. (Lower) The time constant of these exponential decays depends linearly on $\frac{1}{\Delta T}$ ($\Delta T = T_0 - T_m$).

Simulation details

The model describes the sample after the T-Jump, at delays accessible to our experimental observation (t $\geq$ 3 ns). The sample is a $10\times10\times10$ μm^3 monodisperse suspension of water spheres, randomly positioned, in an ice matrix at homogeneous temperature. The initial conditions are reported:

- Initial temperature: $T_1 \sim 360$ K (different initial temperatures have been used in the range 350-400 K).
- Initial diameter of all drops: D_1 = 25 nm [5, 31].
- Initial concentration: C_1 is set at a different value for each simulation (C_1 = 0.1-5 μm^{-3} is able to reproduce our experimental curves at all the absorbed energies E).

In the following, the constants a, b, and c have been chosen to reproduce the shape of the experimental curves. Simulations with different C_1 values are performed with fixed a, b, and c. The following can be assumed at each time step (j) during the simulation:

- The temperature of the sample's wall decreases exponentially in time from T_1 to T_0

  $$T_j = T_1 e^{-aj} + T_0 \tag{2.10}$$

  where T_m = 273 K, T_0 = 263 K.

- If $T_j > T_m$, the volume V of the drops increases all by the same amount:

  $$V_j = V_{j-1}(1 + bT_j) \tag{2.11}$$

  The linear dependence on T does not imply any assumption on the melting mechanism (kinetically or thermodynamically driven by the super-heating). The choice of b is, in fact, arbitrary, as is the length of the time steps.

- If two drops get in contact, they become one drop with spherical shape, with volume equal to the sum of the original volumes, and positioned in the previous center of mass (coalescence).

- If $T_j \leq T_m$, the volume V of the surviving drops decreases all by the same amount

  $$V_j = V_{j-1}(1 + cT_j) \tag{2.12}$$

The temperature T_j is, in fact, the temperature at the interface between the sample and the environment. During refreezing the sample is at T_m, and the small difference $|T_j - T_m|$ (Fig.2.16, left) is the driving force for refreezing.

- The average diameter of the drops D is calculated.
- The absorbance in the configuration of Fig.1.8a is calculated for a monodisperse suspension of spherical droplets with diameter D(t) and concentration C(t), for a thickness of 10 μm and λ_{probe} = 632.8 nm.

As a result of growth and coalescence, the concentration is approximately constant up to a critical time where it suddenly decreases due to coalescence. Correspondingly, the A(t) curve has a sharp decrease in absorbance after the maximum (A_1). This result has been used to obtain the size evolution of molten domains.

2.5 Other investigations

The method described in this chapter has also been applied to the investigation of the melting dynamics of other systems.

The melting has been induced by the T-Jump technique and monitored by the time-resolved Mie scattering spectroscopy. In order to investigate how the presence of hydrogen bonds influence the melting dynamics, non-hydrogen-bonded systems have been chosen. Among them ethylenediamine and benzene present absorption bands resonant with the T-Jump pulse (1900 nm), and can be investigated without changing the setup. In addition, the attempts made to investigate clathrate hydrates of methane will also be presented.

2.5.1 Ethylenediamine

Ethylenediamine is the organic compound with the formula $C_2H_4(NH_2)_2$ and its melting point is 284 K.

An ethylenediamine crystalline sample has been prepared and the cell has been placed in the cryostat at T_0 = 279 K at ambient pressure and irradiated by a T-Jump pulse. A CW laser probe (λ_{probe} = 632.8 nm) has been used to probe the changes in the sample by the Mie scattering technique using the configuration for the transmission detection of figure 1.8a. The IR absorption band of ethylenediamine in the region of the pump is centered around 4933 cm^{-1}, and is due to the overtone of N-H stretching mode at $\sim$ 3360 cm^{-1} and the C-NH bending mode at $\sim$ 1600 cm^{-1}.

The analysis of the acquired kinetic traces has been performed in the same way as water ices. The time constant τ_1 values as a function of the absorbed energy E, ranging from 0.6-2.7 mJ/pulse, are reported in figure 2.21 superimposed to the results obtained for water ices. As can be seen in the figure, the values for ices and ethylenediamine crystal are in good agreement at low energy values ($E <$ 2 mJ/pulse), where the time constant τ_1 for ethylenediamine is comparable to ices. At higher energy values ($E >$ 2 mJ/pulse), τ_1 for ethylenediamine is higher than the one for ices at the same energy condition, revealing that the melting process is slower respect to the ices one. This result is unexpected for a system, such as ethylenediamine, whose crystalline structure is not characterized by the presence of H-bonds. However, this evidence could be related to saturation effects. In fact, the energy needed to obtain absorption saturation (calculated by the equation 1.2

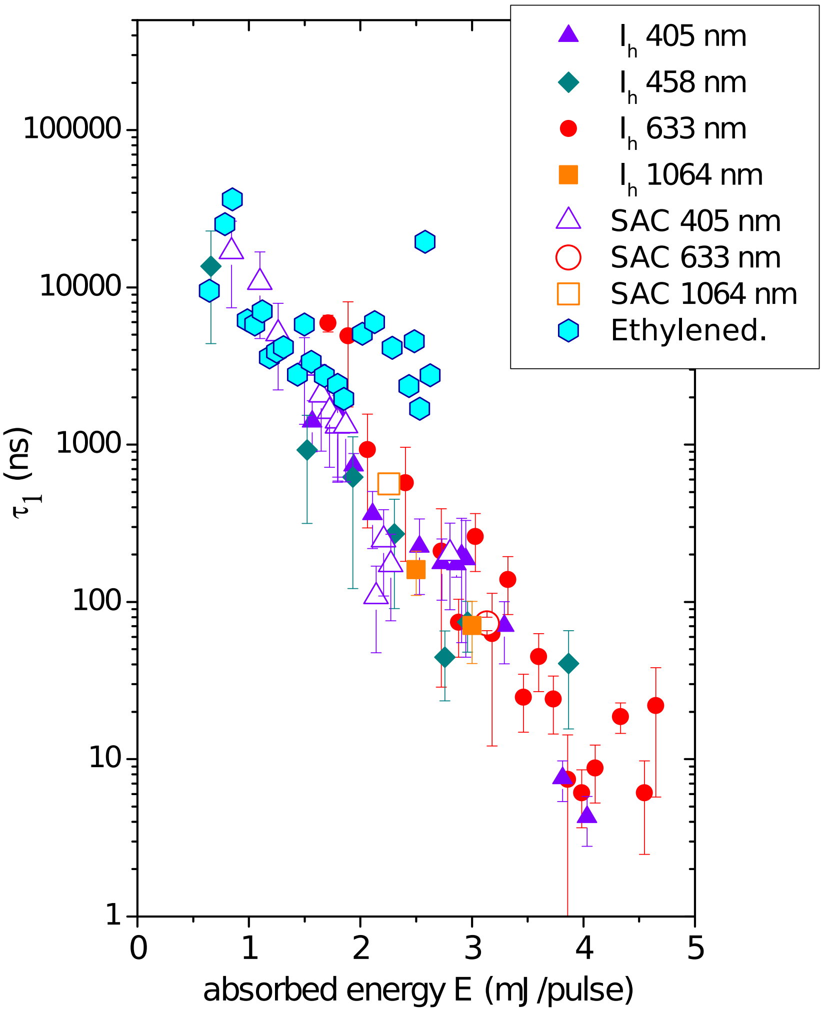

Figure 2.21: τ_1 values as a function of the absorbed energy E for ethylenediamine superimposed to the results for ices. Although the reported values are single shot measurements (not averaged), they are in good agreement with the data collected for water samples at low energy values ($E < 2$ mJ/pulse). At $E > 2$ mJ/pulse, τ_1 for ethylenediamine is higher than the one for ices at the same energy condition.

in paragraph *Calculation of the saturation threshold for absorption* of chapter 1) for ethylenediamine is 2.77 mJ. For energy higher than 2.2 mJ the time constant τ_1 becomes independent of the pulse energy, as can be seen in figure 2.21, suggesting that the saturation regime has been reached. In the same way, the absorption saturation for a water ice I_h sample can be calculated, and it is 9.9 mJ, very far from the energy employed, meaning that there is no absorption saturation for the ice samples. Further investigations will be needed to better characterize the melting dynamics of ethylenediamine, especially for T-Jump energies between 2 and 3 mJ/pulse.

Also the recrystallization dynamics of ethylenediamine has been investigated, and the time constant for refreezing as a function of the temperature difference (ΔT = |T_0 - T_m|) is shown in figure 2.22, superimposed to the one of ice I_h. As expected, the recrystallization occurs on the milliseconds time scale.

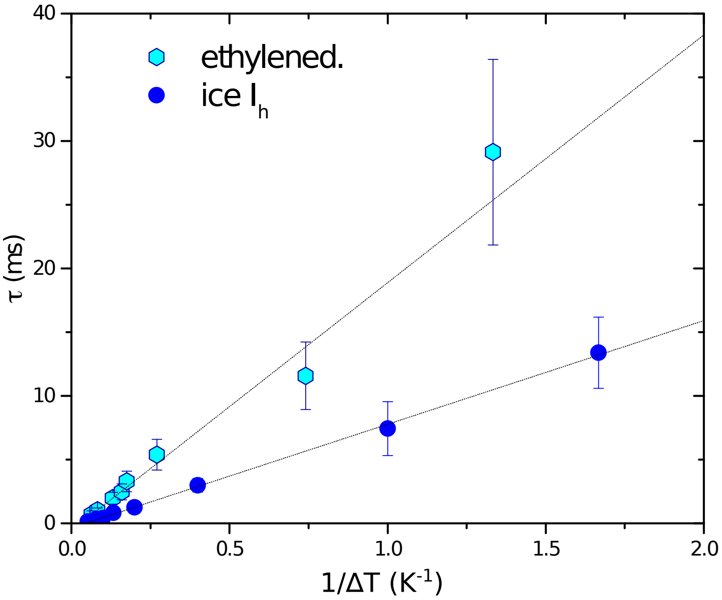

Figure 2.22: Dependence of ethylenediamine on the temperature (ΔT) superimposed to the one of ice I_h.

As the rate constant of the freezing process (k = $\frac{1}{\tau}$) is concerned, the dependence of k on the temperature difference (ΔT) is reported:

$$k_{freezing} \propto \frac{dQ}{dt} \propto \Delta T \tag{2.13}$$

where $\frac{dQ}{dt}$ is proportional to the thermal diffusion coefficient (w). The thermal diffusion coefficients for ice and ethylenediamine are, respectively, w_{ice} = 0.555

$Wm^{-1}K^{-1}$ and $w_{etil.} = 0.257\ Wm^{-1}K^{-1}$. $\frac{dQ}{dt}$ is also proportional to $\frac{1}{m}$, where m is the angular coefficient of the linear fit (black lines in the figure 2.22) of our data for ice and ethylenediamine. Different slopes (black lines) can be calculated for ice and ethylenediamine: $m_{ice} = 0.0081$; $m_{etil.} = 0.0194$. The ratio between the slopes is $m_{ice}/m_{etil.} = 0.42$, while the ratio between the thermal diffusion coefficients is $w_{etil.}/w_{ice} = 0.46$. This shows that the trend of the rate constant k as a function of temperature (ΔT) is consistent with what expected by theoretical model (equation 2.13). As in the case of water ices, also the refreezing time constant for ethylenediamine is regulated by the heat exchange with the environment.

2.5.2 Other systems

Benzene

A crystalline sample of benzene at 277 K and room pressure has been irradiated by a single T-Jump pulse (with incident energy ranging from 3 to 9 mJ/pulse) and monitored by the CW laser probe ($\lambda_{probe} = 632.8$ nm) using the configuration for the transmission detection.

No dynamics of phase transition has been acquired because the sample reacts, and dark spots appear after the excitation pulse. This could be due to a less efficient thermalization of the sample through the lattice phonons and to the fact that the decomposition of the benzene molecule into carbon and hydrogen ($C+H_2$) could be favored by the fact that they are stable compounds at that temperature.

Methane clathrate hydrate

A sample of clathrate hydrate of methane has been synthesized in our Lab in the MH-I phase, by using the procedure reported in chapter 1, and loaded in a SAC at 0.67 GPa and ambient temperature.

The characterization of the sample by FTIR and Raman spectra is reported in the following chapter. The sample has been irradiated by a single T-Jump pulse (with incident energy of about 9 mJ/pulse) and monitored by the CW laser probe ($\lambda_{probe} = 632.8$ nm) using the configuration for the transmission detection.

No dynamics of phase transition has been acquired because the sample reacts. In the Fig.2.23, images of the SAC observed with the optical microscope before (left) and after (right) the laser shot are shown. After the irradiation, the formation of dark spots close to the gasket can be observed. The lower shadow is due to a crack formed in the sapphire anvil after the pulse, which is responsible for the cell opening and the pressure decreasing to a value of 0.18 GPa.

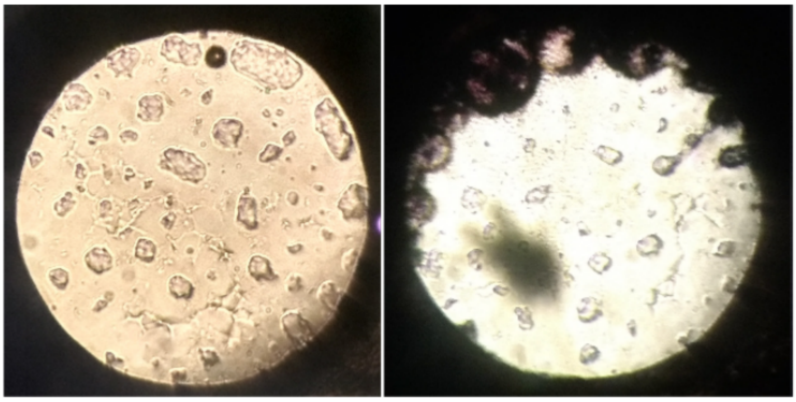

Figure 2.23: Images of the MH-I methane clathrate in the SAC observed with the optical microscope before (left) and after (right) T-Jump pulse. The formation of dark spots close to the gasket can be observed. The lower shadow is due to a crack formed in the sapphire anvil after the pulse.

The formation of dark spots suggests a possible photochemical transformation. The IR spectra of the sample acquired before and after the T-Jump experiment are reported in the Fig.2.24 (left) with their difference (right). The difference between the IR spectra of the sample before and after the excitation shows a weak band at 2135 cm^{-1}, due to the stretching of CO, and the intensification of the narrow band at 2342 cm^{-1}, attributed to the CO_2 asymmetric stretching. These two bands attest the methane oxidation. This could be probably attributed to thermal dissociation of water and the consequent formation of hydroxil radicals which readily attack the methane molecules in the cages. In addition, in the region between 300 and 1000 cm^{-1} of the Raman spectrum (Fig.2.25) the peaks related to gaseous hydrogen molecule can be observed. They can be attributed to the roton of hydrogen with J = 0, 1, 2.

As a consequence of this result, we decided to investigate another clathrate hydrate sample containing argon atoms. The dynamics investigation by the T-Jump technique of melting in the argon hydrate has not been performed yet. As a preliminary study, the IR and Raman characterization of such sample has been performed and is reported in chapter 3.

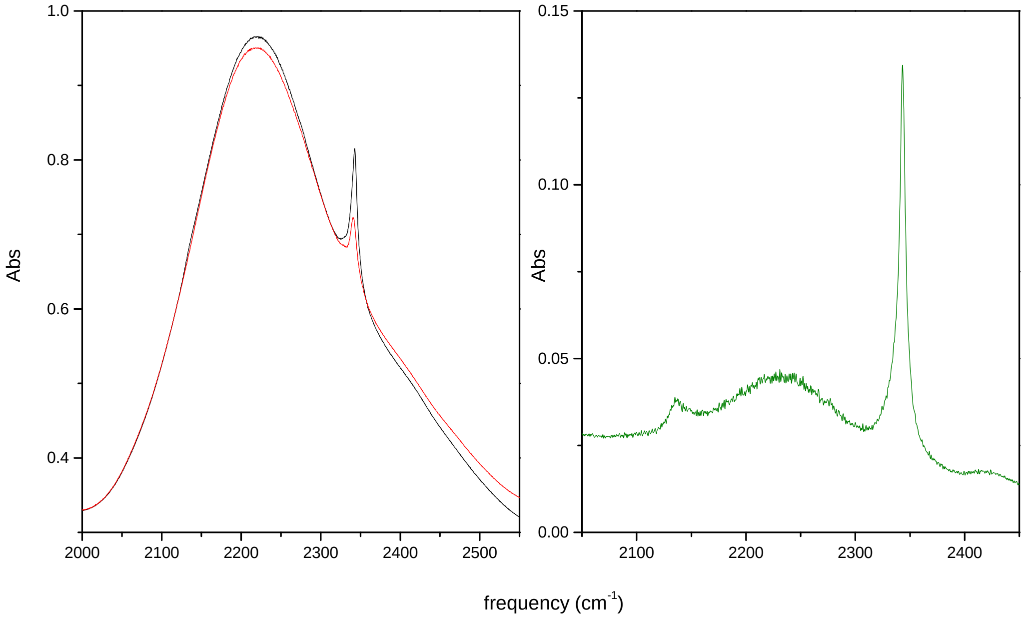

Figure 2.24: IR spectra of the MH-I sample acquired before (red curve) and after (black curve) the pulse, on the left. The difference spectrum (right) shows the presence of two bands at 2135 and 2342 cm^{-1}, respectively attributed to the stretching mode of CO and to the asymmetric stretching mode of the CO_2.

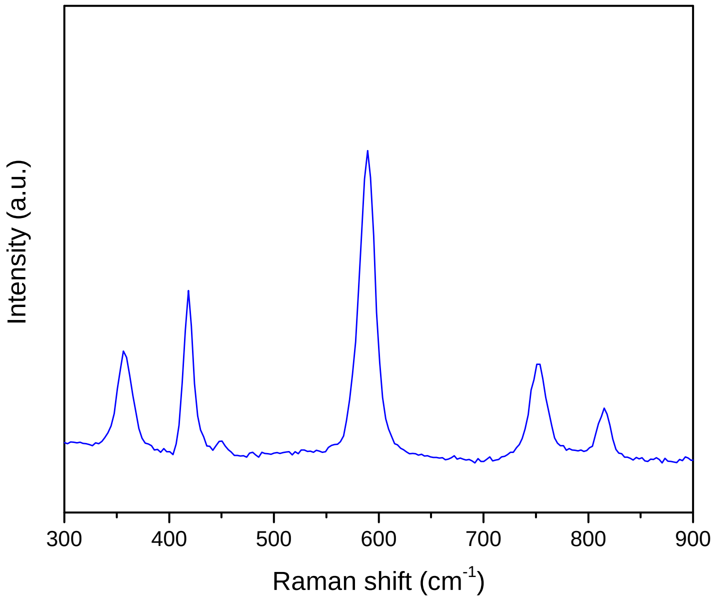

Figure 2.25: Raman spectrum of the MH-I sample acquired at T = 295 K and P = 0.18 GPa after the T-Jump pulse. The peaks observed are related to gaseous hydrogen molecule. They are at 356, 589, and 815 cm^{-1}, respectively the roton of hydrogen with J = 0, 1, 2. The peaks at 418 and 751 cm^{-1} are due to the anvil sapphire.

2.6 Conclusion

Time-resolved Mie scattering has been successfully used to monitor the melting and the successive recrystallization of water ices I_h and VI with a nanosecond time resolution in the entire mesoscopic regime [40].

The melting has been induced by an ultrafast IR pulse resonant with a vibrational combination band of water [20]. The pulse is absorbed by ice, generating a super-heated crystal at temperature up to 400 K, where melt nuclei quickly form within the first nanosecond after the pulse [31]. The melting dynamics has been probed from a few nanoseconds after the heating pulse, allowing for the access to an already nucleated sample. In fact the melt seeds form after the fast relaxation of the absorbed energy (tens of picoseconds) and grow over the time. The entire growth dynamics of these melting seeds are monitored in the *mesoscopic* regime, from a few nanoseconds to tens of milliseconds, up to the successive and complete recrystallization.

The experimental data are excellently reproduced in all their detailed features by a simple phenomenological model where a monodisperse distribution of liquid spherical particles grows, rearranges during coalescence, and decreases its volume when the temperature reaches again the melting temperature. More in detail, the estimate of the size of the scattering particles is based on the use of a monodisperse suspension where all of the particles have the same average diameter. This approximation is reasonable because of the homogeneous irradiation provided by the setup. For $t \geq 0.3$ ms, the angular distribution of the scattering has been used to estimate the particles size, while for shorter delays ($t \leq 0.3$ ms), where the off-axis scattering is too weak to be detected in a reliable way, experimental data have been supported by a model. As an infinite number of combinations of concentration (C) and diameter (D) would give the same absorbance value, in order to estimate the diameter of the scattering particles from a single angular configuration, in addition to the approximation of a monodisperse suspension, some constraints on the concentration have been introduced. The used simulation indicates that C is approximately constant until a sudden coalescence occurs, causing a sharp decrease in the absorbance. The correspondence between simulated and experimental curves is also confirmed by the effect obtained by increasing the initial concentration in the simulation and the delivered energy in the experiment which leads to the same shape in the absorbance curves. To estimate D(t) in our samples, C has been assumed to be constant up to the time

(t_C) where coalescence occurs, indicated by the sharp maximum in the absorbance (A_1). At t_C a simple cubic packing of the water spheres has been assumed, giving rise to sudden coalescence, and thus linking C and D by the relation $C = \frac{1}{D^3}$. The D and C values at t_C have been calculated, by using the code described by Bohren and Huffman for monodisperse suspensions of spherical scatterers [62]. C has been fixed to this value for all the times $t < t_C$, obtaining corresponding D(t) values. The calculation has been performed to obtain the absorbance values versus time, A(t), which are the result of averaging the τ_1 and A_1 resulting from the fit of several traces. The diameters obtained from these values with fixed C have been then plotted against time, using the time evolution of the corresponding A values. The D(t) values obtained with this method are a good approximation to have an idea of the time and the size scales of the melting and recrystallization processes, and show that the melting is far from instantaneous, occurring on a microseconds time scale. Despite the strong approximations used, we are able to provide a precise time evolution of the droplets' dimensions. Such time evolution is an important result in an attempt to connect the previous knowledge of the initial 250 ps [5, 31, 58] to the macroscopic domain. The melting implies the relaxation of the super-heated lattice at ice/water interfaces. However, the temperature at these interfaces decreases in time due to melting itself, which is endothermic, and thus the growth slows down as it proceeds, as also reproduced in calculations for the sub-nanosecond time window [58]. The heat exchange with the environment also contributes to slowing down the growth by decreasing the sample's temperature and eventually reverses the process. However, this has a much slower rate (micro- to milliseconds) and for $E \geq 2.5$ mJ does not affect the sample's behavior in the initial microseconds as demonstrated by the independence of τ_1 on T_0. Thus, in this time scale (3 ns–1 μs) the relevant dynamics are those of the lattice relaxation to its equilibrium liquid structure at $T > T_m$.

For our sensitivity, ice I_h and ice VI bulk samples melt with the same dynamics in the 3-ns to 1-μs time range. In fact, these measurements suggest that the differences in the growth of the molten fractions are very similar in the two ices, although they have different crystal structures and different volume changes upon melting. Probably, the largest difference between the two ices would appear in the nucleation process (the arrangement of the crystal structure is more likely related to nucleation kinetics), whose dynamics is not accessible in the investigated temporal range ($t > 3$ ns).

Thus, with this work, fundamental aspects of melting dynamics of water ices in a time domain previously unexplored, inaccessible also to many computational methods, have been unveiled.

CHAPTER 3

Clathrate hydrates

3.1 Introduction

The ability of water to assemble into complex hydrogen-bonded caged structures in the presence of certain molecules, such as hydrophobic organic ones, or noble gases, results in ice-like crystalline compounds, named *clathrate hydrates*. Clathrate hydrates are a class of inclusion compounds where water acts as host trapping the guests in cages formed by hydrogen-bonded water molecules [63]. The physical appearance of clathrate hydrates is similar to ice, but depending on the nature of guest molecules and pressure, hydrates can be found in conditions where water is liquid. In clathrates cages formation is stabilized by intermolecular repulsive interactions with the guest species [63]. The geometrical arrangement of water molecules in the clathrate gives rise to polyhedral structures which are particularly different compared to the structures that can be found in ices.

Clathrate hydrates, and in particular the methane ones which are the most widespread on Earth, have been and are studied for their potential economic implications and the problems they generate from technological and environmental point of view. Natural gas hydrates can be found on Earth confined in large amount in permafrost regions or in ocean floors. It has been estimated that the total natural gas reserves present in these structures are around 10^{28} m^3, about twice the total fossil hydrocarbon reserve [63, 64]. Gas natural hydrates can be thus considered as a new potential fuel reserve. On the other hand, their unwanted formation within the methane gas pipelines makes the extraction of crude oil more difficult and causes many problems related to technological aspects. Their inclusion characteristics can be revolutionary for gas storage applications without the use of high pressure devices. Their formation can also be employed as separation technique for desalination of sea water. The methane clathrates reserves naturally present in polar ices and permafrost regions are also a potential environmental risk, related to the uncontrolled release of methane in the atmosphere due to the global warming and contributing to the greenhouse effect [65]. More information on hydrate formation and its dynamics at microscopic level would greatly contribute to the development of problem management strategies in oil and gas supply lines, as well as to increase the knowledge on the storage and recovery of fuels or carbon dioxide sequestration, also for their use as valuable resource for energy.

As clathrate hydrate formation and decomposition are concerned, the mechanisms regulating the dynamics of construction of water cages and the diffusion of one system in the other one, are among the aspects of greatest interest. Despite the well known thermodynamics of the clathrate hydrate formation and decomposition, the kinetics of nucleation and growth is still not completely elucidated [66]. In particular, the small lengths and short time scales (nanoseconds) of these phenomena and their stochastic nature have prevented so far the experimental characterizations at molecular level of the processes themselves, so that they have been explored mainly by computational methods [67–69]. These theoretical works have shown how the process of clathrates crystallization proceeds through the characteristic formation of three-dimensional cages with a characteristic time of reorientation of the water molecules to form the cages that is about half the time required for the formation of the crystalline lattice in ice. In the typical experiment designed for the macroscopic characterization of hydrate formation, the hydrate guest is brought in contact with water at a certain pressure and temperature conditions, and the formation is detected through the decrease of gas pressure. The process occurs in three phases [70]: an induction time, in which the mixture stays metastable within the thermodynamic domain of the clathrate hydrate, followed by a rapid growth period, being the first step of the hydrates formation in which they grow very rapidly, and finally a slow growth. In practice, the nucleation is always heterogeneous and usually occurs at the vapor-liquid interface [63], it has a stochastic nature and determines the induction time. The induction time can be reduced increasing the supercooling of the mixture and it can be significantly lowered if the hydrates are reformed from a mixture obtained from a previously dissociated hydrate. This is probably due to the supersaturated solution deriving from the dissociation itself [71] or to long living residual structures acting as a templating agent [72]. These facts have to be taken in account in the characterization of the kinetics of the fast clathrate hydrates formation (first phase of the formation), which is the main phenomenon implied in the growth of hydrates themselves.

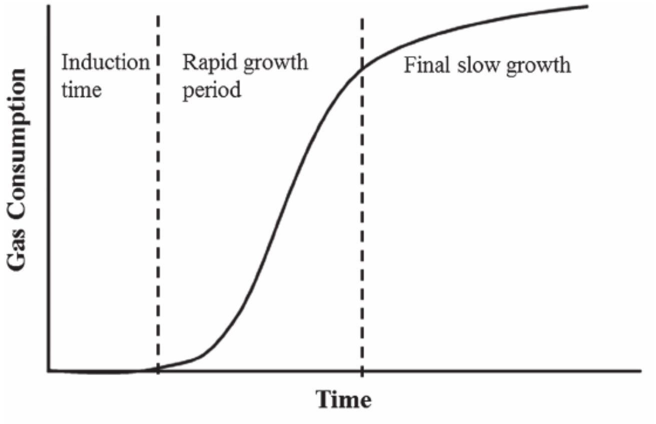

Figure 3.1: The three stages of clathrate formation are shown. The graph indicates the trend of gas consumption as a function of time in the three phases characterizing the hydrate formation. During the growth phase, sigmoidal trend of gas consumption can be observed (picture from ref.[66]).

When the formation of gas hydrates starts from ice spheres the Shrinking-ice-core model can be taken into account [73, 74]. According to this approach, during the gas hydrate formation process each ice particle transforms to a shrinking ice core covered by a growing hydrate shell. The reaction is supposed to start at the surface and proceed toward the center of the ice particle. In detail, two stages of the hydrate formation process can be distinguished. The first relatively rapid stage is the ice surface coating when an initial hydrate film nucleates on and spreads over ice particles. The second one (stage II) is the further growth of the hydrate shell around each shrinking ice core in the sample. This stage implies two constituent steps: the clathration reaction itself at the inner (ice-hydrate) as well as external (gas-hydrate) interfaces, and the gas/water mass transport (diffusion) through the hydrate layer.

3.2 Clathrate structures

Clathrate hydrate structures are guest-host crystalline structures, where the type of structure depends on the guest and on temperature and pressure conditions. Seven different types of hydrate crystal structures have been identified or proposed [63]. At ambient temperature the three most common structures, particularly for gas hydrates, are the I, II, and H structures (Fig.3.2). The unit cell of structure I (sI) comprises two 5^{12} cages and six $5^{12}6^2$ cages. The nomenclature used to describe the polyhedral shape of the cavity is of the type $X^N Y^M$, where X and Y indicate the polygon constituting the face, and N and M the number of faces. Thus, the notation 5^{12} indicates that the cage is composed of 12 pentagonal faces, and $5^{12}6^2$ indicates the cage has 12 pentagonal and 2 hexagonal faces. Similarly, a unit cell of structure II (sII) comprises sixteen 5^{12} cages and eight $5^{12}6^4$ cages, and $4^3 5^6 6^3$ in structure H (sH) indicates that the cage has 3 square faces in addition to 6 pentagonal and 3 hexagonal faces. In the sI structure the water molecules give rise to a cubic lattice (spatial group *Pm3m*), where small, indicated with the

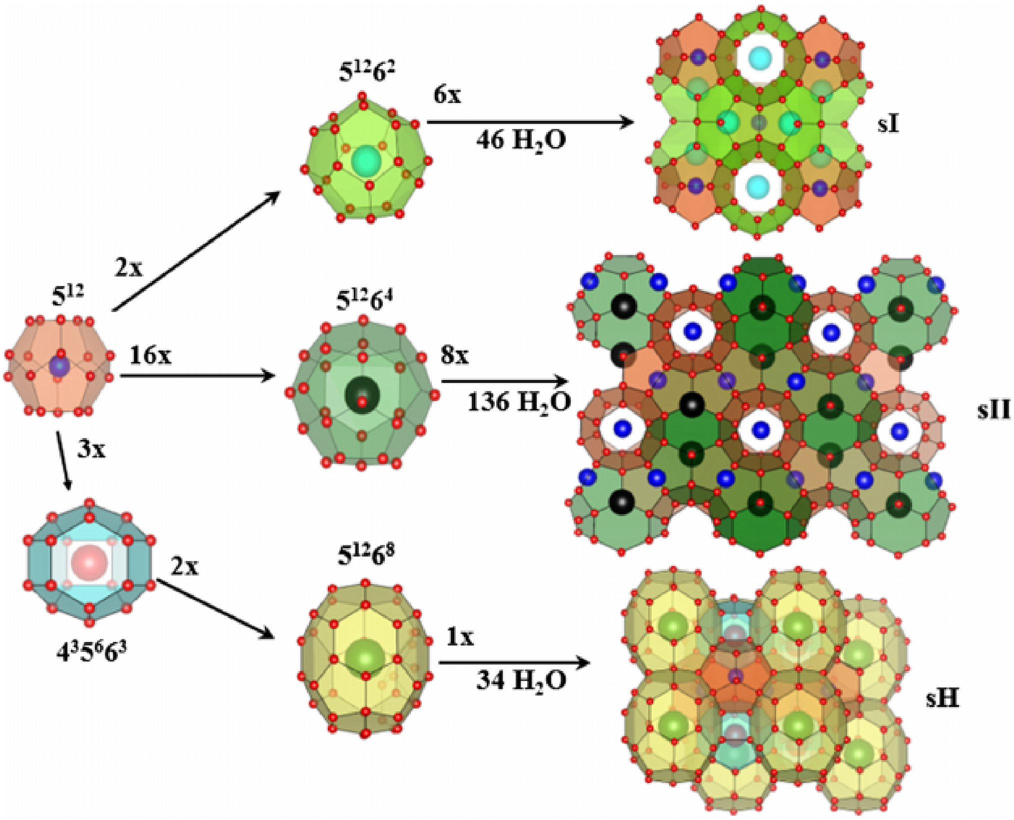

Figure 3.2: Clathrate hydrate cages and crystal structures are shown (from reference [66]). The three most common structures for clathrate hydrates are structures sI, sII, and sH.

notation 5^{12}, and large, indicated with $5^{12}6^{2}$, cavities are present. The unit cell is made of 2 small cages and 6 large cages (follow the arrows of figure 3.2 for sI), and the ratio between the cages type is 1:3 containing 46 water molecules. In case of complete filling, with one guest molecule for each cage, the number of hydration is 46:8 = 5.75. The sII structure is a face-centered cubic lattice (spatial group *Fd3m*), with a ratio between the cages type of 2:1, being 16 small (5^{12}) and 8 large ($5^{12}6^{4}$) cages. The structure contains 136 water molecules generating 24 cavities, thus the number of hydration for a complete filling is 136:24 = 5.67. Finally, the sH structure is characterized by the hexagonal lattice (spatial group *P6/mmm*), with three types of cages: 3 small (5^{12}), 2 medium ($4^{3}5^{6}6^{3}$) and 1 large ($5^{12}6^{8}$) cages. The ratio among the cages types is therefore 3:2:1. The structure has 34 water molecules and 6 cavities, thus the hydration number is 34:6 = 5.67 for complete filling. The type of structure that can be formed depends on T,P conditions and on the guest species: the number and type of guest molecules/atoms determine the range of stability of the hydrate and the ratio between the components (stoichiometry).

In order to experimentally investigate the melting process and the recrystallization of a clathrate hydrate sample through pump and probe techniques, two kind of clathrates, the methane and the argon hydrates, have been taken into account in this work. Homogeneous samples are required for this purpose, thus the synthesis of the hydrate sample has been performed in a specially designed autoclave and by following the procedure described in paragraph *Synthesis procedure* of chapter 1. In this way the excess of one of the two components can be minimized or avoided, unlike what usually occurs when the synthesis is carried out directly inside the anvil cell. In fact, it is experimentally difficult to introduce the components in stoichiometric ratio within the anvil cell for the hydrates synthesis. All the details of the synthesis and loading procedures are described in chapter 1. Also the loading in the anvil cell of the synthesized clathrate should avoid the alteration of the hydrate composition, which naturally occurs when the hydrate is exposed to the atmosphere. After the loading, in order to characterize the sample spatial homogeneity, the samples have been observed with the optical microscope and characterized through IR and Raman spectroscopy. The re-crystallization after melting has also been characterized in the two kind of hydrates, because the clathrate re-formation after melting without separating into the two components is a fundamental requirement for investigating the formation dynamics of clathrate.

3.3 Clathrate hydrates of methane

The phase diagram of methane hydrate is shown in figure 3.3 [12]. The lower pressure structure of the clathrate hydrate of methane is the MH-I, stable at ambient temperature up to around 0.9 GPa with sI conformation. The MH-II phase is stable in the range 0.9-1.9 GPa at ambient temperature with sH structure. During the phase transition MH-I (sI) to MH-II (sH), the ratio water/methane decreases giving rise to a structure richer in methane with consequent ice VI formation [75]. The MH-III phase is stable from 1.9 GPa up to 40 GPa. Its structure is not made of cages, since the water molecules are arranged in the space to form, through the H-bonds, channels similar to those typical of the ice I_h structure. This structure is also named “filled ice” as methane molecules are placed inside the channels [76].

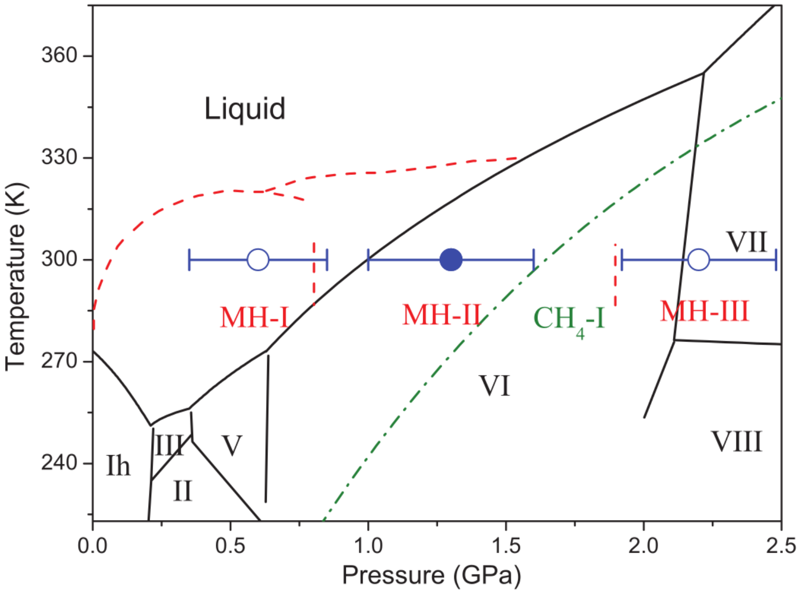

Figure 3.3: Phase diagram of water (solid lines), methane (dashed dotted line), and methane hydrates, MH, (dashed lines). The formation of methane hydrates is indicated by the close circle, whereas the open circles indicate that, within the duration of 1000 s, MH crystal formation is not yet observed. The horizontal bars represent the range of pressures experienced by the samples. All these data are related to the experimental work reported in references [12].

Compared to free methane, in the clathrate the vibrational band of the symmetric C-H stretching mode of methane (at around 2900-3000 cm^{-1}) becomes asymmetric and shifts to higher frequencies due to the different chemical environment experienced by the methane molecules inside the different cages [76].

However, the IR spectroscopy is not useful for the characterization of the different methane clathrate phases due to the presence, in the same IR spectrum region of methane, of the typical broad band of O-H stretching mode belonging to water. This band goes from 2900 to 3800 cm^{-1} and is characterized by a strong absorption. Thus, for the MH characterization, the Raman spectra have been acquired, where the methane band can be easily observed above 2900 cm^{-1}. In figure 3.4 the Raman spectra for the C-H stretching modes of methane molecules in MH-I, MH-II, and MH-III phases are shown.

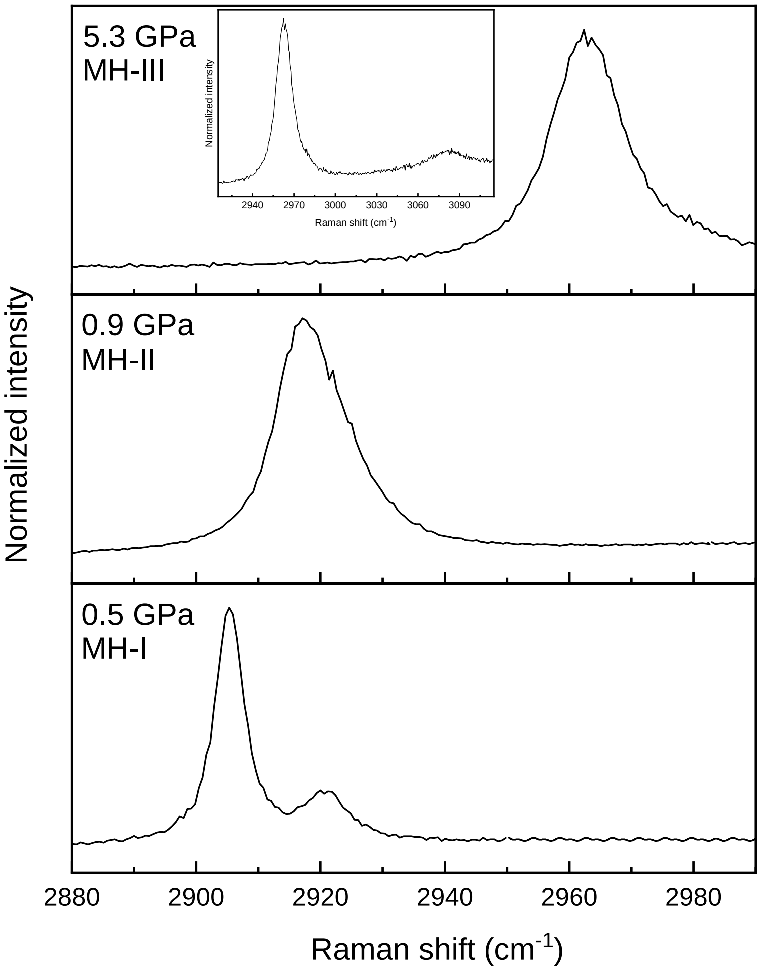

Figure 3.4: Raman spectra for C-H stretching modes of encaged methane molecules acquired at ambient temperature at different pressure in MH-I, MH-II, and MH-III phases (respectively at 0.5 GPa, 0.9 GPa and 5.3 GPa). In the inset the symmetric (at around 2960 cm^{-1}) and asymmetric (at around 3080 cm^{-1}) C-H stretching modes are shown for MH-III.

The Raman spectroscopy allows to distinguish the presence of water and free methane or clathrate methane in our samples, as can be observed in figures 3.5, allowing to reveal the homogeneity of the hydrate, as will be later discussed.

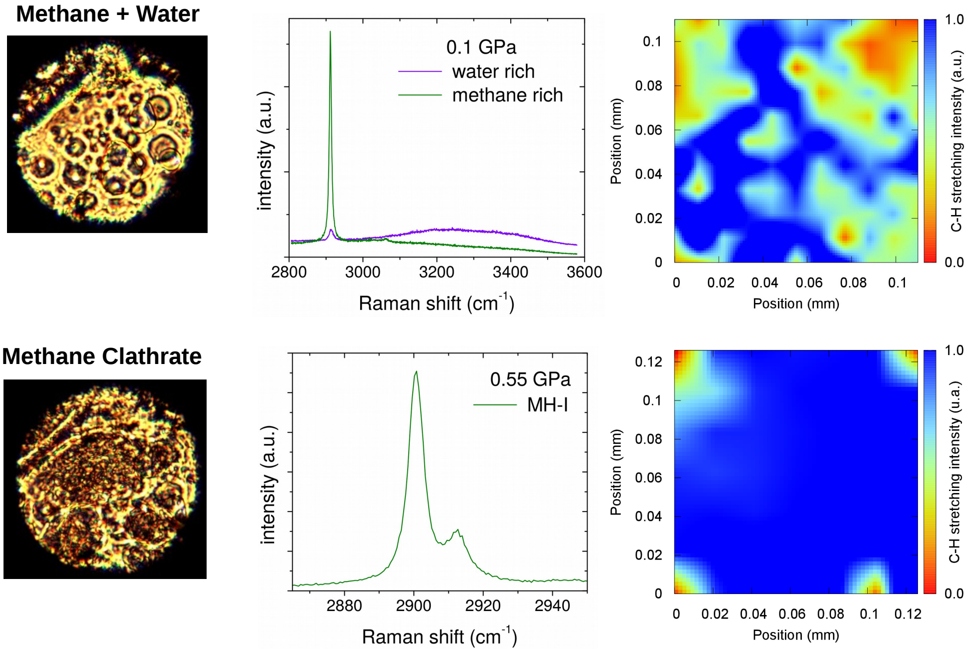

Figure 3.5: Photo, Raman spectrum and Raman map of unmixed sample at 0.1 GPa (free methane and water) and of clathrate in the stability region of phase MH-I. The Raman map is built by plotting the intensity of the methane band (of the spectrum on the left) in the C-H stretching mode region versus the position in the sample (both x and y spatial directions).

3.3.1 Characterization of methane hydrate sample

The methane clathrate hydrate sample synthesized by the procedure described in paragraph *Synthesis procedure* of chapter 1 has been characterized through Raman spectroscopy to investigate its homogeneity.

The sample at ambient temperature and 5.3 GPa, according to the phase diagram in figure 3.3, is in the stability region of the filled ice phase (MH-III). A photo of the sample in the diamond anvil cell is shown in figure 3.6. The homogeneity of the hydrate has been verified through the Raman map of figure 3.7 showing the methane band intensity of the symmetric C-H stretching mode versus the position in the sample (both x and y spatial directions).

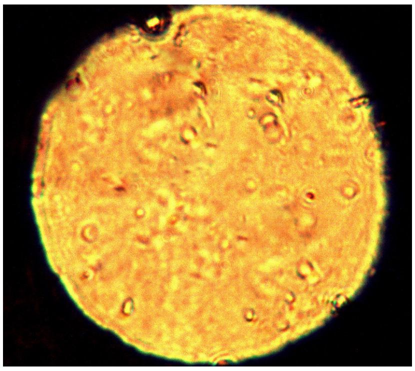

Figure 3.6: Photo of the methane clathrate sample at 5.30 GPa in the domain of filled ice phase (MH-III).

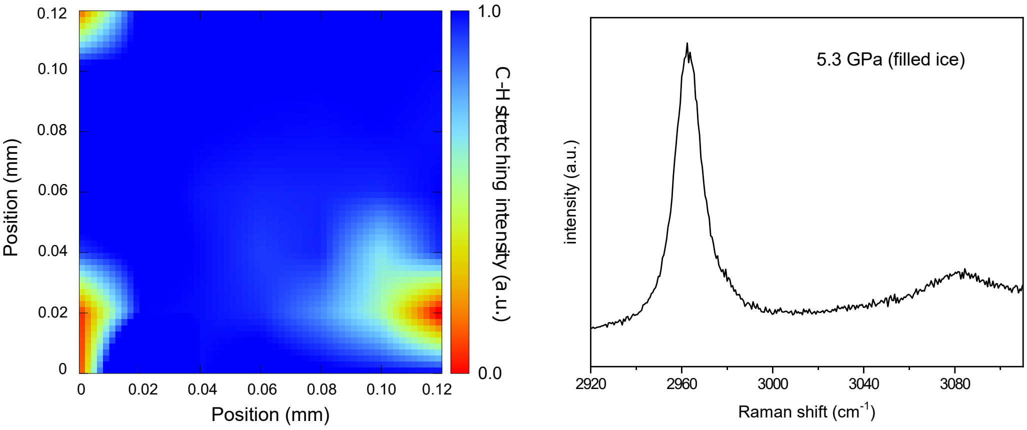

Figure 3.7: (Left) Raman map of the methane band intensity of the symmetric C-H stretching mode (low frequency in the spectrum reported on the right) versus the position in the sample (both x and y spatial directions). It shows an homogeneous sample. (Right) Raman spectrum of clathrate methane in the C-H stretching modes region at 5.3 GPa and ambient temperature (MH-III). Both the symmetric and asymmetric C-H stretching mode can be observed at such pressure, respectively at around 2960 cm^{-1} and 3080 cm^{-1}.

A Raman spectrum of the map corresponding to the MH-III at 5.3 GPa is reported on the right of Fig. 3.7. In methane hydrates at such pressure both the symmetric and the asymmetric C-H stretching mode of the methane molecule are visible. In our spectra, in good agreement with the work of Schaack et al. [77], these two bands can be observed respectively at around 2960 cm^{-1} and 3080 cm^{-1}, confirming the formation of the filled ice structure. The IR spectrum of the sample, showing the presence of water and methane bands, was completely saturated.

3.3.2 Characterization of melting and recrystallization

IR measurements

In order to verify the re-crystallization of the clathrate after melting, the IR spectroscopy can be successfully employed to monitor the vibrational band at about 2220 cm^{-1}, combination of the bending with an external mode, which is common to ices and hydrates (about 2220 cm^{-1} in ice I_h and 2218 cm^{-1} in MH-I). This band is very sensitive to the solid-liquid phase transition due to its dependence on the hydrogen bond, allowing to use it as a probe for monitoring the transition. The comparison between the IR absorption bands of ice I_h and liquid water is reported in figure 1.12 of chapter 1, showing a red shift and an intensity decrease passing from solid to liquid phase.

IR spectra have been acquired as a function of temperature at constant pressure (steps of 5°C between each spectrum). The sample has been heated by a resistive heater and the temperature has been measured through a thermocouple placed on the gasket. The temperature range under investigation goes from ambient temperature to around 15°C above the temperature where melting is observed. A controlled cooling has been performed to observe the reversibility of the process. In the following the IR spectra for the MH-I (Fig.3.8) and MH-II (Fig.3.9) phases are shown, certifying that the melting and recrystallization of the sample occurred in both phases.

The melting has been observed at 45.8°C in the MH-I sample, and, on cooling, the crystallization started at 38.8°C. In the MH-II sample the melting occurred at 50.3°C, whereas the begin of solidification has been observed at 43.3°C. As can be deducted, the temperature where the crystallization starts is always lower than the temperature of the melting, indicating a quite broad range of metastability. This is typical of water structures, where a higher supercooling degree is needed because of the strength of the hydrogen bonds network of the liquid which determines

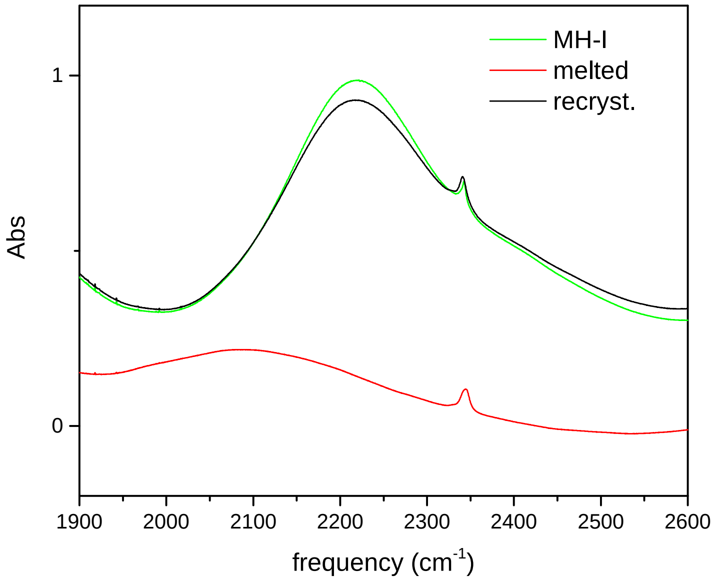

Figure 3.8: IR spectrum for a MH-I sample at 0.67 GPa and ambient temperature before melting (in green), after melting at 0.67 GPa and 45.8°C (in red) and after 48 hours from the crystallization onset (in black) at 0.67 GPa and ambient temperature. The narrow band at 2340 cm^{-1} is due to impurities attributable to the asymmetric stretching mode of CO_2 loaded inside the cell during the loading procedure.

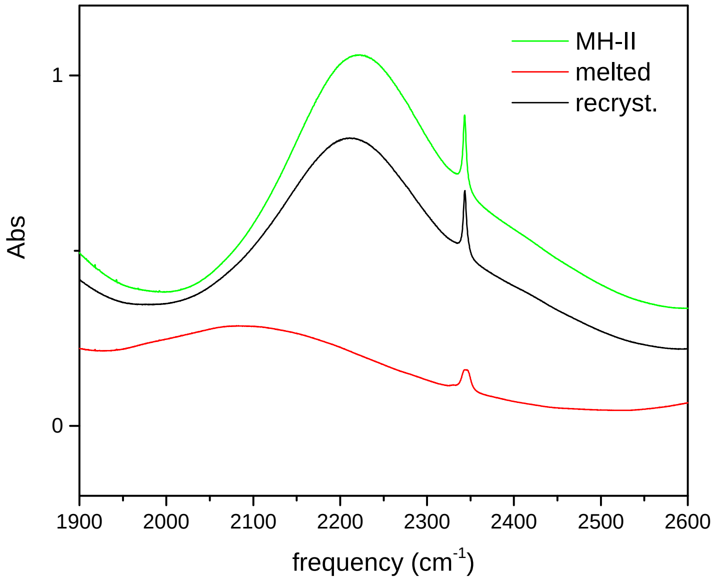

Figure 3.9: IR spectrum for a MH-II sample at 0.88 GPa and ambient temperature before melting (in green), after melting at 0.88 GPa and 50.3°C (in red) and after 16 hours from the crystallization onset (in black) at 0.88 GPa and ambient temperature. The narrow band at 2340 cm^{-1} is due to impurities attributable to the asymmetric stretching mode of CO_2 loaded inside the cell during the loading procedure.

a further energy barrier to the formation of the crystal lattice [72]. The slow recovery of the crystalline sample, as indicated by the spectra acquired after many hours from the crystallization onset (see the black curves of Figs.3.8 and 3.9), is likely due to a progressive increase in the crystalline structure quality, meaning defects in the crystal lattice that disappear. In fact, at temperatures close to the melting an efficient thermal annealing of the structure can occur.

Raman measurements

After the recrystallization, the two samples (MH-I and MH-II) have been characterized through Raman spectroscopy to investigate their homogeneity.

MH-I sample after recrystallization The Raman map of figure 3.10 is built by plotting the ratio between the areas of the methane band in the C-H stretching mode region for free methane and clathrate versus the position (both x and y spatial directions) in the sample. The red regions in the map indicate the clathrate hydrate of methane in phase MH-I reformed after melting inside the cell, whereas the regions of the sample containing free methane are those colored in blue. The Raman spectra of the Raman map are reported for both the red and blue regions in figures 3.11 and 3.12, respectively. Figure 3.11 shows the methane clathrate Raman bands related to the C-H stretching mode at 0.67 GPa and ambient temperature, which gives rise to two bands at 2905 and 2920 cm^{-1} related to

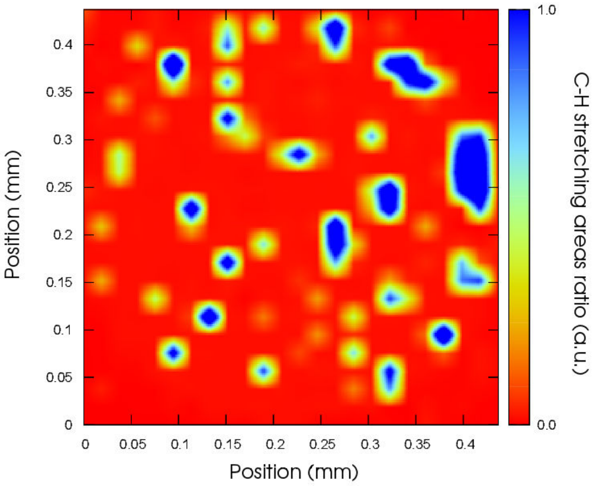

Figure 3.10: The Raman map of the re-crystallized MH-I sample (at 0.67 GPa and ambient temperature) shows in red the clathrate hydrate of methane and in blue the free methane.

methane molecules in large and small cages, respectively. SI hydrates only require a single guest molecule for each cage type, thus their intensity ratio should be 3:1 as the number of large and small cages characterizing such structure [78–80]. In the sample are also present regions where free methane dominates, as can be seen in figure 3.12, giving rise to a third band at 2915 cm^{-1}.

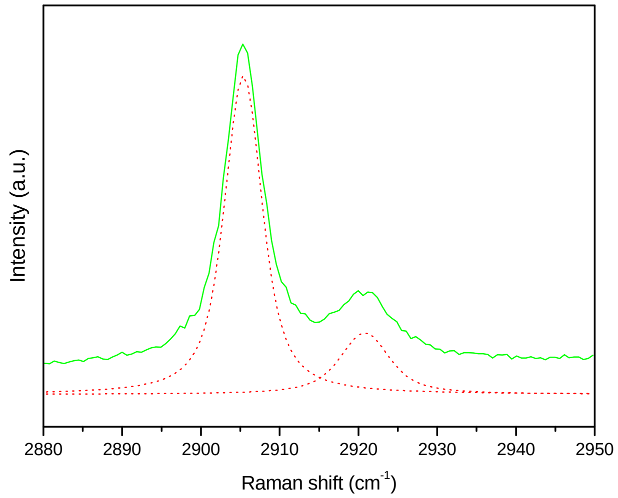

Figure 3.11: Raman band of MH-I in the C-H stretching region at 0.67 GPa and ambient temperature (green curve) and the fit, revealing the presence of two bands (red curves) related to the two kind of cages occupied by methane in the sI structure. The bands at 2905 and 2920 cm^{-1} correspond to large and small cages, respectively.

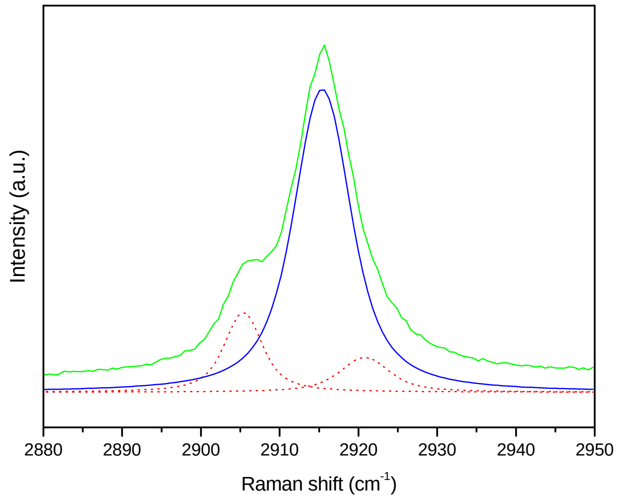

Figure 3.12: Raman band of MH-I in the C-H stretching region at 0.67 GPa and ambient temperature (green curve), where the red curves are the two bands related to the cages occupied by methane, and the blue band at 2915 cm^{-1} is attributable to free methane.

The average ratio between the areas of the two bands at 2905 and 2920 cm^{-1} of our MH-I sample is 3.97, as emerges from the figure 3.13. In fact, the distribution of the areas ratio of the two methane bands is centered at that value. Since the intensity of the Raman bands is not dependent of the type of cages where the molecule is found, the deviation from the expected ratio for an ideal MH-I clathrate, which is 3, indicates the presence of small empty cages or large cages occupied by two methane molecules per cage. In fact, unlike natural SI methane hydrates where single occupancy of cages is typically found [81], a higher occupancy of large cages with respect to small cages can be observed for synthetic MH-I.

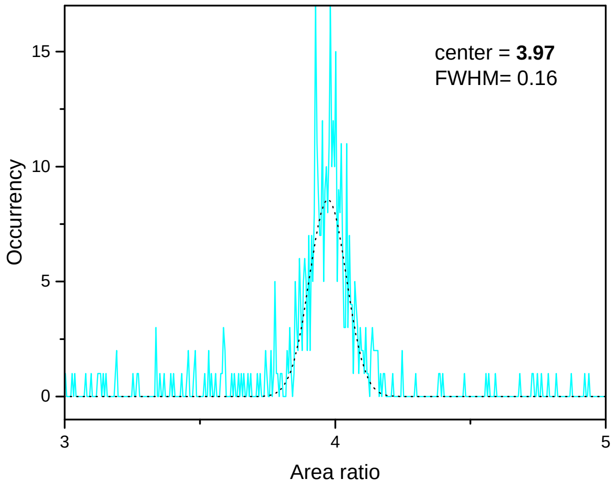

Figure 3.13: The distribution of the ratio between the areas of the two methane bands (large/small cages) in our re-crystallized MH-I sample is centered at 3.97.

MH-II sample after recrystallization The Raman band in the methane C-H stretching region for the MH-II recrystallized sample is shown in figure 3.14. At 0.88 GPa and ambient temperature the two bands of the C-H stretching mode in the different cages are not resolved and they can be obtained only by spectral decomposition of the strongly asymmetric band centered at about 2920 cm^{-1}. The two red curves, obtained by the fit, correspond to the molecules in the cages characterizing the sH clathrate structure. The ratio between the areas of these bands is 1.33, slightly lower than the expected one, which is 1.5, and in good agreement with data from Shimizu et al. [82]. Despite the three cages in sH hydrate, our Raman spectra show two bands. This may be because the two small cages have almost the same average radii [80, 83], and, as a result, CH_4 molecules encaged inside them show almost the same frequencies. Namely, the methane

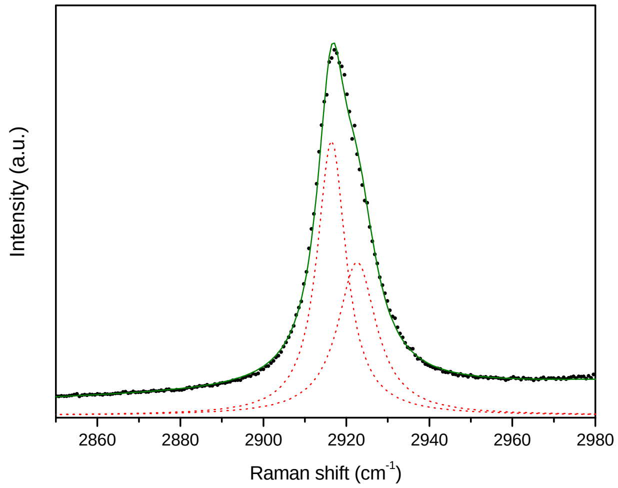

Figure 3.14: The Raman band in the methane C-H stretching region for MH-II at 0.88 GPa and ambient temperature. The fit revealed the presence of two methane bands (red curves) at 2917 and 2921 cm^{-1} related to the molecules in the cages characterizing the sH structure. These bands at low and high frequencies correspond to a large cage and small cages, respectively.

molecules filling the two small cages may present one broad Raman band at higher frequency and the methane molecule in the larger cage shows also one Raman band at lower frequency, as can be seen in Fig. 3.14.

Other characterization of samples homogeneity after recrystallization from the melt

The characterization of MH-II and MH-I samples after recrystallization from the melt has been performed through Raman spectroscopy to investigate the homogeneity.

A MH-II hydrate sample has been heated at 1.7 GPa up to 99°C when the melting has been observed by direct microscope observation. Then the sample has been cooled to ambient temperature at constant pressure within the domain where the phase MH-II should form. The Raman spectrum revealed the presence of free methane, Fig.3.15 (right), and the Raman map, Fig.3.15 (left), of the methane C-H stretching intensity shows high sample inhomogeneity. This results are consistent with the acquired IR spectrum reporting fluid methane and ice VI.

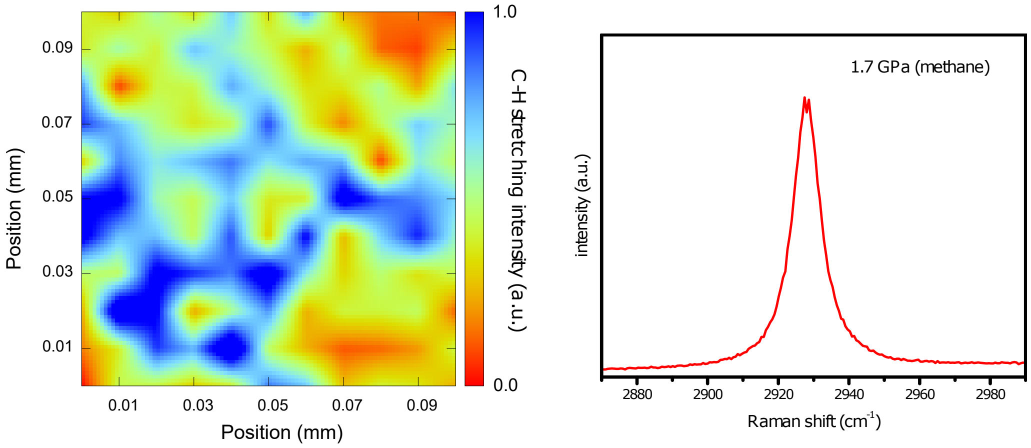

Figure 3.15: (Left) Raman map of the intensity of the methane band (spectrum reported on the right) versus the position in the sample (both x and y spatial directions). The blue regions indicate free methane, and the red ones corresponds to water ice VI. (Right) Raman spectrum of free methane in the C-H stretching region at 1.7 GPa and ambient temperature, after melting and cooling.

A MH-I hydrate sample has been heated up to 102°C at 0.3 GPa and cooled down to ambient temperature at constant pressure within the T,P conditions of the MH-I phase. Observations with the microscope have shown the formation of bubbles likely due to gaseous methane in liquid water. The appearance of the sample is reported in figure 3.16. No Raman signal of clathrate has been detected, as it is shown by the Raman map (Fig. 3.17) which reveals the presence of water with methane bubbles inside, indicating de-mixing of the two components. In order to regenerate the MH-I phase, the pressure has been raised till the clathrate formation which has been observed at 0.6 GPa at ambient temperature.

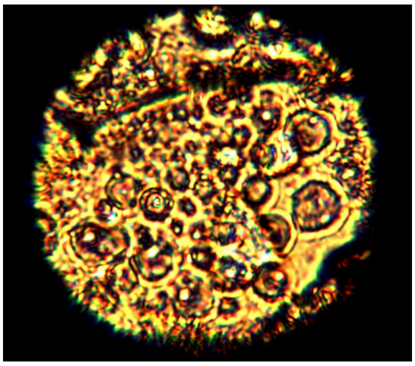

Figure 3.16: Visual appearance of the de-mixing sample. Methane bubbles and liquid water can be observed all over the sample.

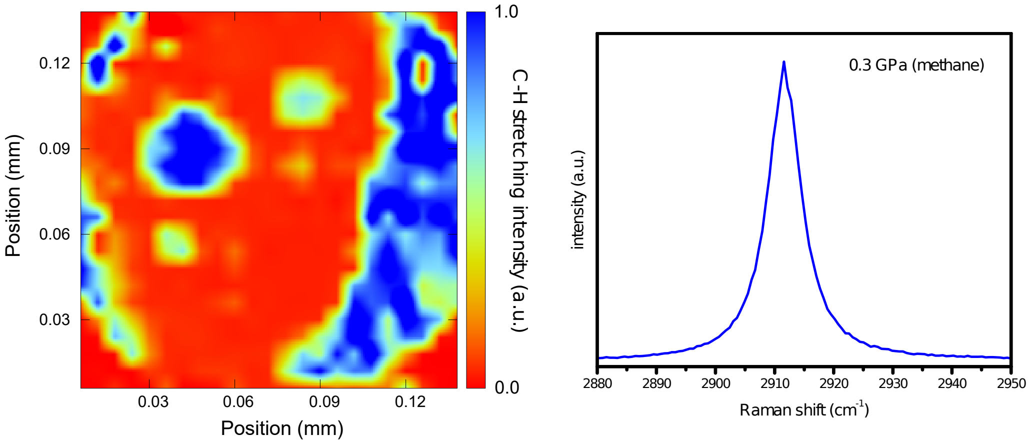

Figure 3.17: (Left) Raman map of the intensity of the methane band (spectrum reported on the right) versus the position in the sample (both x and y spatial directions). The blue regions indicate bubbles of free methane and the red ones corresponds to water, indicating the de-mixing of the two components. (Right) Raman spectrum of free methane in the C-H stretching region at 0.3 GPa and ambient temperature, after melting and cooling.

By decompressing the so reformed MH-I phase at ambient temperature, the complete melting is observed only below 0.05 GPa, while by compressing again in presence of a clathrate seed, the formation of the clathrate is observed, and it is completed only over 0.6 GPa. The Raman spectrum of the reformed MH-I sample is reported in figure 3.18 with the relative Raman map. The formation is slow and it can be easily followed by eye at the microscope, as can be observed in the sequence of photos reported in figure 3.19 acquired at intervals of few seconds.

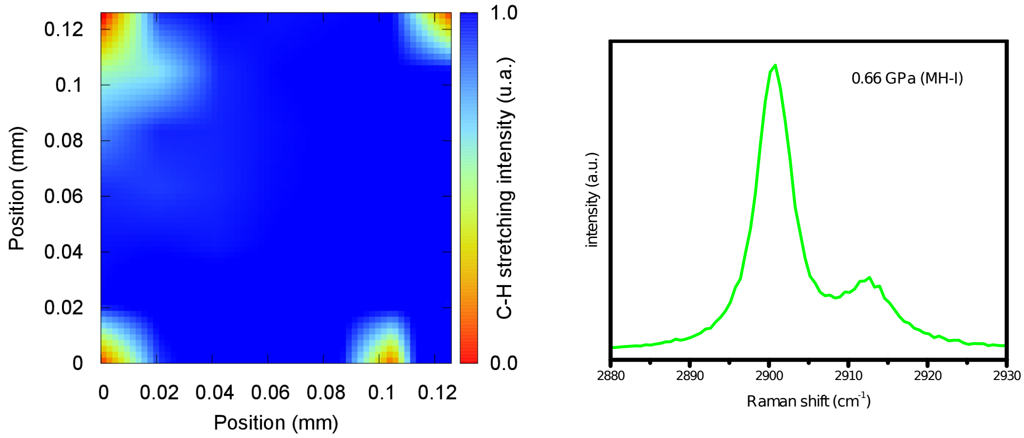

Figure 3.18: (Left) Raman map of the intensity of the methane band (spectrum reported on the right) versus the position in the sample (both x and y spatial directions). The map shows an homogeneous sample. (Right) Raman spectrum of clathrate methane in the C-H stretching region at 0.6 GPa and ambient temperature (reformed MH-I sample).

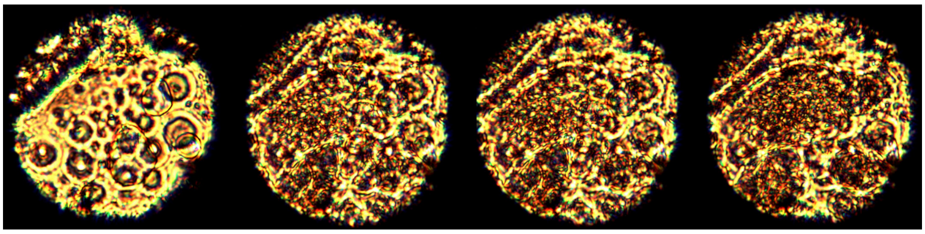

Figure 3.19: Sequence of photos of the sample during the clathrate formation (crystallization) process which takes place at constant pressure of 0.6 GPa and ambient temperature.

3.4 Clathrate hydrates of argon

The phase diagram of argon hydrates is shown in figure 3.20 [47]. In these hydrates the guest-host interaction is of purely van-der-Waals type. The phase which is stable from ambient pressure to 0.46 GPa (phase h in figure 3.20) appears to be the typical cubic structure sII with variable degree of filling of the large cavities. The stoichiometry of this compound has been determined by Manakov et al. under high-pressure conditions resulting in Ar·4.5H_2O and Ar·4H_2O at 0.34 GPa and 0.43 GPa, respectively [47]. The argon hydrate existing in the pressure range 0.46-0.77 GPa has a hexagonal structure (sH), indicated as h_1 in figure 3.20. The h_2 hydrate, stable in the 0.77-0.95 GPa range, has a primitive tetragonal unit cell, which does not correspond to any known type of gas hydrates. It is the first example of gas hydrate containing only one type of polyhedral cavity with 14

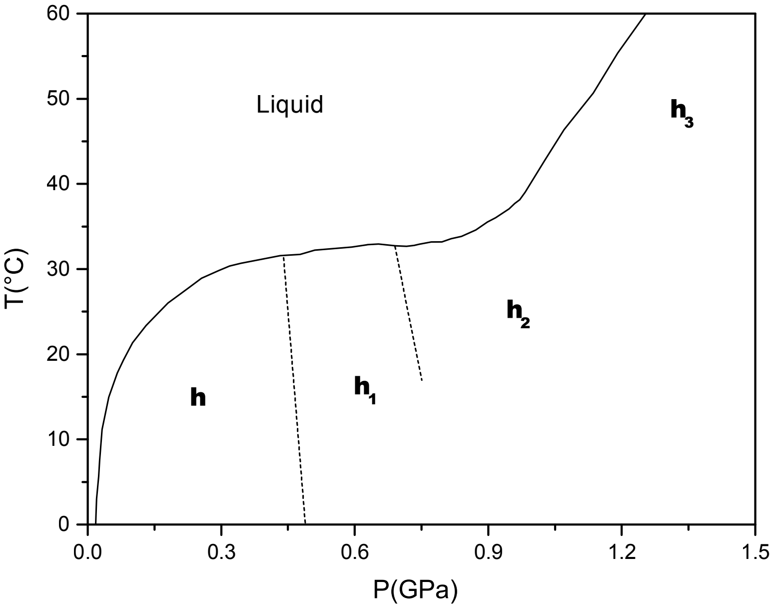

Figure 3.20: Phase diagram of the argon-water system [47]. It shows the different hydrate phases h, h_1, h_2, and h_3.

faces. This type of polyhedrons are space-filling: two argon atoms occupy each cavity, the unit cell contains 12 water molecules, and the hydrate stoichiometry is $Ar \cdot 3H_2O$.

3.4.1 Characterization of argon hydrate sample

The argon hydrate has been synthesized, and after its loading in the SAC and decompression (see details in chapter 1), the pressure of the sample at ambient temperature was 0.64 GPa. The T,P conditions are in the stability range of the clathrate hydrate phase h_1 of argon, as can be verified from the phase diagram (Fig.3.20). The appearance of the sample of argon clathrate in the sapphire anvil cell is shown in Fig.3.21.

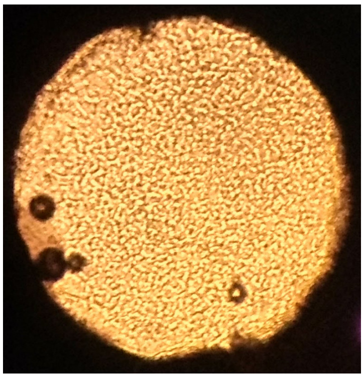

Figure 3.21: Argon clathrate after the loading at 21.2°C and 0.64 GPa. It is in the phase h_1.

In order to verify the formation of the desired phase of argon hydrate, the phonon bands in the low frequency region of the clathrate Raman spectrum are observed. Despite this being an uncommon diagnostic method to detect the hydrate formation, the presence of bands typical of phonons at the T,P conditions of stability for the hydrate, where the sample otherwise would be separated in liquid water and argon, ascertains the presence of the crystalline hydrate.

The Raman spectrum in the low frequency region for the argon clathrate sample is shown in figure 3.22. Two main features have been observed: the band at 230 cm^{-1}, which is common to ice and it is associated to the deformational type of vibrations of water molecules, and the band at 130 cm^{-1}, typical of clathrates and related to the resonance interaction of the motions of guest atoms with the lattice modes [84]. Also weaker bands at 80, 55 and 33 cm^{-1} have been observed, which have been predicted for the clathrate structure [85].

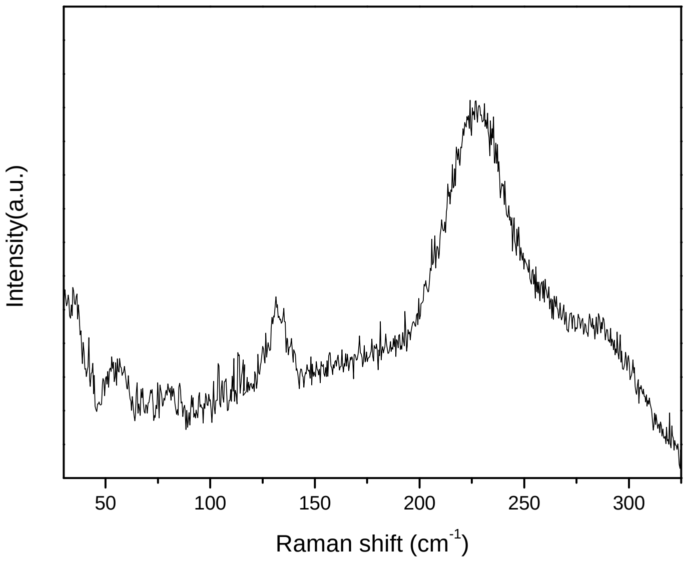

Figure 3.22: Raman spectrum of the argon clathrate hydrate in the low frequency region acquired at 0.64 GPa and 21.2°C. It shows the bands at 230, 130, 80, 55 and 33 cm^{-1} typical of hydrates.

By looking at the intensity of the phonon band at 230 cm^{-1} all over the sample the presence of a homogeneous phase is confirmed.

3.4.2 Characterization of melting and recrystallization

The temperature of the hydrate has been raised to induce the melting, while the sample has been observed at the microscope. At 33.8°C and 0.61 GPa the melting has been observed by eye, indicated by bubbles of argon all over the sample. A Raman spectrum of the sample confirms the absence of crystalline structure as no phonons have been observed (see figure 3.23).

In order to reform the argon hydrate in the starting phase (h_1) and characterize the crystallization process, the temperature has been lowered, while the sample has been visually observed. At 25°C a modification of the sample appearance occurred: the argon bubbles disappeared. After 12 hours the sample appearance (reported in figure 3.24 on the right) indicates borders of phase in the centre of the sample. Raman spectra have been acquired in the region around these borders of phase to characterize the sample composition. The Raman map showing the intensity of the phonon band at 230 cm^{-1} as a function of the position in the sample is reported in figure 3.24 (left).

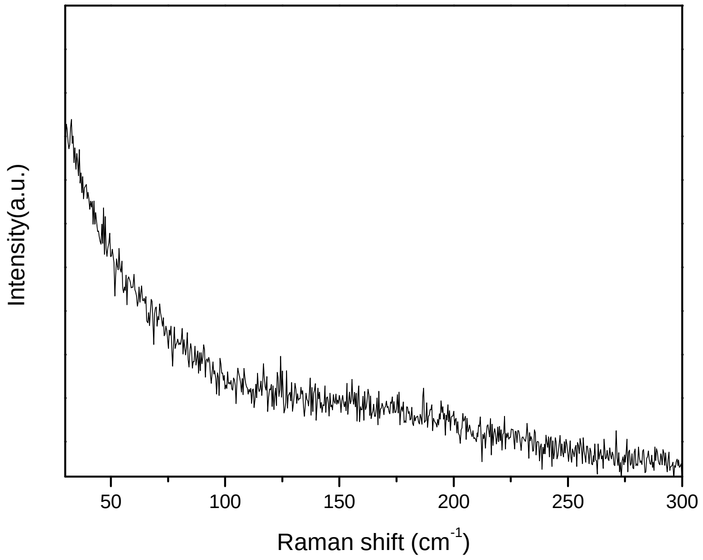

Figure 3.23: Raman spectrum in the low frequency region of the melted argon clathrate at 0.61 GPa and 33.8°C. No phonons have been observed, confirming that the sample is melted.

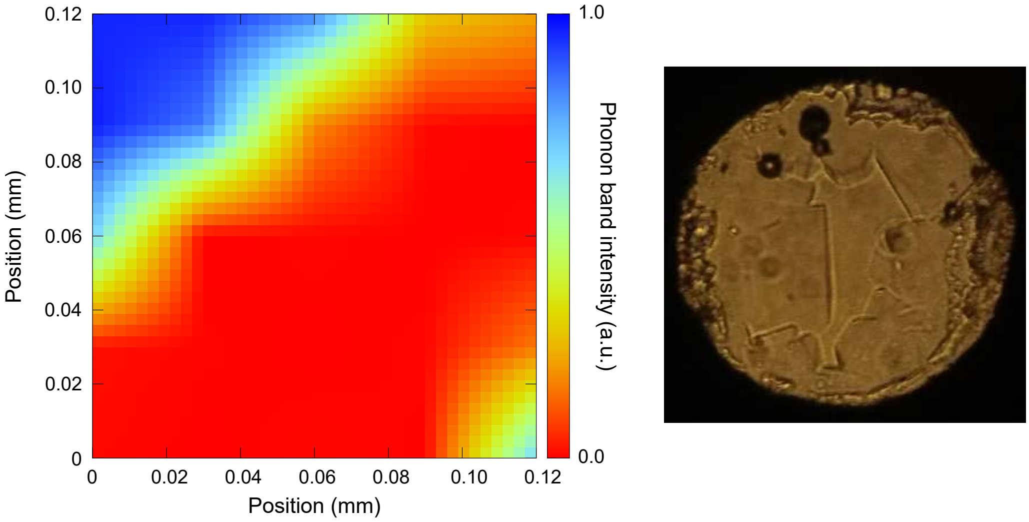

Figure 3.24: (Left) Raman map showing the intensity of the phonon band at 230 cm^{-1} as a function of the position (both x and y spatial directions) in the sample. The map is at a phase border, in the central part of the cell (picture on the right). The blue region indicates the presence of the argon hydrate. In the red region no clathrate can be observed, indicating the separation of the two components (liquid water and gaseous argon). (Right) Photo of the sample showing phase borders in the centre of the cell.

The evolution of the sample aspect was very slow: after 3 days at around 21°C and 0.6 GPa the water in the centre disappeared, and the appearance is more homogeneous (figure 3.25).

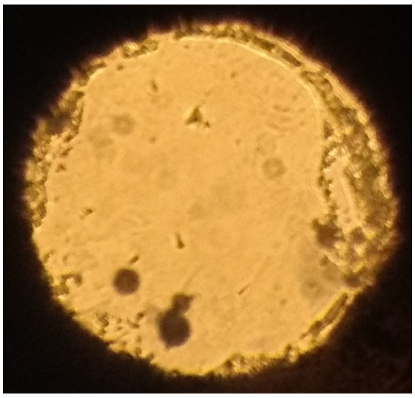

Figure 3.25: Photo of the sample after a week at constant T-P conditions. It appears more homogeneous.

The recrystallization process of the argon clathrate from the melt has been also monitored by acquiring IR spectra as a function of time. We have used the absorption band at about 2200 cm^{-1} (figure 3.26) to follow the crystal evolution. The evolution of the band frequency and of the full width at half maximum (FWHM) as a function of time are shown in Figs. 3.27 and 3.28. The onset of the kinetics measurement (t = 0 h in figure 3.27 and 3.28) corresponds to the time when the first variation of the IR band has been observed.

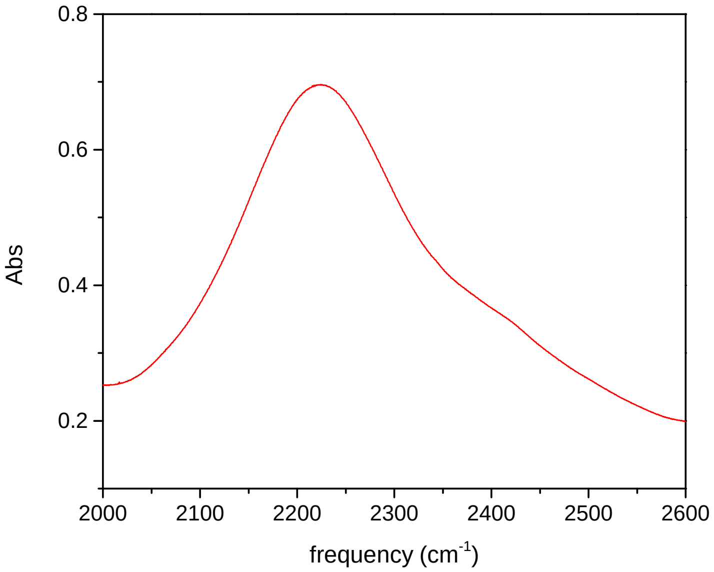

Figure 3.26: IR absorption spectrum of argon clathrate in the region around 2200 cm^{-1}.

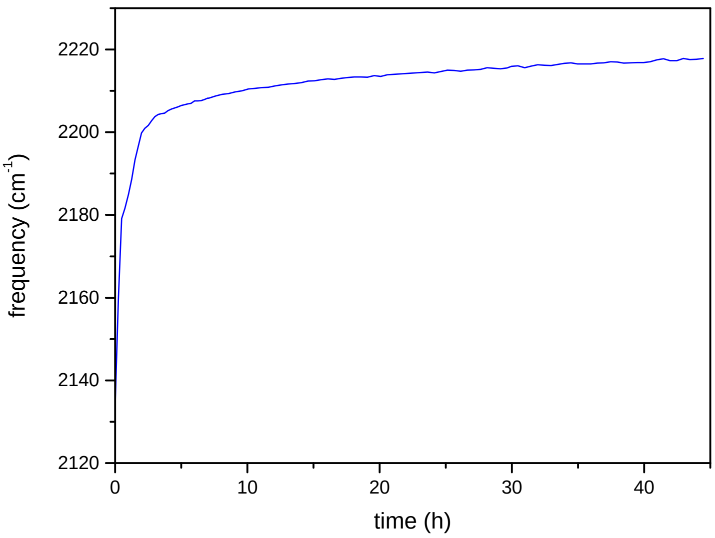

Figure 3.27: Evolution of the frequency of the band maximum (band of Fig. 3.26) as a function of time.

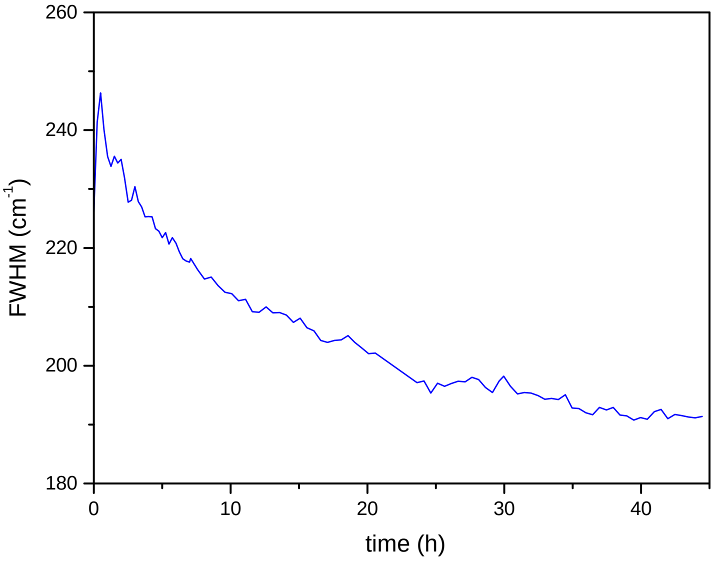

Figure 3.28: Evolution of the full width at half maximum (FWHM) of the band of Fig. 3.26 as a function of time.

A significant variation in the first 2 hours can be observed in both the graphs. As in the case of methane clathrate, this step is followed by a slow process (tens hours). A possible interpretation of this experimental evidence refers to a particularly complex model for the clathrate nucleation and growth processes [66]. According to this hypothesis, at the beginning of the clathrate formation, the guest molecules/atoms are dissolved in water (supersaturation of the solution) and small bubbles of gas form within the liquid phase. A small cage (5^{12}) forms around a guest molecule/atom, while other guest molecules/atoms are adsorbed on the cage faces. This determines the formation of pseudo-structures, named *blobs*, which are long-life aggregates composed of small cages with adsorbed guests molecules/atoms all around, separated by water molecules. In this step, the cages form and break repeatedly until the formation of a critical nucleus. Then, an amorphous clathrate forms as mix of different hydrate structures, becoming, over the time, a unique crystalline structure. The last step involves structural rearrangements also through the annealing process which is favored by maintaining the T,P conditions close to the phase transition ones.

In the curve of figure 3.27 different slopes can be observed related to different temporal regimes probably due to the phenomenon described above. By looking at the two graphs in the range from 0 to 2 hours, the curves probably reveals the amorphous clathrate formation starting to the *blob* pseudo-structures and its evolution over the time. The diffusion process of the guest argon atoms inside the cages of the clathrate structure, which leads to the typical clathrate crystalline structure, could have been detected. The regime from 3 to 40 hours is attributable to the slow progressive recovery of the crystalline structure quality of the initial sample.

These results could reveal that we are able to monitor the amorphous clathrate evolution and the diffusion of the argon atoms inside the preexisting water cages. A further characterization of the process through Raman spectroscopy to monitor the evolution, particularly between 0 and 2 h, of the phonon bands spectrum over the time is needed. This further investigation would help to correlate the results described above with the evolution of the cages occupation, explaining the mechanism of the phenomenon.

3.5 Conclusion

In this thesis different types of hydrates, both methane and argon clathrates, have been investigated in order to verify our ability in synthesizing and transferring to the anvil cell homogeneous samples and the capability of the hydrates to recrystallize from their melt. In addition, we have also investigated the kinetics of the crystallization, or more precisely the recovery of the crystal quality possessed prior the melting. The samples characterization has a fundamental significance for dynamics investigations of phase transitions realized through ultrafast pump and probe techniques. In order to investigate the melting dynamics of clathrate hydrates, the homogeneity of the initial sample is a fundamental requirement. In this way, interference from unmixed components is avoided. Thus, a working procedure to synthesize clathrate hydrates, both of methane and argon, has been developed, beginning with the design of a high pressure apparatus. Starting from ground ice and gaseous methane or argon we are able to synthesize homogeneous clathrate hydrates samples in the autoclave, by following a specific temperature program and reaching high pressure (up to 400 bar). The sample loading in the anvil cell (DAC or SAC) has been performed in dry atmosphere, avoiding external contamination. The maintenance of the homogeneity over the entire synthesis and loading processes has been verified by using FTIR and Raman spectroscopies. By Raman spectroscopy we are able to identify the methane or argon hydrate phase by detecting, respectively, the band of the symmetric C-H stretching mode of methane in the region around 2900 cm^{-1} and the phonon band around 230 cm^{-1} in the low frequency region of the argon clathrate spectrum. The IR spectroscopy, instead, has been successfully used to monitor the melting and recrystallization processes by following the absorption band of the water bending modes and librations in the spectrum region around 2200 cm^{-1}. The recrystallization from the melt has been characterized for the methane hydrate MH-I and MH-II phases, even if tens hours are needed to the sample at ambient temperature to recover the initial crystalline quality. Moreover, the reformation of the MH-I hydrate sample has also been possible by decompressing the system until the melting, and by compressing the unmixed components. In this way, the crystallization is obtained thanks to the presence in the sample of pre-existing seeds of crystallization. The same considerations reported for the MH-I and MH-II phases can be done for the h_1 phase of argon hydrate: after melting the recrystallization occurs but the recovery of the same crystal structure quality of the initial sample is the longest process. Moreover, the results obtained for the argon clathrate by monitoring the crystallization kinetics with IR spectroscopy offer information on a possible mechanism describing the diffusion of the guest into the host cages, according to a model of clathrate nucleation and growth reported by Warrier et al. [66].

In order to proceed in the direction of dynamics investigations of clathrate hydrates, this characterization study offers an initial but fundamental result, revealing the T,P conditions which allow the recrystallization from the melt and our ability to generate homogeneous samples.

CHAPTER 4

Melting dynamics by TRIR absorption

4.1 Introduction

In this chapter a new approach developed to access the first nanosecond after the T-Jump pulse is described.

The method reported in chapter 2, based on time-resolved *Mie scattering*, allows to monitor the phase transition only after the first nanoseconds (∼3 ns) after the pump pulse. Moreover, the scattering probe, being sensitive to interfaces between media with different refractive index, is not able to distinguish, in case of a multicomponent system, the different scattering species present in the sample during the phase transition. This happens for example when unmixed components (water and guest) are present in the sample. In this case, a correct insight into the melting and recrystallization dynamics at the molecular level can be gained only by a method able to directly quantify the melted portion generated in the heated sample volume, as can be the *transient infrared* absorption spectroscopy (TRIR). Indeed, as the infrared spectrum of the formed hydrate and the unmixed components is considerably different, the two phases can be detected and quantified as a function of time, allowing for a fine characterization of the dynamics of melting and crystallization. The transient IR probe, in fact, is sensitive to the vibrational bands typical of ices and clathrates and allows to appreciate the changes in the IR spectrum in time during the phase transition.

A previous work on 1.6-μm-thick ice I_h has already revealed the capabilities of time-resolved IR absorption spectroscopy to investigate the ice super-heating and melting dynamics after an ultrafast (femtoseconds) T-Jump [31]. In their work, the pump and probe experiment used as spectral signature the O-H stretching mode of water in D_2O which shows a strong absorption at around 3400 cm^{-1} in the IR spectrum. By exciting the O-H stretching mode of water (HDO:D_2O 15 M) the authors claim to superheat ice which persists over the monitored time interval of 250 ps after the pulse without completely melting. In fact, an incomplete melting (around the 33% of the irradiated volume) is still observed after 1.3 ns, consistent with the amount of energy delivered by the pulse which is not sufficient to fully melt the sample.

In the present work the (picoseconds) T-Jump technique has been coupled to the TRIR absorption spectroscopy to monitor the ice (and potentially clathrate) destruction and formation in time by probing the combination band of water due to bending and librational modes.

4.2 Experimental method

In the new experiment the Thermal Jump technique is coupled to the TRIR absorption spectroscopy to monitor the melting of ice I_h by probing the water vibrational band centered at about 2200 cm^{-1}. The band, attributable to the combination of bending and librational modes, is characterized by typical absorptions in the solid and liquid water phase as reported in figure 4.1.

The T-Jump pulse (pump), responsible for the increase of the sample temperature and thus the melting, is an energetic picosecond infrared pulse absorbed by the ice sample, which redistributes the thermal energy through the lattice modes (thermalization) in $\sim$15 ps [5]. The experimental apparatus for the transient absorption measurements is described in detail in section 1.2.5 of chapter 1.

Despite the duration of the employed pump and probe pulses being $\sim$15 ps and $\sim$100 fs, respectively, the temporal resolution obtained by the new experimental apparatus is $\sim$100 ps. This value has been obtained by detecting the $\sim$100-fs-long pulse at 800 nm with two identical photodiodes, and by looking at the distribution of the delays between the same pulse detected by the two photodiodes over 1000 pulses. The width of such distribution is 100 ps. This value is therefore given by the used detection system, i.e. the two photodiodes and the oscilloscope.

Thanks to the possibility to change the delay between pump and probe potentially to the infinity, also slow dynamics can be followed. The time window investigated in the present experiment goes from 100 ps after the pump pulse up

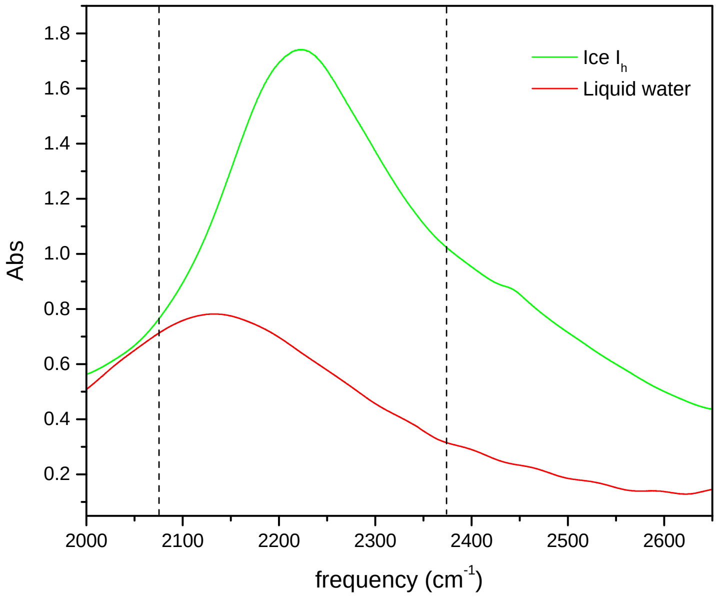

Figure 4.1: Comparison between ice I$_h$ (in green) and liquid water (in red) spectra. The shown band is attributable to the combination of bending and librational modes. The black dashed lines delimit the probed region.

to $\sim$1 μs. The experiment has been set to sample a $\sim$1.5-μs-wide time window around the pump pulse (15-ps-long). In this way we are sure to probe the duration of the entire melting process.

The experiment consists of pump and probe measurements with a repetition rate of 1 Hz. Each measurement is a single-shot event, where only one pump pulse is shot, and only one probe pulse monitors the system state. The polycrystalline ice sample, which is kept in a cryostat at static temperature and pressure conditions (-5°C, room P), reforms between a pump pulse and the following one. In this way, a fresh sample is present in each measurement. The employed incident energy of the T-Jump pulse was around 9 mJ/pulse, which corresponds to the maximum energy used in the Mie scattering experiment.

In each measurement an IR spectrum of the band centered at 2200 cm^{-1} has been acquired at a measured delay time Δt between pump and probe pulses (with $\Delta t = t_{probe} - t_{pump}$). The probed band contains information of the portion of melted ice (liquid) at a certain Δt, since it is due to the contribution both of the ice and the liquid band.

4.2.1 Data treatment

In figure 4.2 the IR spectra acquired with our setup at different delay times Δt are shown.

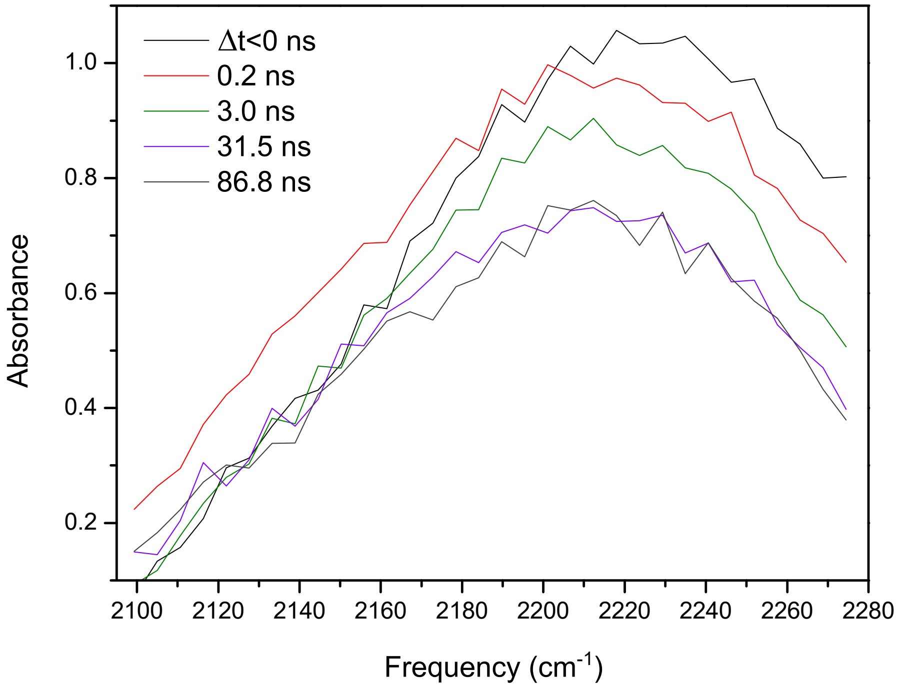

Figure 4.2: Experimental absorbance curves of our sample acquired by the TRIR setup at different delay times. The curves are subtracted of a constant value.

The spectra show the probed band, i.e. the band attributable to the combination of bending and librational modes. Such experimental absorbance curves are obtained by the following equation

$$A = -log \frac{I_{probe}}{I_{reference}} \tag{4.1}$$

where A is the absorbance value of the sample, I$_{probe}$ is the intensity of the probe beam detected by the MCT detector when it crosses the sample, while I$_{reference}$ is the detected intensity of the reference beam. All the acquired absorbance curves are subtracted of the same constant value, which is the absorbance value of the empty cell. Such value is obtained by the equation 4.1 when the probe beam crosses the empty cell. The value is experimentally due to the absence of absorption of the empty cell in the investigated frequency range, intensity losses by reflection on the cell windows and other optics, and the different intensities of probe and reference beams.

Two IR bands acquired at different delays are shown in figure 4.3 along with the fitting functions. The blue dots represent the acquired band at Δt < 0 ns, i.e. before the pump pulse, which is typical of the ice sample. The red dots correspond to the band acquired 5.6 ns after the pump pulse. The comparison between these two bands with the ones of figure 4.1 indicates the presence of a partially melted sample at Δt = 5.6 ns. In fact, the band acquired at such delay (red dots in figure 4.3) is due to the superposition of the ice band and the band of liquid water, which is present in the sample in a certain percentage. Although two bands would be needed, in first approximation we decided to fit the acquired bands to

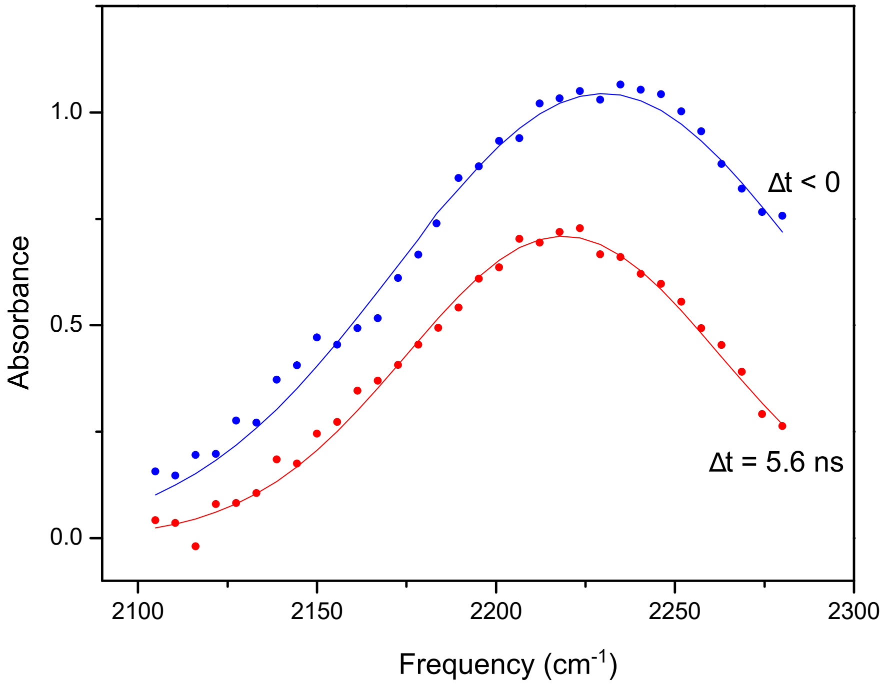

Figure 4.3: Experimental IR bands acquired by the TRIR setup at different delays (Δt < 0 ns in blue, Δt = 5.6 ns in red), subtracted of a constant value. The band acquired at Δt < 0 ns is typical of ice sample before the pump pulse, while the one acquired at Δt = 5.6 ns shows the system absorption band at 5.6 ns after the pump pulse. Dots indicate the experimental signal intensity detected by the 32 pixels of the MCT detector. The curves represent the fitting (Gaussian) functions.

one Gaussian function (blue and red curves in figure 4.3). This is motivated by the fact that we are first interested in the ice band evolution, and especially of its intensity, since it provides information on the ice quantity, and thus on the liquid one. The parameters obtained by the fit are the frequency of the band centre, the standard deviation (σ) and the intensity of the band.

In order to estimate the quantity of ice (and thus of melted ice) both the peak intensity or the integrated area, obtained by fitting the band with the Gaussian function, can be employed. Since both the parameters contain the information of the band variation due to melting, the intensity or the area can be reported as a function of Δt, allowing for the reconstruction of the dynamics. Despite the spectra having been stochastically acquired, the curve can be reconstructed. In fact the spectra are not acquired at increasing delay times but every spectrum is acquired after a certain delay time from a corresponding T-Jump pulse (for any experimental detail, see the paragraph *Sources synchronization* in 1.2.5 section). Each measurement involves a fresh sample, in fact, the repetition rate of 1 Hz at which the spectra are acquired has been chosen to allow the complete recrystallization of the sample. Two examples of curves, obtained by reporting the band intensity as a function of the delay time Δt, are shown in figures 4.4 and 4.5. Positive Δt values probe the melting process, $\Delta t = 0$ corresponds to a temporal overlap of the pump and the probe pulse describing the onset of the melting, and negative Δt values mean that the system is probed before the pump pulse arrival, corresponding to the ice sample not yet irradiated.

The evolution of the band intensity as a function of time can be described as follows. The initial constant level (before the time when the pump pulse is shot) is typical of the ice sample. A fast drop in the first nanoseconds after the pump pulse can be seen, and it is followed by a lower constant level, due to a certain portion of the melted ice. Such liquid, generated by the excitation, is in thermal equilibrium with ice at long delay times. The curve has been fitted to the sigmoid function as shown in figures 4.6 and 4.7 (zoom of figures 4.4 and 4.5 around the onset of melting, respectively). The sigmoid function has been chosen to take in account both the drop and the two levels (the initial level and the final one) characterizing our curves. Moreover, an exponential function has also been used to fit only the interval around the drop (sampled with few data points), and the fit returns the same time constant as the sigmoid. The result of the fit with the sigmoid function, which provides the time constant (τ) of the process, is also reported in the figures 4.6 and 4.7 with the calculated absorbance difference

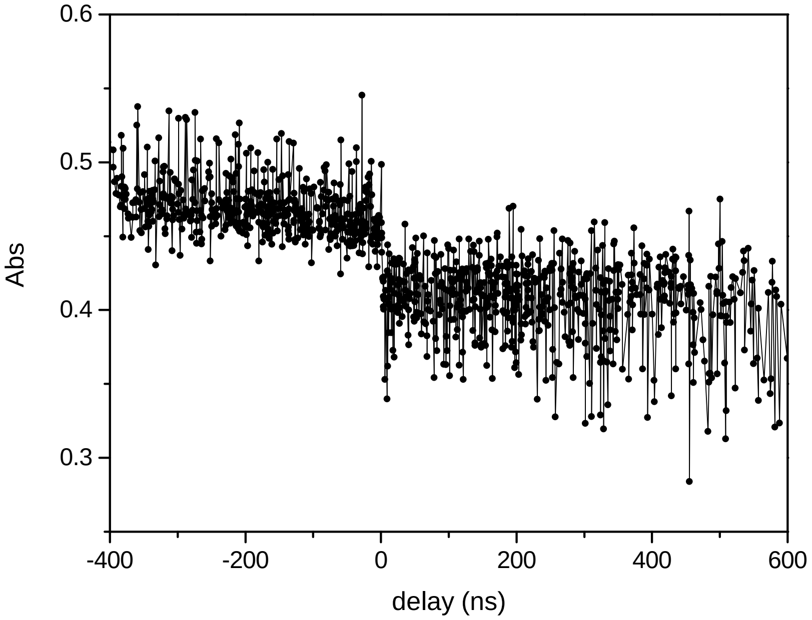

Figure 4.4: Example of our curve reconstructed by using the band intensity, resulting from the fit of 1000 measurements with Gaussian function, as a function of the delay time Δt. At negative delays the unperturbed ice sample is probed. No delay time between pump and probe pulses means the onset of the melting detection, and at positive values the melting process is probed.

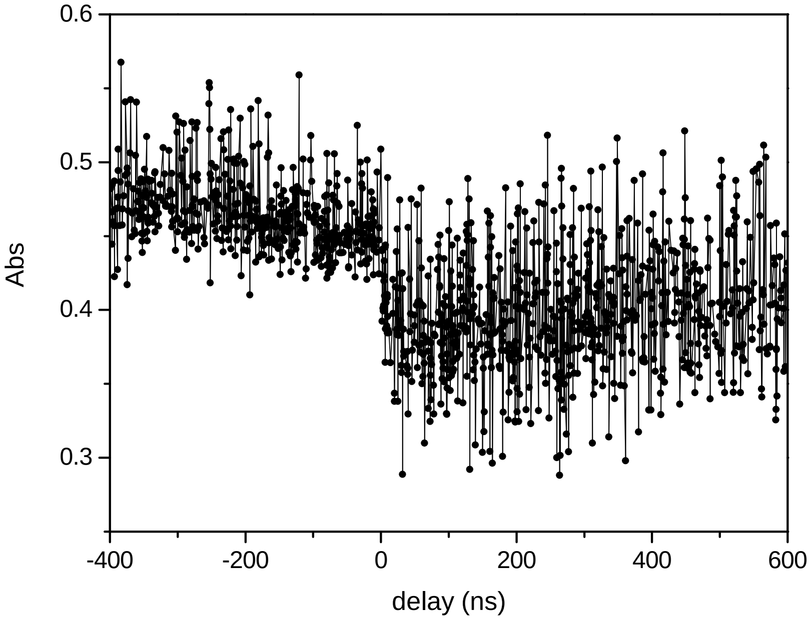

Figure 4.5: Another example of curve reconstructed by using the band intensity, resulting from the fit of 1000 measurements with Gaussian function, as a function of the delay time Δt. At negative delays the unperturbed ice sample is probed. No delay time between pump and probe pulses means the onset of the melting detection, and at positive values the melting process is probed.

(ΔA) between the initial and final levels and the corresponding melted portion (*fraction*).

In order to estimate the sample melted portion the absorbance difference (ΔA) of each curve is compared to the ice-liquid ΔA acquired at static conditions. The static absorbance values of the ice and the liquid sample in the IR spectrum region at around 2200 cm^{-1} have been acquired with the same setup in order to characterize the maximum ΔA that should be reached with the melting process in case of complete melting (liquid phase). The measured ice-liquid ΔA for a 50-μm-thick sample is 1.09, in good agreement with the ΔA of figure 4.1, where the spectra have been acquired by the FT-IR spectrometer. Thus, the ΔA values of the transient experiment provide a percentage of melt sample of $\sim$ 5-6%.

The absorbance variation can be well appreciated, even if the signal to noise ratio is close to 1. The high noise could be attributed to the presence of hot spots in the pump pulse. To increase the signal/noise ratio and validate our method, the quality of the pump beam must be improved. From the fit a time constant of the process of 3.2 $\pm$ 0.1 ns is obtained.

As can be seen in the curves shown so far, and especially in their zooms, the drop due to melting is shown to happen at Δt different to 0 ns, but this is due to the error we make in the determination of the delay Δt of the measurement, and represents just an offset.

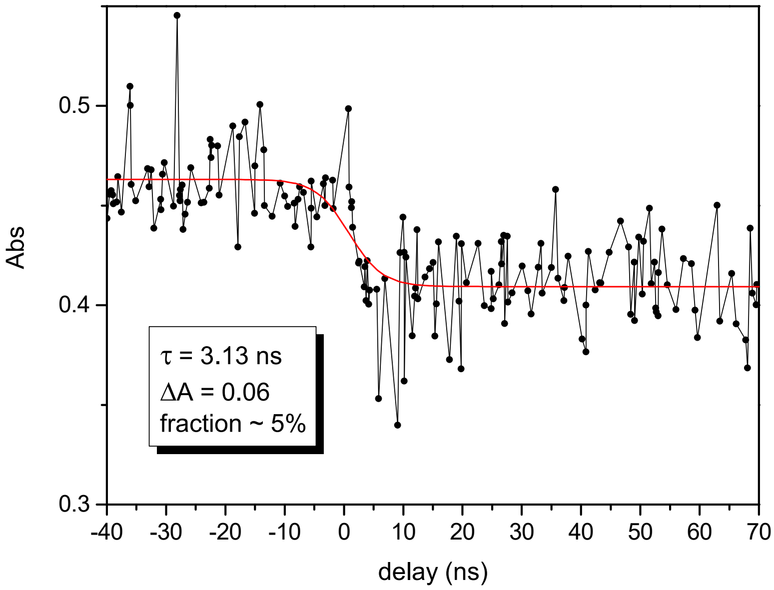

Figure 4.6: Fit with a sigmoid function (red line) of the curve of figure 4.4 (black dots and line). The obtained time constant (τ) of the process is 3.13 ns. The absorbance difference (ΔA) between the initial and final level is 0.06, resulting in a melting fraction (fraction) of about 5%.

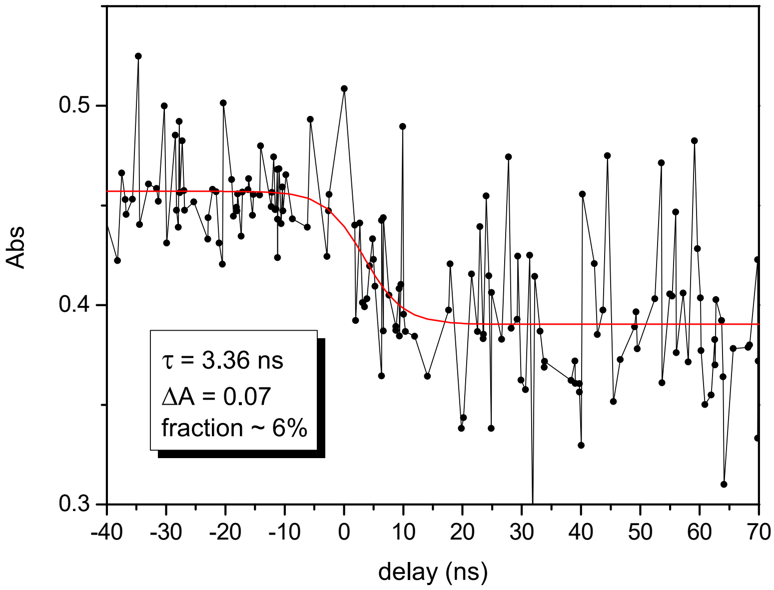

Figure 4.7: Fit with a sigmoid function (red line) of the curve of figure 4.5 (black dots and line). The obtained time constant (τ) of the process is 3.36 ns. The absorbance difference (ΔA) between the initial and final level is 0.07, resulting in a melting fraction (fraction) of about 6%.

4.3 Improvement of the experimental setup

In order to improve the quality of the pump beam, and to be sure to work with a beam with Gaussian characteristics, the experimental setup used to focus the pump beam on the sample, which is described in section 1.2.4, has been revised to decrease the beam diameter on the focal plane. A pinhole with an aperture of 3.4 mm in diameter has been placed on the beam coming out of the T-Jump source and the lens used to focus the beam on the sample (f = 500 mm) has been replaced with another one with focal length f = 200 mm. After these modifications, the beam diameter measured at 208 mm from the lens was 200 μm. By comparing this value with the beam diameter calculated for a Gaussian beam in the same conditions (λ = 1900 nm, distance from the lens, etc.) which is 201 μm, we can confirm that the beam has a Gaussian profile. With respect to the previous configuration, besides reducing the focal length we also modified the sample position which is now placed in the focal plane, whereas it was 50 mm far from the focus. This configuration allows to reduce the energy per pulse without changing the power density on the sample. In fact, to maintain on the focal plane the same power density per unit volume, a quarter of the previous energy (the maximum employed incident energy is $\sim$ 9 mJ/pulse), which is $\sim$ 2.3 mJ/pulse, has been sent to the sample. The factor ($\frac{1}{4}$) is obtained by the ratio between the previous volume and the new one. Thus, the energy absorbed by the sample remained unchanged, being equal to the one characterizing the TRIR experiment before the setup improvement. It is also equal to the maximum absorbed energy related to the Mie scattering experiment. Therefore, the conditions to reach a complete melting of ice at thermodynamic equilibrium are still guaranteed.

4.3.1 Results

Examples of the evolution in time of the probed band intensity in the spectral region accessed by our detection system obtained after the setup improvement are shown in Figs.4.8 and 4.9. As can be seen in the upper panels of Figs.4.8 and 4.9, the absorbance variation after the T-Jump pulse is extremely clear in spite of a slightly larger uncertainty on the absorbance values. These curves have been fitted to the sigmoid function as shown in the lower panels of figures 4.8 and 4.9, where the result of the fit and the melted portion are also reported.

The new results, compared to the previous ones, show a slightly shorter

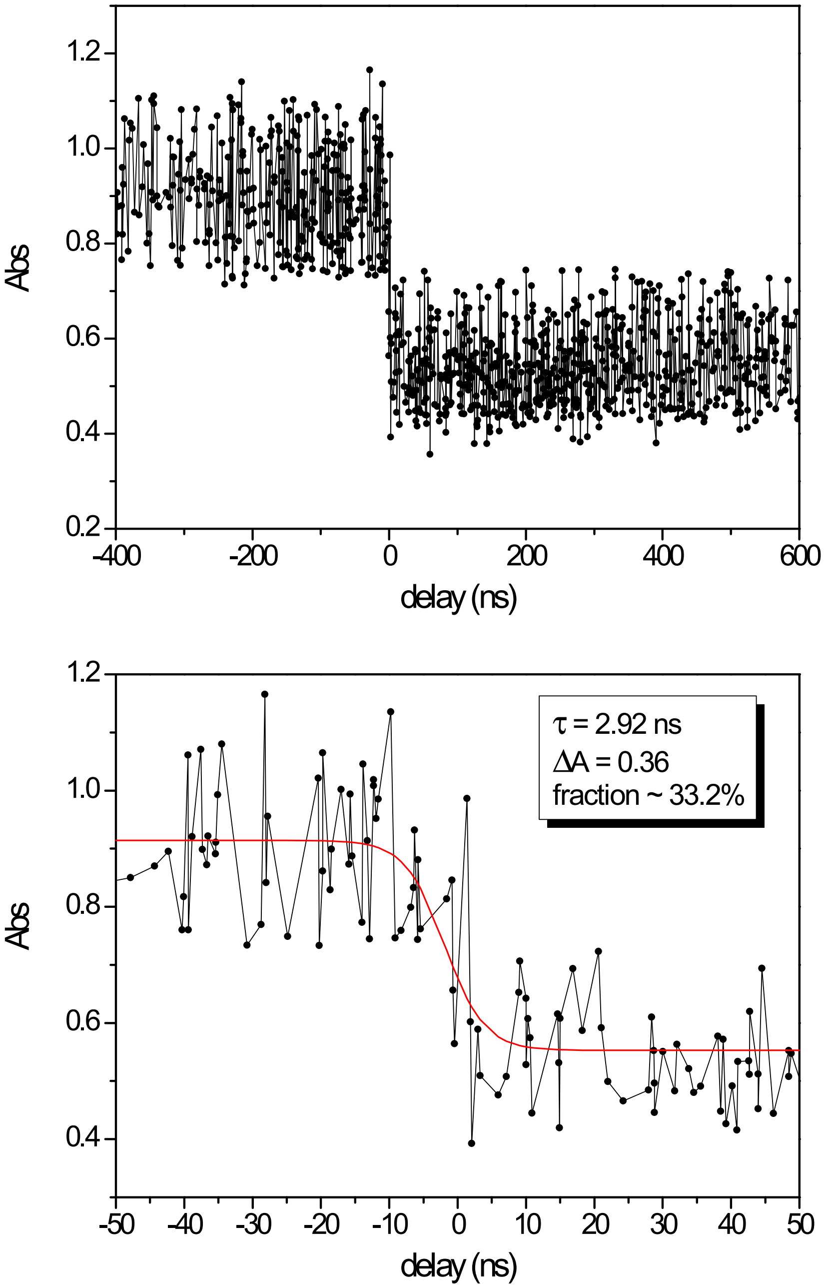

Figure 4.8: (Upper) Example of the curve reconstructed by using the band intensity, resulting from the fit of 1000 measurements with the Gaussian function, as a function of the delay time Δt. The spectra have been acquired after the setup improvement. (Lower) Fit with sigmoid function (red line) of the portion of the above curve around the zero delay (black dots and line). The obtained time constant (τ) of the process is 2.92 ns. The absorbance difference (ΔA) between the initial and final level is 0.36, resulting in a melting fraction of $\sim$ 33.2%.

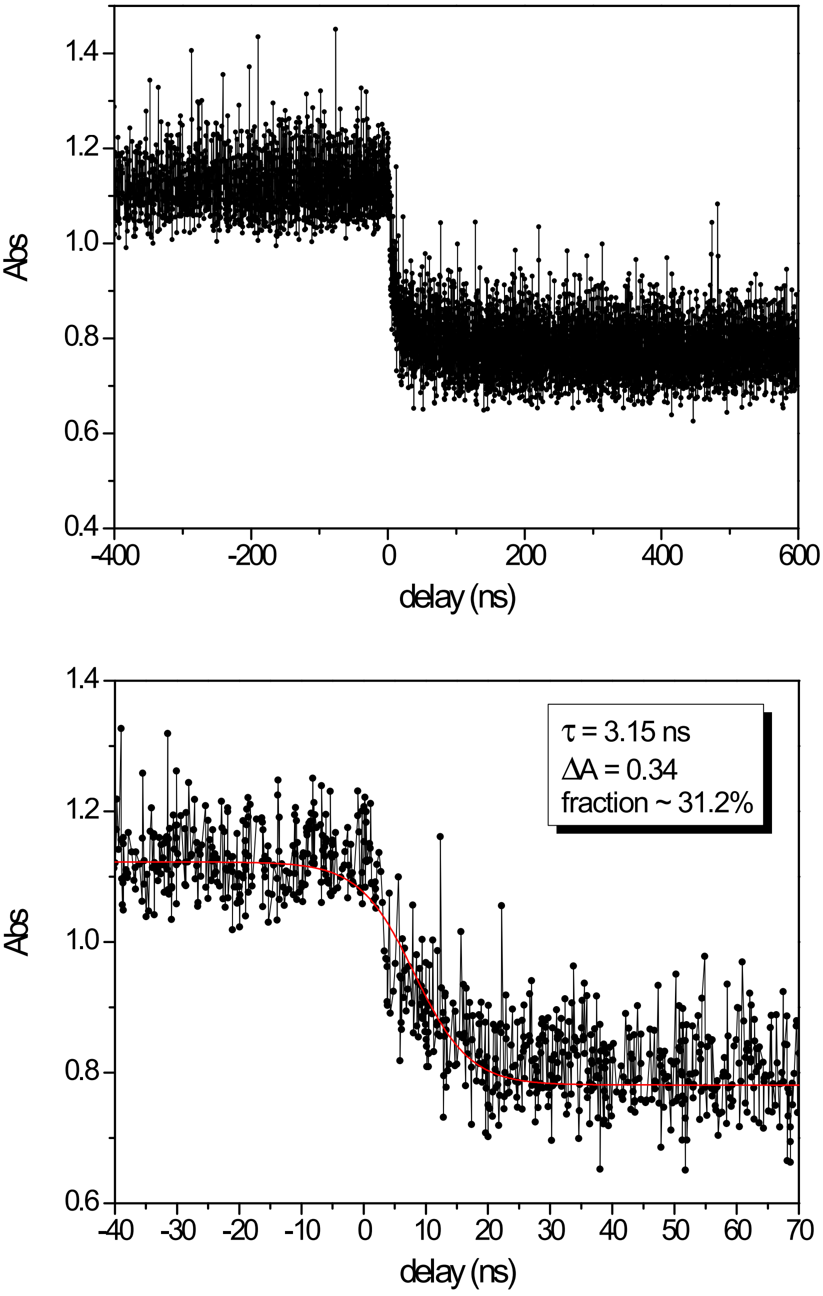

Figure 4.9: (Upper) Example of the curve reconstructed by using the band intensity, resulting from the fit of 10000 measurements with the Gaussian function, as a function of the delay time Δt. The spectra have been acquired after the setup improvement. (Lower) Fit with sigmoid function (red line) of the portion of the above curve around the zero delay (black dots and line). The obtained time constant (τ) of the process is 3.15 ns. The absorbance difference (ΔA) between the initial and final level is 0.34, resulting in a melting fraction of $\sim$ 31.2%.

time constant (τ = 3.0 ± 0.1 ns) of the process and a significant increase of the melting fraction, which is 31.2–33.2%. The larger fraction of melt is the reason of the better signal/noise ratio (the error of absorbance measurement is ± 0.1) after the beam quality improvement. The obtained molten fraction values are in good agreement with the previous work [31] which reports a value of 33%, that therefore appears as a kind of intrinsic limit of this approach.

Instead of the peak intensity, we have also plotted the time evolution of the band area. As can be seen in the curve of figure 4.10, the time constant (τ = 3.2 ns) nicely agrees with that obtained using the intensity.

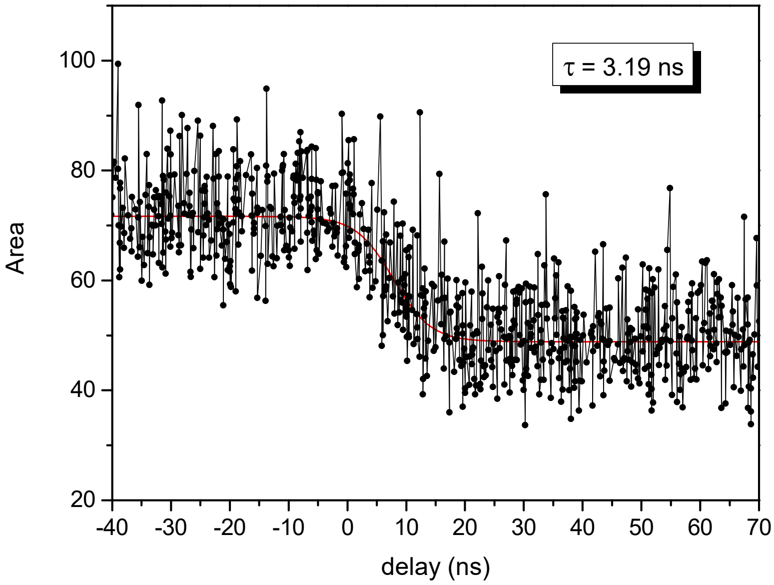

Figure 4.10: Fit with sigmoid function (red line) of the curve (black dots and line) obtained by reporting the area as a function of delay time Δt. The obtained time constant (τ) of the process is 3.19 ns.

Interestingly, the frequency of the band centre (other fit parameter of the IR band at 2200 cm^{-1}) reported as a function of delay time Δt has an intriguing behavior (see figure 4.11). The initial constant level is typical of the ice sample, as for the case of the curve construction using the intensity or the area, then a 200-ps-long drop occurs, comparable to the temporal resolution (100 ps), therefore much faster than those observed in the peak intensity and the area evolution with time. Since the bands around 2200 cm^{-1} acquired at different delays are due to the superposition of the ice and the liquid water bands, they should be fitted by two bands. However, this is not possible because the frequency window accessed by our detector (MCT) prevents the full analysis of both bands. By using only one band for the fit we describe the behavior of the centre of mass of the system which

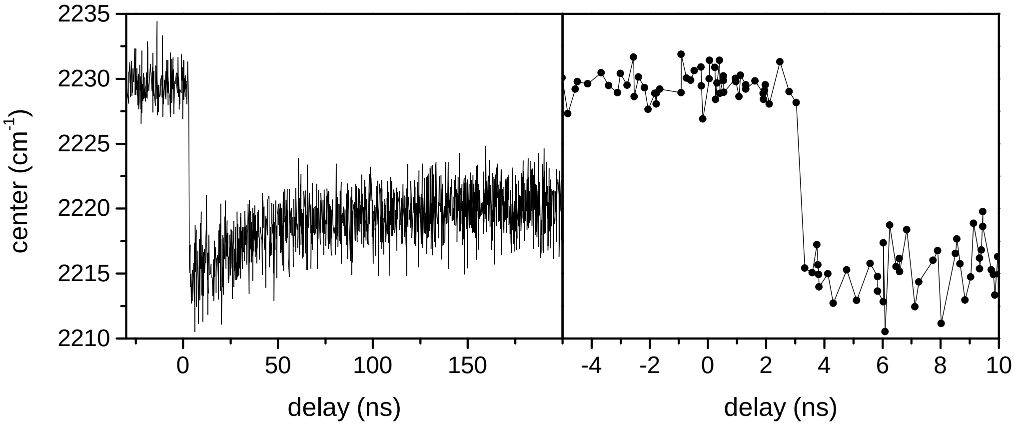

Figure 4.11: Curve obtained by reporting the frequency of the band centre as a function of the delay time Δt (left). Zoom of the same curve in the first nanoseconds (right).

nicely accounts for the dynamics of the process.

By comparing the band frequency evolution to the band intensity one (describing the absorbance changes in the irradiated sample) as a function of the delay time Δt, both the evolutions are well characterized by our method, revealing different phenomena and characteristic times. The time required for the frequency and for the intensity to reach a constant level of values is about 80 ns and 3 ns, respectively. In the last spectrum acquired before the frequency drop (figure 4.11), the frequency and the intensity are typical of ice, while in the first spectrum acquired after the drop, the frequency is typical of the liquid and the intensity of ice. In other words, during melting the band immediately shifts at lower frequency and later it decreases its intensity, revealing, in first approximation, the presence of two phenomena with different evolutions and different time constants. The different behavior of the frequency and the intensity suggests a complex evolution of the melting process. The sudden change of the frequency is indeed ascribable to the librational component of the examined combination mode (due to bending and librations). In fact, the frequency of the librational mode changes from 800 cm^{-1} in ice I$_h$ to about 680 cm^{-1} after melting [86], while the bending mode is around 1650 cm^{-1} both in ice I$_h$ [87] and in liquid water [88]. The intensity decrease is instead the signature of the fluid because only the “free” diffusion (and rotation) of molecules is responsible for the broadening and for the partial, statistical, cancellation of the transition dipoles which determines the intensity decrease.

The transient structure characterizing the superheated state can be speculated to derive from the partial or complete disruption of the H-bond network. The features of this metastable state depend on whether the energy supplied to the system is sufficient to break also the translational symmetry. In this case the long-range order of the crystal structure is lost and an amorphous solid would characterize the superheated state, otherwise a plastic crystal phase would account.

It can be thus speculated that the loss of the translational symmetry, crystal long-range order, occurs within our experimental resolution on the same time scale of the vibrational relaxation, giving rise to a kind of amorphous ice. A time-resolved X-ray diffraction experiment [89] reported a similar conclusion showing, after rapid decompression, the transformation of a high-pressure ice phase into a low-density amorphous ice.

Otherwise, the supplied energy causes the system to break the hydrogen bond network and, thus, to lose only its rotational order. In such case the oxygens remain in the mass centers, leading to the formation of a crystalline plastic phase, i.e. an ice phase with freely rotating molecules, as predicted to occur close to the melting line by several simulations [90–92].

Therefore, from our results can be envisaged a two-step mechanism of melting: a very fast process occurring on a time scale shorter than 200 ps that leads to the destruction of the rotational order of the crystal (or, even, of the long-range order of the crystal), and a slower process ($\sim$3 ns) where the melting effectively occurs and the crystalline plastic phase (or the amorphous ice) transforms to the liquid.

4.4 Conclusion

In this chapter we have described how the T-Jump technique and the transient infrared absorption spectroscopy have been successfully coupled to follow the changes of an IR vibrational band of water during the phase transition.

The energy release by the T-Jump to a vibrational combination band of water and the thermal redistribution occur within the duration of our pump pulse, ensuring the super-heating of the system already after $\sim$ 15 ps [5]. The water vibrational band monitored by the IR probe is due to the combination of water bending and librational modes. This band, in fact, has been chosen as probe for the melting process, and it is common to ices and clathrate hydrates, paving the way to dynamics investigations of the argon and other clathrates, as future perspective of this thesis work.

The possibility to directly quantify by this method the melted sample portion as a function of time has confirmed the intrinsic limit to the ice melting: the maximum fraction of the probed ice volume that can be melted is about 33%, and it is reached in $\sim$3 ns. Such time constant ($\tau \sim$3 ns) is in excellent agreement with the time constant τ_1 obtained by the Mie scattering experiment in the same T-Jump energy condition, that is the maximum energy absorbed by the sample. In the Mie scattering experiment, in fact, the time constant τ_1 corresponds to the scattering at the ice/melt interfaces inside the sample, and it becomes shorter and shorter as the energy increases until a minimum value of few nanoseconds. This trend seems to tend to a limit, a constant value around 5 ns, comparable to the resolution allowed by the used photodiode, and thus not allowing to completely resolve the process kinetics. The access to a shorter delay time between the pump and the probe pulses allowed by the new TRIR experiment allows to validate the approximation made to obtain that value by the Mie scattering technique. Such access also allows to affirm that τ_1 tends to a constant value at the highest employed T-Jump energy, which corresponds to the time needed to achieve the intrinsic limit to the ice melting. The value (33%) is in excellent agreement with a previous work [31] on ice I_h which exploits a different method to pump and to probe the system respect to our experiment. Moreover, the time window investigated with the present TRIR experiment, which goes from 100 ps after the pump pulse up to $\sim$1 μs, is well connected to the time window under investigation with the Mie scattering technique (first nanoseconds of the process to tens of milliseconds). This allows to investigate the dynamics of the melting process on a wide time window starting from 100 ps after the perturbation (T-Jump) to the end of the process (complete recrystallization).

The results here reported provide new elements concerning a possible melting mechanism involving the role of the librations (probed band) during the phase transition of the crystalline ice sample. The melting appears, in fact, as a two-step process where a fast ($\leq$200 ps) destruction of rotational or long-range order of the crystal takes place and likely produces a plastic phase or an amorphous solid followed by the slower ($\sim$3 ns) formation of the liquid. Importantly, this information nicely completes and connects to the following growth of the melt particles identified by the Mie scattering technique.

Conclusion

Up to now the melting mechanisms on a sub-microscopic scale have been addressed by many experimental and theoretical works which cover a sub-nanosecond time window. However, these works are unable to unveil the entire system dynamics. On the other hand, macroscopic observations of phase transitions, such as the freezing process, take place in a milliseconds time scale and account for processes occurring at surfaces and limited in time by thermal exchange with the environment. The connection between these two time windows is difficult to achieve both through experimental and theoretical techniques, and it is still completely unexplored. This thesis, describing an investigation on melting dynamics in ices, is placed within this scenario. In this study, in fact, the gap between these two time windows has been covered.

In order to study the dynamics of melting, a perturbation faster than the dynamics under investigation is a fundamental requirement. For this reason, an ultrafast thermal jump has been used to change very rapidly (on a picoseconds time scale) the temperature of a 50-μm-thick ice sample and to induce the phase transition. Such thermal jump is realized by an energetic picosecond infrared laser pulse (pump) resonant with a combination band of ice. The pump pulse is absorbed by ice, inducing the heating of the crystalline sample above its melting temperature (up to $\sim$400 K) and generating a superheated lattice. Melt nuclei form inside such superheated lattice within the first nanosecond [31] after the pump pulse and grow over the time. The dynamics of the melting process has been probed through two different kind of time-resolved spectroscopic techniques, whose coupling to the T-Jump method has been specifically developed in this thesis: the *Mie scattering* and the *transient infrared* absorption spectroscopy.

The *Mie scattering* spectroscopy allows to follow the dimensional evolution of the molten domains inside the superheated crystal lattice from the first nanoseconds ($\sim$3 ns) after the heating pulse, where an already nucleated sample is found. The scattering at the melt/ice interfaces has been monitored in time by using a continuous-wave probe laser. The melting dynamics of ices have been experimentally investigated within the entire mesoscopic regime from the first nanoseconds after the melting onset to the complete recrystallization of the sample, which takes place in tens of milliseconds, by combining the Thermal-Jump technique and the time-resolved Mie scattering spectroscopy [40]. By this experiment three dynamical regimes have been identified: The growth of molten domains (fast process), the coalescence (intermediate regime) and the recrystallization (slow process). The molten domains, approximated to spheres, reach the maximum size (diameter$\sim$400 nm) in $\sim$200 ns. Then, they start to merge each other (coalescence) on a microseconds time window until the average diameter achieves $\sim$1.5 μm, when the recrystallization takes place. The ice reformation is complete in tens of milliseconds, depending on the heat diffusion to the environment. The experiment reveals a melting of the bulk ice sample which is not instantaneous (up to the microseconds time scale). The order of magnitude of the characteristic time of the melting process is larger than that expected for simple H-bond structures.

In order to include the dynamics investigation of complex structures, such as clathrate hydrates, the characterization through FTIR and Raman spectroscopy of clathrate hydrate samples has been performed. The recrystallization from the melt has been investigated being a prerequisite for dynamics investigations with pump-probe techniques. An homogeneous sample is also a fundamental requirement to investigate the melting dynamics of clathrate, thus the development of a technique to synthesize clathrate hydrates and a loading procedure in the diamond or sapphire anvil cell has been necessary. The Mie scattering technique cannot be used for studying the crystallization of these hydrates because of the impossibility to distinguish the species under investigation (ice or hydrate). Since the IR spectra of the hydrate and the unmixed components are considerably different, the hydrate phase evolution can be detected as a function of time by using transient IR spectroscopy, thus allowing a fine characterization of the melting dynamics. The same considerations hold for water, which shows different IR absorption spectra for the solid and the liquid phase.

In order to access the first nanosecond after the pump pulse, the T-Jump technique has been coupled to the *transient infrared* (TRIR) absorption spectroscopy.

In this experiment the ice melting is monitored in time by probing the combination band of water corresponding to bending and librational modes. This experiment allows to access the temporal window going from 100 ps after the pump pulse to about 1 μs, allowing the investigation of melting dynamics at shorter delay times compared to Mie scattering experiments. The melted sample portion as a function of time has been directly quantified, revealing that the maximum fraction of the probed ice volume that can be melted is about 33%, and it is reached in $\sim$ 3 ns. Such time constant ($\tau \sim$3 ns), corresponding to the melting process, is in excellent agreement with the time constant τ_1 obtained by the Mie scattering experiment in the same T-Jump energy condition, that is the maximum energy absorbed by the sample. In the Mie scattering experiment the time constant τ_1 corresponds to the behavior of the scattering at the ice/melt interfaces inside the sample as a function of the absorbed energy. The time constant τ_1 decreases by increasing the energy absorbed by the sample until a minimum value of few nanoseconds: It spans five orders of magnitude ranging from 15000 to about 5 ns. This trend seems to tend to a limit, a constant value around 5 ns, which is the resolution allowed by the used photodiode, and thus not allowing to completely resolve the process kinetics. The new TRIR experiment instead allows to follow the melting process, i.e. the transition from ice to liquid, by the direct quantification of the melt in time. The access to a shorter delay time between the pump and the probe pulses by the new TRIR experiment allows to validate the approximation made to obtain that value (5 ns) by the Mie scattering technique, and also to affirm that τ_1 tends to a constant value at the highest employed T-Jump energy, which corresponds to the time needed to achieve the intrinsic limit to the ice melting ($\sim$ 33%).

The two techniques therefore provide the full melting dynamics from 100 ps after the pump excitation (T-Jump) to tens of milliseconds, from the beginning of melting to recrystallization in bulk water ice samples, allowing to experimentally connect for the first time the short and the long time scales. The picture resulting from this study envisages the superheating of the crystal on a time scale comparable to the pulse duration (15 ps) accompanied by the simultaneous or slightly slower ($\leq$ 100 ps) destruction of the rotational order of the crystal or, even, of the crystal structure itself without the melting of the sample. The melting, in fact, occurs on longer time scales being achieved in a time interval of few nanoseconds ($\tau \sim$ 3 ns). The nuclei evolve until the coalescence takes place in a time window strictly depending on the nuclei concentration (pulse energy), the parameter that should be carefully considered to interpret the scattering data. Microseconds after the pulse the system is completely thermalized, and the cooling and the corresponding decrease of the melt drops is entirely regulated by thermal diffusion to the sink.

For the first time the full dynamics of the melting process of an archetypal crystal, ice, has been followed from the first hundreds of picoseconds after the energy for the homogeneous nucleation of the fluid phase has been delivered, up to the crystal reformation, which occurs tens of milliseconds later. The mechanisms regulating the melting as well as the following evolution have been identified and temporally located. These approaches can be immediately extended to the study of more complex systems such as clathrate hydrates and other, high pressure, ice phases. This could help to establish a correlation between the structural arrangement, the strength of the intermolecular interaction, the presence of H-bonds and the melting dynamics. Much more complicated appears the study of the crystallization process which motivated this research. In fact, the only partial melting of the sample prevents the possibility to study the nucleation and growth of the crystalline phase, which is always present in the sample.

Bibliography

[1] S. Bauerecker, P. Ulbig, V. Buch, L. Vrbka, and P. Jungwirth. Monitoring ice nucleation in pure and salty water via high-speed imaging and computer simulations. *Journal of Physical Chemistry C* **112**, 7631 (2008). 7, 48

[2] B. Murray, S. Broadley, T. Wilson, S. Bull, R. Wills, H. Christenson, and E. Murray. Kinetics of the homogeneous freezing of water. *Physical Chemistry Chemical Physics* **12**, 10380 (2010). 7, 48

[3] B. Siwick, J. Dwyer, R. Jordan, and R. Miller. An atomic-level view of melting using femtosecond electron diffraction. *Science* **302**, 1382 (2003). 7, 47

[4] P. Musumeci, J. T. Moody, C. M. Scoby, M. S. Gutierrez, and M. Westfall. Laser-induced melting of a single crystal gold sample by time-resolved ultrafast relativistic electron diffraction. *Applied Physics Letters* **97**, 063502 (2010). 47

[5] H. Iglev, M. Schmeisser, K. Simeonidis, A. Thaller, and A. Laubereau. Ultrafast superheating and melting of bulk ice. *Nature* **439**, 183 (2006). 7, 12, 17, 47, 49, 65, 72, 81, 110, 124

[6] M. Forsblom and G. Grimvall. How superheated crystals melt. *Nature Materials* **4**, 388 (2005). 8

[7] A. Samanta, M. E. Tuckerman, T.-Q. Yu, and W. E. Microscopic mechanisms of equilibrium melting of a solid. *Science* **346**, 729 (2014). 8, 47

[8] V. Schettino, R. Bini, M. Ceppatelli, L. Ciabini, and M. Citroni. *Chemical Reactions at Very High Pressure*. John Wiley & Sons, Inc. (2005). 8

[9] W. J. Evans, C. S. Yoo, G. W. Lee, H. Cynn, M. J. Lipp, and K. Visbeck. Dynamic diamond anvil cell (dDAC): A novel device for studying the dynamic-pressure properties of materials. *Review of Scientific Instruments* **78**, 073904 (2007). 8

[10] G. W. Lee, W. J. Evans, and C. S. Yoo. Dynamic pressure-induced dendritic and shock crystal growth of ice VI. *Proceedings of the National Academy of Sciences of the United States of America* **104**, 9178 (2007). 9, 48

[11] G. W. Lee, W. J. Evans, and C. S. Yoo. Crystallization of water in a dynamic diamond-anvil cell: Evidence for ice VII-like local order in supercompressed water. *Physical Review B* **74**, 134112 (2006). 9

[12] J. Y. Chen and C. S. Yoo. Formation and phase transitions of methane hydrates under dynamic loadings: Compression rate dependent kinetics. *Journal of Chemical Physics* **136**, 114513 (2012). 9, 44, 48, 88

[13] D. Dolan, M. Knudson, C. Hall, and C. Deeney. A metastable limit for compressed liquid water. *Nature Physics* **3**, 339 (2007). 9

[14] D. Milathianaki, S. Boutet, G. Williams, A. Higginbotham, D. Ratner, A. Gleason, M. Messerschmidt, M. Seibert, D. Swift, P. Hering, J. Robinson, W. White, and J. Wark. Femtosecond visualization of lattice dynamics in shock-compressed matter. *Science* **342**, 220 (2013).

[15] S. Anzellini, A. Dewaele, M. Mezouar, P. Loubeyre, and G. Morard. Melting of iron at Earth's inner core boundary based on fast X-ray diffraction. *Science* **340**, 464 (2013).

[16] M. Gorman, R. Briggs, E. McBride, A. Higginbotham, B. Arnold, J. Eggert, D. Fratanduono, E. Galtier, A. Lazicki, H. Lee, H. Liermann, B. Nagler, A. Rothkirch, R. Smith, D. Swift, G. Collins, J. Wark, and M. McMahon. Direct observation of melting in shock-compressed bismuth with femtosecond X-ray diffraction. *Phisical Review Letters* **115**, 095701 (2015). 9

[17] A. E. Gleason, C. A. Bolme, H. J. Lee, B. Nagler, E. Galtier, D. Milathianaki, J. Hawreliak, R. G. Kraus, J. H. Eggert, D. E. Fratanduono, G. W. Collins, R. Sandberg, W. Yang, and W. L. Mao. Ultrafast visualization of crystallization and grain growth in shock-compressed SiO_2. *Nature Communications* **6**, 8191 (2015).

[18] R. Briggs, M. G. Gorman, A. L. Coleman, R. S. McWilliams, E. E. McBride, D. McGonegle, J. S. Wark, L. Peacock, S. Rothman, S. G. Macleod, C. A. Bolme, A. E. Gleason, G. W. Collins, J. H. Eggert, D. E. Fratanduono, R. F. Smith, E. Galtier, E. Granados, H. J. Lee, B. Nagler, I. Nam, Z. Xing, and M. I. McMahon. Ultrafast X-ray diffraction studies of the phase transitions and equation of state of scandium shock compressed to 82 GPa. *Phisical Review Letters* **118**, 025501 (2017). 9

[19] M. Millot, S. Hamel, J. Rygg, P. M. Celliers, G. Collins, F. Coppari, D. Fratanduono, R. Jeanloz, D. Swift, and J. Eggert. Experimental evidence for superionic water ice using shock compression. *Nature Physics* **14**, 297 (2018). 9

[20] M. Citroni, S. Fanetti, B. Guigue, P. Bartolini, A. Taschin, A. Lapini, P. Foggi, and R. Bini. Picosecond optical parametric generator and amplifier for large temperature-jump. *Optics Express* **22**, 30047 (2014). 10, 23, 80

[21] P. Wernet, G. Gavrila, K. Godehusen, C. Weniger, E. Nibbering, T. Elsaesser, and W. Eberhardt. Ultrafast temperature jump in liquid water studied by a novel infrared pump-X-ray probe technique. *Applied Physics A-Materials Science & Processing* **92**, 511 (2008). 10, 15

[22] Q. Mei and K. Lu. Melting and superheating of crystalline solids: From bulk to nanocrystals. *Progress in Materials Science* **52**, 1175 (2007). 10, 47

[23] R. Ludwig. Water: From clusters to the bulk. *Angewandte Chemie-International Edition* **40**, 1808 (2001). 10

[24] G. Malenkov. Liquid water and ices: understanding the structure and physical properties. *Journal of Physics-Condensed Matter* **21** (2009). 10

[25] R. Dyer, F. Gai, and W. Woodruff. Infrared studies of fast events in protein folding. *Accounts of Chemical Research* **31**, 709 (1998). 15

[26] J. Chen, D. Rempel, and M. Gross. Temperature jump and fast photochemical oxidation probe submillisecond protein folding. *Journal of the American Chemical Society* **132**, 15502 (2010).

[27] O. Mohammed, G. Jas, M. Lin, and A. Zewail. Primary peptide folding dynamics observed with ultrafast temperature jump. *Angewandte Chemie-International Edition* **48**, 5628 (2009). 15, 17

[28] S. Chen, I. Lee, W. Tolbert, X. Wen, and D. Dlott. Applications of ultrafast temperature jump spectroscopy to condensed phase molecular-dynamics. *Journal of Physical Chemistry* **96**, 7178 (1992). 15

[29] H. R. Ma, C. Z. Wan, and A. H. Zewail. Ultrafast T-jump in water: studies of conformation and reaction dynamics at the thermal limit. *Journal of the American Chemical Society* **128**, 6338 (2006). 16

[30] A. Millo, Y. Raichlin, and A. Katzir. Mid-infrared fiber-optic attenuated total reflection spectroscopy of the solid-liquid phase transition of water. *Appl. Spectroscopy* **59**, 460 (2005). 17

[31] M. Schmeisser, H. Iglev, and A. Laubereau. Bulk melting of ice at the limit of superheating. *Journal of Physical Chemistry B* **111**, 11271 (2007). 18, 47, 49, 65, 72, 80, 81, 110, 121, 124, 127

[32] M. Schmeisser, H. Iglev, and A. Laubereau. Maximum superheating of bulk ice. *Chemical Physics Letters* **442**, 171 (2007). 18, 47

[33] M. Schmeisser, A. Thaller, H. Iglev, and A. Laubereau. Picosecond temperature and pressure jumps in ice. *New Journal of Physics* **8** (2006).

[34] H. Iglev and M. Schmeisser. Ultrafast IR spectroscopy of ice-water phase transition. *Journal of Molecular Liquids* **154**, 14 (2010). 18, 47, 49

[35] C. M. Phillips, Y. Mizutani, and R. M. Hochstrasser. Ultrafast thermally induced unfolding of RNase A. *Proceedings of the National Academy of Sciences of the United States of America* **92**, 7292 (1995). 18

[36] V. Tchijov. Heat capacity of high-pressure ice polymorphs. *Journal of Physics and Chemistry of Solids* **65**, 851 (2004). 19

[37] L. Bezacier, B. Journaux, J. P. Perrillat, H. Cardon, M. Hanfland, and I. Daniel. Equations of state of ice VI and ice VII at high pressure and high temperature. *Journal of Chemical Physics* **141**, 104505 (2014). 19

[38] H. PV. *Ice Physics*. Oxford University Press, Oxford, UK (2010). 19

[39] R. Bini, R. Ballerini, G. Pratesi, and H. Jodl. Experimental setup for Fourier transform infrared spectroscopy studies in condensed matter at high pressure and low temperatures. *Rev. Sci. Instrum.* **68**, 3154 (1997). 20

[40] M. Citroni, S. Fanetti, N. Falsini, P. Foggi, and R. Bini. Melting dynamics of ice in the mesoscopic regime. *Proceedings of the National Academy of Sciences of the United States of America* **114**, 5935 (2017). 26, 48, 80, 128

[41] K. Syassen. Ruby under pressure. *High Pressure Research* **28**, 75 (2008). 29, 39

[42] R. Kaindl, M. Wurm, K. Reimann, P. Hamm, A. Weiner, and M. Woerner. Generation, shaping, and characterization of intense femtosecond pulses tunable from 3 to 20 μm. *Journal of the Optical Society of America B - Optical Physics* **17**, 2086 (2000). 34

[43] A. Ruoff, H. Xia, and Q. Xia. The effect of a tapered aperture on X-ray diffraction from a sample with a pressure gradient: studies on three samples with a maximum pressure of 560 GPa. *Rev. Sci. Instrum.* **63**, 4342 (1992). 39

[44] J. W. Shaner, H. K. Mao, P. M. Bell, and D. J. Steinberg. Specific volume measurements of Cu, Mo, Pd, and Ag and calibration of the ruby R1 fluorescence pressure gauge from 0.06 to 1 Mbar. *J. Appl. Phys.* **49**, 3276 (1978). 39

[45] G. Piermarini and S. Block. Ultrahigh pressure diamond-anvil cell and several semiconductor phase transition pressures in relation to the fixed point pressure scale. *Rev. Sci. Instrum.* **46**, 973 (1975). 39

[46] M. Max. *Natural Gas Hydrate, in Oceanic and Permafrost Environments*. Kluwer Publ. (2000). 43

[47] A. Y. Manakov, V. I. Voronin, A. V. Kurnosov, A. E. Teplykh, V. Y. Komarov, and Y. A. Dyadin. Structural investigations of argon hydrates at pressures

up to 10 kbar. *Journal of Inclusion Phenomena and Macrocyclic Chemistry* **48**, 11 (2004). 44, 100

[48] P. Atkins and J. De Paula. *Atkins' Physical Chemistry*. Oxford University Press, Oxford, UK, 8th ed. (2006). 45

[49] M. Matsumoto, S. Saito, and I. Ohmine. Molecular dynamics simulation of the ice nucleation and growth process leading to water freezing. *Nature* **416**, 409 (2002). 45

[50] O. Mishima, L. Calvert, and E. Whalley. 'Melting ice' I at 77 K and 10 kbar: a new method of making amorphous solids. *Nature* **310**, 393 (1984). 46

[51] O. Mishima, L. Calvert, and E. Whalley. An apparently 1st-order transition between two amorphous phases of ice induced by pressure. *Nature* **314**, 76 (1985).

[52] O. Mishima. Reversible 1st-order transition between 2H_2O amorphs at similar-to-0.2 GPa and similar-to-135-K. *Journal of Chemical Physics* **100**, 5910 (1994).

[53] T. Loerting, K. Winkel, M. Seidl, M. Bauer, C. Mitterdorfer, P. Handle, C. Salzmann, E. Mayer, J. Finney, and D. Bowron. How many amorphous ices are there?. *Phys. Chem. Chem. Phys.* **13**, 8783 (2011). 46

[54] R. J. Speedy. Stability-limit conjecture. An interpretation of the properties of water. *The Journal of Physical Chemistry* **86**, 982 (1982). 46

[55] F. Prielmeier, E. Lang, R. Speedy, and H. Lüdemann. Diffusion in supercooled water to 300 MPa. *Phys. Rev. Lett.* **59**, 1128 (1987). 46

[56] S. Fanetti, M. Pagliai, M. Citroni, A. Lapini, S. Scandolo, R. Righini, and R. Bini. Connecting the water phase diagram to the metastable domain: High-pressure studies in the supercooled regime. *Journal of Physical Chemistry Letters* **5**, 3804 (2014). 46

[57] C. Stan, G. Schneider, S. Shevkoplyas, M. Hashimoto, M. Ibanescu, B. Wiley, and G. Whitesides. A microfluidic apparatus for the study of ice nucleation in supercooled water drops. *Lab on a chip* **9**, 2293 (2009). 46

[58] C. Caleman and D. van der Spoel. Picosecond melting of ice by an infrared laser pulse: A simulation study. *Angewandte Chemie-International Edition* **47**, 1417 (2008). 47, 49, 81

[59] R. G. Pereyra, I. Szleifer, and M. A. Carignano. Temperature dependence of ice critical nucleus size. *Journal of Chemical Physics* **135**, 034508 (2011). 48

[60] Z. Ge, D. Cahill, and P. Braun. Thermal conductance of hydrophilic and hydrophobic interfaces. *Phys. Rev. Lett.* **96**, 186101 (2006). 52

[61] B. Chen, W.-P. Hsieh, D. G. Cahill, D. R. Trinkle, and J. L. Thermal conductivity of compressed H_2O to 22 GPa: A test of the leibfried-schlomann equation. *Physical Review B-Condensed Matter* **83**, 132301 (2011). 52

[62] C. Bohren and D. Huffman. *Absorption and scattering of light by small particles*. John Wiley and Sons, New York (1983). 59, 60, 81

[63] E. Sloan and C. Koh. *Clathrate hydrates of Natural Gases*. CRC Press, New York, 3rd ed. (2007). 83, 84, 86

[64] W. Mao, C. Koh, and E. Sloan. Clathrate, hydrates under pressure. *Physics Today* **60**, 42 (2007). 83

[65] E. Suess, G. Bohrmann, J. Greinert, and E. Lausch. Flammable ice. *Scientific American* **281**, 76 (1999). 84

[66] P. Warrier, M. N. Khan, V. Srivastava, C. M. Maupin, and C. A. Koh. Overview: Nucleation of clathrate hydrates. *Journal of Chemical Physics* **145**, 211705 (2016). 84, 85, 86, 106, 108

[67] B. Kvamme, A new theory for the kinetics of hydrate formation. in *NGH '96 - 2nd International Conference on Natural Gas Hydrates, Proceedings.*, 139, (1996). 2nd International Conference on Natural Gas Hydrates (NGH 96), Toulouse, France, June 02-06, 1996. 84

[68] R. L. Christiansen and E. D. Sloan JR. Mechanisms and kinetics of hydrate formation. *Annals of the New York Academy of Sciences* **715**, 283 (1994).

[69] E. Sloan and F. Fleyfel. A molecular mechanism for gas hydrate nucleation from ice. *Aiche Journal* **37**, 1281 (1991). 84

[70] J. Lederhos, J. Long, A. Sum, R. Christiansen, and E. Sloan. Effective kinetic inhibitors for natural gas hydrates. *Chemical Engineering Science* **51**, 1221 (1996). 84

[71] G. Guo and P. Rodger. Solubility of aqueous methane under metastable conditions: implications for gas hydrate nucleation. *Journal of Physical Chemistry B* **117**, 6498 (2013). 85

[72] S. Takeya, A. Hori, T. Hondoh, and T. Uchida. Freezing-memory effect of water on nucleation of CO_2 hydrate crystals. *Journal of Physical Chemistry B* **104**, 4164 (2000). 85, 94

[73] W. Kuhs, D. Staykova, and A. Salamatin. Formation of methane hydrate from polydisperse ice powders. *Journal of Physical Chemistry B* **110**, 13283 (2006). 85

[74] A. Falenty, A. Salamatin, and W. Kuhs. Kinetics of CO_2-Hydrate formation from ice powders: Data summary and modeling extended to low temperatures. *Journal of Physical Chemistry C* **117**, 8443 (2013). 85

[75] Y. Dyadin, E. Aladko, and E. Larionov. Decomposition of methane hydrates up to 15 kbar. *Mendeleev Communications*, 34 (1997). 88

[76] T. Kumazaki, Y. Kito, S. Sasaki, T. Kume, and H. Shimizu. Single-crystal growth of the high-pressure phase II of methane hydrate and its raman scattering study. *Chemical Physics Letters* **388**, 18 (2004). 88

[77] S. Schaack, U. Ranieri, P. Depondt, R. Gaal, W. Kuhs, A. Falenty, P. Gillet, F. Finocchi, and L. Bove. Orientational ordering, locking-in, and distortion of CH_4 molecules in methane hydrate III under high pressure. *The Journal of Physical Chemistry C* **122**, 11159 (2018). 92

[78] I. Chou, A. Sharma, R. Burruss, J. Shu, H. Mao, R. Hemley, A. Goncharov, L. Stern, and S. Kirby. Transformations in methane hydrates. *Proceedings of the National Academy of Sciences of the United States of America* **97**, 13484 (2000). 95

[79] A. Sum, R. Burruss, and E. Sloan. Measurement of clathrate hydrates via raman spectroscopy. *The Journal of Physical Chemistry B* **101**, 7371 (1997).

[80] S. Subramanian, R. Kini, S. Dec, and E. Sloan. Evidence of structure II hydrate formation from methane+ethane mixtures. *Chemical Engineering Science* **55**, 1981 (2000). 95, 96

[81] B. Chazallon, C. Focsa, J. Charlou, C. Bourry, and J. Donval. A comparative raman spectroscopic study of natural gas hydrates collected at different geological sites. *Chemical Geology* **244**, 175 (2007). 96

[82] H. Shimizu, T. Kumazaki, T. Kume, and S. Sasaki. In situ observations of high-pressure phase transformations in a synthetic methane hydrate. *J. Phys. Chem. B* **106**, 30 (2002). 96

[83] R. Pratt, D. Mei, T. Guo, and E. Sloan. Structure H clathrate unit cell coordinates and simulation of the structure H crystal interface with water. *Journal of Chemical Physics* **106**, 4187 (1997). 96

[84] J. S. Tse, V. P. Shpakov, V. V. Murashov, and V. R. Belosludov. The low frequency vibrations in clathrate hydrates. *J. Phys. Chem* **107**, 9271 (1997). 101

[85] S. V. Adichtchev, V. R. Belosludov, A. V. Ildyakov, V. K. Malinovsky, A. Y. Manakov, O. S. Subbotin, and N. V. Surovtsev. Low-frequency raman scattering in a Xe hydrate. *The Journal of Physical Chemistry B* **117**, 10686 (2013). 101

[86] L. Shi, Y. Ni, S. Drews, and J. Skinner. Dielectric constant and low-frequency infrared spectra for liquid water and ice Ih within the E3B model. *The Journal of Chemical Physics* **141**, 084508 (2014). 122

[87] J. Bertie and E. Whalley. Infrared spectra of ices Ih and Ic in the range 4000 to 350 cm^{-1}. *The Journal of Chemical Physics* **40**, 1637 (1964). 122

[88] M. Falk and T. Ford. Infrared spectrum and structure of liquid water. *Canadian Journal of Chemistry* **44**, 1699 (1966). 122

[89] C. Lin, J. Smith, S. Sinogeikin, and G. Shen. Experimental evidence of low-density liquid water upon rapid decompression. *Proceedings of the National Academy of Sciences* **115**, 2010 (2018). 123

[90] Y. Takii, K. Koga, and H. Tanaka. A plastic phase of water from computer simulation. *The Journal of chemical physics* **128**, 204501 (2008). 123

[91] J. Aragones and C. Vega. Plastic crystal phases of simple water models. *The Journal of Chemical Physics* **130**, 244504 (2009).

[92] M. Matsumoto, K. Himoto, and H. Tanaka. Spin-one Ising model for ice VII–plastic ice phase transitions. *The Journal of Physical Chemistry B* **118**, 13387 (2014). 123

List of Figures

Acknowledgments

At the end of this trip, my PhD at LENS in the research group of high-pressure physics and chemistry and molecular spectroscopy, I would firstly congratulate myself for having continued to believe in this project, showing dedication and determination, despite the numerous, almost daily, difficulties in which I came across. After this hard trial I feel I have understood more what the art of the researcher involves: infinite dedication and determination. However, this thesis work is not only my goal, but it also belongs to the people who shared the joys and sorrows of this work with me. I would therefore like to thank first of all Professor Roberto Bini, my PhD supervisor, for giving me the opportunity to do this experience. I thank my colleagues and Lab-mates Samuele Fanetti for all the help he gave me during these years, his patience and competence and Margherita Citroni, who for a long time was the true supporter of the project, all the people who contributed to this project: Paolo Bartolini, Laura Bussotti, Andrea Lapini, Andrea Taschin, and Professor Paolo Foggi. I thank Mauro Giuntini, Marco De Pas, Ahmed Hajeb and Riccardo Ballerini for their technical expertise, Demetrio Scelta, Matteo Ceppatelli and Kamil Dziubek for their companionship, and all my friends, doctorate-mates, and all the people I met in these years. A special thanks is to Chiara Calvagna, for her friendship, and for my parents. I dedicate this thesis to Francesco Cappelli because he taught me a lot and he always supported me.

This second version of my thesis is the result of the suggestions I received from my referees. Indeed I want to thank Professor Livia Bove and PhD R. Stewart McWilliams for having accepted to referee my thesis and for having performed this task with competence and accuracy.

Naomi Falsini